Fundamental and Practical Limits to Image Acceleration in Parallel Magnetic Resonance Imaging

by

Michael A. Ohliger

A.B. Physics
Harvard College, 1997

SUBMITTED TO THE HARVARD-MIT DIVISION OF HEALTH SCIENCES AND TECHNOLOGY IN PARTIAL FULFILLMENT OF THE REQUIREMENTS FOR THE DEGREE OF

DOCTOR OF PHILOSOPHY IN MEDICAL PHYSICS
AT THE
MASSACHUSETTS INSTITUTE OF TECHNOLOGY

FEBRUARY 2005 [June 2005]

Signature of Author: _____
Harvard-MIT Division of Health Sciences and Technology
September 9, 2004

Certified by: _____
Daniel K. Sodickson, M.D., Ph.D.
Assistant Professor of Radiology and Medicine
Beth Israel Deaconess Medical Center
Harvard Medical School
Thesis Supervisor

Accepted by: _____
Martha L. Gray, Ph.D.
Edward Hood Taplin Professor of Medical & Electrical Engineering
Co-Director, Harvard-MIT Division of Health Sciences and Technology

Fundamental and Practical Limits to Image Acceleration
in Parallel Magnetic Resonance Imaging

by

Michael A. Ohliger

Submitted to the Harvard-MIT Division of Health Sciences and Technology on September 9, 2004 in Partial Fulfillment of the Requirements for the Degree of Doctor of Philosophy in Medical Physics

Abstract

Imaging speed in conventional magnetic resonance imaging (MRI) is limited by the performance of magnetic field gradients and the rate of power deposition in tissue. Parallel MRI techniques overcome these constraints by exploiting information stored within the spatial sensitivity patterns of radiofrequency detector arrays to substitute for some of the spatial information that would normally be obtained using magnetic field gradients. Parallel MRI strategies have been applied clinically to increase patient comfort, enhance spatial resolution, expand anatomical coverage, and reduce image artifacts.

The effectiveness of parallel MRI techniques is largely determined by the amount of spatial information that is stored in the detector coil sensitivities. This dissertation investigates the spatial encoding properties of coil arrays from three practical and fundamental perspectives. First, a novel array design is presented that enables spatial encoding in multiple directions simultaneously. Second, the impact of inductive coupling between array elements in parallel MRI is investigated theoretically and experimentally. Finally, electromagnetic calculations are described that permit computation of the ultimate intrinsic signal-to-noise ratio available to any physically realizable coil array for parallel MRI. These calculations help to establish fundamental limits to the image accelerations that may be achieved using parallel MRI techniques. These limits are intrinsically related to the wavelengths of the electromagnetic fields at MR imaging frequencies. The sensitivity patterns that correspond to the ultimate intrinsic SNR also represent potential starting points for new coil designs.

Thesis Supervisor: Daniel K. Sodickson, M.D., Ph.D.
Title: Assistant Professor of Radiology and Medicine, Harvard Medical School

Table of Contents

Acknowledgements

The greatest blessing in my life has been my family. Even if all 160 pages of this thesis were only about them, it would be impossible to thank them enough. When I was growing up, my parents taught me the value of education and the importance of following my heart's desire. My big sister, Rachel, has, through her example, set a very high bar for me in terms of both humanity and achievement. She has been an inspiration. My grandparents have been a constant source of love and encouragement, teaching the importance of hard work and a constant smile.

Daniel Sodickson has been everything a person could ask for in a thesis supervisor. He is always ready to listen to any idea with encouragement and enthusiasm. He has always given me the freedom to explore when I wanted it and careful guidance when I needed it. I have been proud to know him the past four years as a mentor and as a friend.

David Cory and David Alsop have made tremendous contributions to my education as members of my thesis committee. They have always been ready with new research suggestions, together with careful admonitions to remember the wider context of my work.

During the course of my research at Beth Israel Deaconess Medical Center, I have been fortunate to be surrounded by a group of people who are simultaneously terrific scientists and wonderful human beings. I have benefited tremendously from the experience, wisdom, and generosity of everyone that I have worked with in the hospital.

Ernest Yeh has shared an office with me for four years and has been the first one to hear every new result and to help solve every new challenge. Charles McKenzie has taught me a great deal about MRI. Charlie has an inspiring enthusiasm for his work, and he is always ready to share new ideas and to help fix almost any problem. Aaron Grant has taught me an incredible amount about physics during the past few years, and has been unfailingly ready with advice and encouragement.

Robert Greenman patiently guided me through building my first coil array, and his teaching has provided the foundation for everything that I know about MR hardware. Patrick Ledden of Nova Medical has also been an invaluable resource, always friendly and always ready to share his irrepressible enthusiasm for building coils.

Huaiyu Yang has, with her constant patience and encouragement, been an irreplaceable part of this thesis. Through all of the ups and downs that come with being a graduate student, Huaiyu has never failed to make the ups more fun, and make the downs seem like tiny bumps.

This research has been supported through the generosity of the Harvard/MIT Division of Health Sciences and Technology; the National Institutes of Health; and Mr. and Mrs. Athanoula Martinos.

Chapter 1.
Introduction to Spatial Encoding Using Radiofrequency Coil Arrays

1.1 Historical Overview and General Introduction

Magnetic resonance imaging (MRI) is a valuable tool for both clinical medicine and basic science. Imaging speed in conventional MRI is limited by the performance of magnetic field gradients and the rate of tissue power deposition. In recent years, a number of parallel MRI techniques have been developed that overcome these constraints by exploiting information stored within the spatial sensitivity patterns of radiofrequency (RF) detector arrays to substitute for some of the spatial information that would normally be obtained using magnetic field gradients.

Detector arrays are commonly used in MRI because they provide images with a high signal-to-noise ratio (SNR) across a large field of view (1). This SNR advantage arises because each detector in an array responds to magnetization from local regions, while ignoring magnetization (and noise) from the rest of the sample. Parallel MRI methods similarly take advantage of the local nature of each coil's reception pattern in order to extract additional spatial information about the sample.

The use of coil arrays to obtain spatial information and thus accelerate image acquisition was first proposed in a variety of techniques that were validated through either numerical simulations or reconstructions of phantom images (2-6). The first use of parallel MRI to obtain *in vivo* images was the Simultaneous Acquisition of Spatial Harmonics (SMASH) technique (7). In this technique, coil sensitivity functions were combined in ways that directly emulated the spatial harmonic modulations imposed by magnetic field gradients. Subsequent modifications helped make the SMASH technique more generally applicable to different image planes and array configurations (8-10). Shortly after the development of SMASH, the Sensitivity Encoding (SENSE) technique (11) was introduced. SENSE presented the problem of parallel imaging in terms of a general inverse of the MR signal equation. In the special case where data were sampled uniformly on a Cartesian grid, SENSE had a particularly simple implementation that can be expressed as the "unfolding" of aliased image-domain data. This image-domain approach was similar to the previously-proposed "subencoding" technique (5).

Following the introduction of SMASH and SENSE, a number of other parallel MRI imaging techniques have been developed (12-20). These various techniques have seen applications in many areas of clinical medicine as well as basic research. The gains in imaging speeds made possible using parallel MRI have been used to reduce the breath-hold time for abdominal scans (21) and to increase the temporal resolution in real-time cardiac imaging (22). Dynamic contrast-enhanced angiography has been a particularly attractive application of parallel MRI (23-25). Single-shot MR sequences often suffer a degradation in resolution and an increase in image distortion when the scan time is too long, and parallel MR has been applied to mitigate both effects (26-28). An RF coil-based technique has been introduced for velocity-encoding of spectroscopic nuclear magnetic resonance data (29). Parallel MRI approaches have even been applied as methods of detecting and correcting for motion (30,31) as well as chemical shift (32) artifacts. Some form of parallel MRI methodology is now available as a standard clinical product from every major MRI device manufacturer.

When parallel MRI techniques were first introduced, the majority of clinical MRI scanners were able to acquire data simultaneously from either four or six detector coils. The restrictions on the number of independent detectors that could be incorporated into an array not only limited the

maximum theoretical image acceleration to either four- or six-, but these restrictions also led to a degradation of image quality for more modestly accelerated images. Early investigations used a multiplexed array design to incorporate an eight-channel coil array into a single-channel MR system (33). Recently, largely as a result of developments in parallel MRI, MR systems with eight independent receiver channels have become routinely available, and specialized coil designs have been described for these systems (34). Prototype MR scanners have been introduced with 16 (35), 32 (36), and 64 (37) receiver channels. These new systems offer substantial flexibility for designing coil arrays optimized for parallel MRI.

While the assembly of simple loop coils into arrays has been effective for parallel MRI, several investigators have introduced arrays composed of non-standard elements. These alternative arrays have included a planar microstrip antenna (38,39); the butterfly and loop elements of a quadrature surface coil (40); a TEM resonator (41); and specialized volume coils (4,42-46).

The freedom provided by the increasing number of available receiver channels, combined with the rapidly-expanding repertoire of array designs, has led to several fundamental and practical questions regarding the use of coil arrays for spatial encoding in parallel MRI. This dissertation addresses three of these important issues. First, because the number of available array channels will frequently be limited, there is pressure to develop flexible array designs with a limited number of coil elements that can provide spatial encoding in several directions at once. Second, as the density of coil array elements continues to increase and as it becomes more difficult to isolate the elements from each other electrically, there is a question as to whether coupling interactions between coil elements will limit the effectiveness of parallel MRI techniques. Finally, as the performance of coil arrays for parallel MRI continues to improve, it is useful to understand the fundamental limits on coil encoding. To what extent, one might ask, is coil array design for parallel MRI constrained by the fundamental physical interactions between the coil array and the sample, rather than being limited only by the imagination of coil array designers?

The remainder of this chapter describes the general principles underlying the use of radiofrequency (RF) coil arrays for spatial encoding in MRI. Sections 1.2 and 1.3 briefly review the origins of the MR signal as well as the techniques of gradient encoding that are used in

conventional MRI. The speed limitations of conventional gradient encoding lead naturally to a brief introduction to the concepts of parallel imaging.

Once the basic concepts of parallel MRI have been discussed, the use of coil arrays for spatial encoding is described first qualitatively and then quantitatively. Expressions are derived for the sensitivity and noise characteristics of a detector array in terms of the electromagnetic interactions between the array and the sample. Selected coil design concepts are introduced, followed by a short discussion of complications that are encountered when assessing coil arrays experimentally.

In Chapter 2, a novel array design with concentric elements is presented that provides for simultaneous spatial encoding in several directions. In Chapter 3, the impact of inductive coupling between array elements on the effectiveness of parallel MRI is assessed theoretically and experimentally. Chapter 4 is devoted to calculating the "ultimate intrinsic SNR" for a coil array that is used for parallel imaging. The ultimate SNR sets an upper bound on the performance of any physically realizable coil array. The final chapter of this thesis attempts to summarize and explore the implications of this work for the design of future coil arrays for high performance applications of parallel MRI.

1.2 The MRI Signal

Many textbooks have been written that are devoted to the phenomenon of nuclear magnetic resonance as well as the basic principles of forming an MR image. The discussions of signal detection and gradient encoding presented in this section and in Section 1.3 are not intended to be comprehensive. Rather, these sections are intended to briefly review the general concepts and basic formalism that will be important for the discussions of receiver-coil encoding presented in the rest of this dissertation. The basic development of these sections, with some minor changes in notation, closely follows that provided in the introductory chapters of reference (47).

The MRI experiment involves the manipulation and detection of magnetization within a sample, which often consists of biological tissue. While it is possible to introduce magnetization into the

sample from an outside source, most MRI techniques utilize endogenous magnetization, which is created by placing the sample inside a strong uniform magnetic field. Atomic nuclei with non-zero magnetic moments align themselves with the applied field, creating a net macroscopic magnetization. The most commonly imaged nucleus, because of its abundance in biological tissues and its high inherent signal level, is that of hydrogen, whose nucleus consists of a single proton. A sample of protons that is placed in a magnetic field that has magnitude $\mathbf{B}_0$ will acquire a magnetization density at thermal equilibrium equal to (47)

$$\mathbf{M}^0(\mathbf{r}) = \frac{B_0 \gamma^2 \hbar^2}{4kT} \rho(\mathbf{r}) \hat{\mathbf{z}}, \qquad [1.1]$$

where the z-axis has been placed parallel to $\mathbf{B}_0$, $\rho(\mathbf{r})$ is the number of protons per unit volume, T is the absolute temperature, k is Boltzmann's constant, and γ is the proton's gyromagnetic ratio. The gyromagnetic ratio is specific to a given chemical species, and it describes the ratio of a spin's magnetic moment to its angular momentum.

Radiofrequency energy is used to excite the protons (generically called "spins") such that a portion of the net magnetization is rotated from the z-axis into the x-y plane. The magnetization that reaches the x-y plane precesses with angular frequency ω about the main magnetic field $\mathbf{B}_0$. The x- and y- components of the magnetization in the laboratory frame, $M_x(\mathbf{r},t)$ and $M_y(\mathbf{r},t)$, can be written in terms of the magnetization in the rotating reference frame, $\tilde{M}_x(\mathbf{r},t)$ and $\tilde{M}_y(\mathbf{r},t)$,

$$\begin{aligned} M_x(\mathbf{r},t) &= \tilde{M}_x(\mathbf{r},t)\cos(\omega t) + \tilde{M}_y(\mathbf{r},t)\sin(\omega t) \\ M_y(\mathbf{r},t) &= -\tilde{M}_x(\mathbf{r},t)\sin(\omega t) + \tilde{M}_y(\mathbf{r},t)\cos(\omega t) \end{aligned}, \qquad [1.2]$$

The angular frequency of precession, ω, is known as the Larmor frequency, and it is a function of the applied field and the spin's gyromagnetic ratio:

$$\omega = \gamma B_0. \qquad [1.3]$$

The time-dependence of the rotating-frame magnetization in Eq. [1.2] reflects the relaxation of spins due to energy exchange with the environment as well as loss of coherence due to the presence of non-uniform magnetic fields. These processes typically occur at rates that are much slower than the overall precession frequencies of the spins (47). The total transverse magnetization can be written in complex notation as

$$\begin{aligned}\mathbf{M}(\mathbf{r},t) &= M_x(\mathbf{r},t)\hat{\mathbf{x}} + M_y(\mathbf{r},t)\hat{\mathbf{y}} \\ &= \mathrm{Re}\left[\left(\hat{\mathbf{x}} - i\hat{\mathbf{y}}\right)\left(\tilde{M}_x(\mathbf{r},t) + i\tilde{M}_y(\mathbf{r},t)\right)e^{-i\omega t}\right], \\ &= \mathrm{Re}\left[\left(\hat{\mathbf{x}} - i\hat{\mathbf{y}}\right)\tilde{M}(\mathbf{r},t)e^{-i\omega t}\right]\end{aligned} \qquad [1.4]$$

where $\tilde{M}(\mathbf{r},t) \equiv \tilde{M}_x(\mathbf{r},t) + i\tilde{M}_y(\mathbf{r},t)$, is the complex-valued rotating frame magnetization. Precessing magnetization gives rise to a time-varying magnetic field on the outside of the sample, and this time-varying field is detected as alternating magnetic flux through the surface of a detector coil. The voltage induced in the detector coil is amplified and then demodulated by the functions $\cos(\omega t)$ and $\sin(\omega t)$. The signals from the two demodulated channels are combined and stored as a single complex number:

$$S(t) = \int_{sample} C(\mathbf{r})\tilde{M}(\mathbf{r},t)d^3\mathbf{r} + n(t). \qquad [1.5]$$

In this expression, $C(\mathbf{r})$ is a complex-valued spatial sensitivity function, whose spatial dependence reflects the fact that the detector interacts more strongly with spins that are in one part of the sample (usually near the detector) than with spins in other parts of the sample (usually far from the detector). $n(t)$ is a complex variable representing noise voltages that are recorded from the real and imaginary channels.

The functional form of the sensitivity, $C(\mathbf{r})$, depends on the details of the detector's design; A method for calculating this function will be discussed later in this chapter. The physical origins of the noise, $n(t)$, will also be discussed. For the moment, we simply state that the real and

imaginary parts of $n(t)$ are both random functions of time, with zero mean and equal standard deviation σ.

1.3 Spatial Encoding Using Magnetic Field Gradients

Because the precession frequencies and relaxation rates of spins inside a sample depend on the details of each proton's molecular environment, Equation [1.5] contains a great deal of spectroscopic information about the sample. The equation offers little information, however, about where the spins are located. In conventional (non-parallel) MRI techniques, spatial information is usually obtained by adding to the main magnetic field, $\mathbf{B}_0$, a second z-directed magnetic field, $\mathbf{B}_{gradient}$, that varies linearly with position. If the magnitude of the field gradient, $\mathbf{G}$, is defined as

$$\mathbf{G} = \nabla(\mathbf{B}_{gradient} \cdot \hat{\mathbf{z}}), \qquad [1.6]$$

and the protons are allowed to evolve for a time Δt, then the overall magnetization density acquires a spatially-varying phase such that

$$M'(\mathbf{r},t) = M(\mathbf{r},t)\exp(i\Delta t\gamma \mathbf{G}\cdot\mathbf{r}). \qquad [1.7]$$

The gradient-induced phase in Equation [1.7] can also be written in terms of a wave vector $\mathbf{k} \equiv \Delta t\gamma\mathbf{G}$, and Equation [1.5] becomes

$$S(\mathbf{k}) = \int_{sample} C(\mathbf{r})M'(\mathbf{r},\mathbf{k})\exp(i\mathbf{k}\cdot\mathbf{r})d^3\mathbf{r} + n(\mathbf{k}). \qquad [1.8]$$

The MR signal acquired under the influence of a linear gradient corresponds to a single Fourier component of the underlying magnetization density that has spatial frequency $\mathbf{k}$. Because many relaxation effects cause magnetization to decay in times that are comparable to the length of time, Δt, that the gradients are applied, the magnetization amplitude is, in general, a function of the k-space point. However, as an initial approximation, the effects of relaxation can be included in the signal equation as an overall constant. Thus, Eq. [1.8] can be written as

$$S(\mathbf{k}) = \int_{sample} C(\mathbf{r}) M(\mathbf{r}) \exp(i\mathbf{k}\cdot\mathbf{r}) d^3\mathbf{r} + n(\mathbf{k}), \qquad [1.9]$$

where the quantity $M(\mathbf{r})$ is now assumed to include the effects of relaxation.

The form of Eq. [1.9] implies that, abstractly, each gradient-encoded sample corresponds to a point in a discretely-sample "k-space." Often, the sampling of k-space is uniform and rectilinear such that

$$\mathbf{k} = \left[a\Delta k_x, b\Delta k_y, c\Delta k_z \right] (a,b,c \text{ integers}). \qquad [1.10]$$

While many MR imaging strategies employ non-Cartesian samplings of k-space, the Cartesian sampling scheme provides a simple framework for specifying the sampling requirements – and therefore the time requirements – for image acquisition. The number of points in *k*-space that must be obtained in order to acquire an entire image depends on the size of the object being imaged and the desired spatial resolution. In order to achieve a spatial resolution in the *x*-direction equal to Δx, the maximum acquired value of k-space in that direction must be $k_x^{\max} = 1/\Delta x$. The sampling interval, Δk_x, must also be small enough so that $1/\Delta k_x$ (also known as the "field of view") is larger than the object in that dimension. If the sampling interval is too large, the reconstructed image will suffer from aliasing, and different parts of the image will be folded on top of each other.

For simple Cartesian sampling schemes, magnetic field gradients can be applied along the three principal spatial axes (as in the example above), or else linear combinations of gradients may be used to acquire images in any specified image plane. Regardless of the image plane that is chosen, the same general acquisition strategy can be used. K-space points along a single axis – called the *frequency encode* axis – are acquired under the influence of field gradients that are applied while the signal is being received. The two axes perpendicular to the frequency-encode axis are called the *phase encode* axes. The k-space coordinates in these phase-encode directions are changed by applying gradients prior to the frequency-encode readout. One entire frequency-

encode readout is necessary for each increment in the phase-encode direction. "3D" acquisition strategies have two phase-encode directions, while "2D" sequences only have one.

1.4 Limitations of Magnetic Field Gradients

Magnetic field gradients provide a flexible method for encoding MR magnetization spatially. The image plane and slice thickness may be tailored for any application, and the technique is compatible with virtually any contrast mechanism. Fourier encoding also provides inherent noise averaging when the image is reconstructed. On the other hand, gradient-based techniques can be quite slow. For each point in the phase-encode direction, the frequency encode readout must be repeated, and often the entire spin preparation needs to be repeated as well. There are both practical and physiological limits to how fast this sequential data acquisition can proceed. From a practical standpoint, gradient switching speeds and data digitization rates are both limited by technological constraints. On a more fundamental level, rapidly-varying magnetic fields that are created by changing gradients have the potential to induce currents in the body and cause peripheral nerve stimulation. In addition, the frequent spin excitations that occur during fast MR imaging sequences can lead to unwanted tissue heating. The problem of tissue heating is likely to be especially prominent as human MR scanners are developed at progressively higher magnetic fields.

1.5 Spatial Encoding Using Detector Coil Sensitivities: Parallel MRI

The practical and physiological limits on imaging speed using magnetic field gradients have inspired the development of new methods for spatial encoding. One class of new spatial encoding methods, which has become known as parallel MRI, uses spatial information extracted from radiofrequency detector coil sensitivities as a substitute for some of the information normally obtained using magnetic field gradients.

Consider a discrete form of the MR signal equation from a single detector (Eq. [1.8])

$$S(\mathbf{k}_m) = \sum_{pixel\ j} C(\mathbf{r}_j) M(\mathbf{r}_j) e^{i\mathbf{k}_m \cdot \mathbf{r}_j} + n(\mathbf{k}_m) . \qquad [1.11]$$

In addition, assume that the spatial sensitivity function, $C(\mathbf{r}_j)$, has been measured. If there are N pixels to be reconstructed and N acquired k-space points, then Equation [1.11] describes a linear system with an equal number of equations and unknowns. If the number of acquired k-space points is reduced by a factor R, then there will be only N/R equations available to reconstruct N unknown magnetization values, and the linear system will be underdetermined. However, if data are acquired simultaneously using L coils, there will be an independent set of acquired signal data S_l for each coil. The new linear system,

$$S_l(\mathbf{k}_m) = \sum_{pixel\ j} C_l(\mathbf{r}_j) M(\mathbf{r}_j) e^{i\mathbf{k}_m \cdot \mathbf{r}_j} + n_l(\mathbf{k}_m), \qquad [1.12]$$

has $L*N/R$ equations, and the N unknowns can be determined as long as the number of coils is greater than the reduction in sampling density.

Equation [1.12] is a very general formulation of the process of parallel imaging, and it is the basis for the Sensitivity Encoding (SENSE) technique (11). The coil sensitivities and the gradient-induced sinusoidal variations are formally placed in a single encoding matrix $\mathbf{B}$

$$\mathbf{B}_{(lm),j} = C_l(\mathbf{r}_j) e^{i\mathbf{k}_m \cdot \mathbf{r}_j}. \qquad [1.13]$$

If the acquired signal and noise, together with the magnetization density, are written as column vectors, then the signal equation becomes

$$\mathbf{S} = \mathbf{BM} + \mathbf{n}. \qquad [1.14]$$

Within this formalism, reconstructing an image amounts to finding a matrix $\mathbf{B}^{inv}$ such that $\mathbf{B}^{inv}\mathbf{B}$ is equal to the identity matrix. In practical implementations of parallel imaging, the number of coils, L, is typically larger than the reduction in k-space sampling, R. As a result, $\mathbf{B}$ is a rectangular matrix, and there are many possible choices for $\mathbf{B}^{inv}$. It has been shown in References (11) and (16) that the minimum-norm solution of Equation [1.14], which leads to an image reconstruction with the least possible noise, is given by

$$\mathbf{B}_{\text{min norm}}^{inverse} = \left(\mathbf{B}^{\dagger}\boldsymbol{\Psi}^{-1}\mathbf{B}\right)^{-1}\mathbf{B}^{\dagger}\boldsymbol{\Psi}^{-1}. \qquad [1.15]$$

Here, $\boldsymbol{\Psi}$ is a matrix that describes the noise statistics of the various coils. The diagonal elements of $\boldsymbol{\Psi}$ are equal to the total noise power received by a given coil, and the off-diagonal elements of $\boldsymbol{\Psi}$ represent correlations in noise between multiple coils (noise correlations will be discussed at greater length later).

The SENSE formulation of the parallel MRI reconstruction (Eq. [1.14]), which prescribes an inverse of the MR signal equation, is straightforward and general. Many more specialized parallel MRI techniques can be formally classified as modifications of this approach. These specialized techniques tend to either make the inverse in Equation [1.15] easier to perform or to make the inverse more numerically stable, especially for high acceleration factors.

1.5.a Sensitivity Calibration

The definition of the encoding matrix in Equation [1.13] explicitly assumes that the coil sensitivities have been measured. Some sort of sensitivity calibration is a universal requirement for parallel imaging approaches. The robust acquisition of sensitivity information is a research field in its own right, and extensive discussion is provided elsewhere. A select number of representative approaches are reviewed here.

Coil sensitivities can be calculated using the electromagnetic techniques that will be described in Section 1.8. This approach can be logistically difficult because it requires the coil array to be attached to a rigid frame in order ensure that its elements are in the same locations at the time of each scan. Even for coils that are fixed rigidly, samples with different sizes and electrical properties will have different field patterns inside of them. Because of these complications, the coil array sensitivity patterns are usually measured separately for each patient.

Coil information is often acquired as part of a given imaging protocol by performing a dedicated fully-encoded scan. This reference scan need not have the same resolution or contrast as the target image acquisition. The "pure" sensitivity functions can be determined by dividing the coil-modulated images by a separate image acquired using a uniform-sensitivity body coil (11).

Additionally, several post-processing methods have been described for further improving the quality of the sensitivity reference (48,49).

An alternative approach to coil calibration makes use of so-called "*in vivo*" coil sensitivity data, in which a fully-sampled data set from a separate full- or reduced-resolution scan can be used directly, eliminating the need for body coil data (5,8,16,50). This approach is possible because only the *relative* coil sensitivities are required to reconstruct undersampled data. Images reconstructed using *in-vivo* coil sensitivity data do retain some degree of coil sensitivity modulation. In one common approach, the final image has an overall profile similar to a "sum-of-squares" reconstruction of the fully-encoded image data. Unlike a sum-of-squares reconstruction, however, parallel reconstructions that use *in vivo* coil sensitivities are able to preserve information about the relative phases between different acquisitions. This distinction is important for the experimental analysis of coil SNR. One tremendous advantage of *in vivo* coil sensitivities is that they allow coil sensitivity data to be embedded into the undersampled acquisition, eliminating the need for a separate reference and mitigating potential errors that might result from the misregistration of coil sensitivity data (15,17,51-53).

1.6 Qualitative Descriptions of Spatial Encoding Using Coil Arrays

The encoding matrix inversion in Equations [1.13]-[1.15] provides a general prescription for reconstructing undersampled MR data using coil array sensitivities. The most important principle of coil array design for parallel MRI is the recognition that while gradient-induced spatial harmonic functions are orthogonal to each other over a chosen field-of-view, the sensitivity-modulated harmonics ($C_l(\mathbf{r})e^{i\mathbf{k}_m\cdot\mathbf{r}}$, also called "encoding functions") generally are not orthogonal. It will be shown later that this lack orthogonality can amplify noise in the final reconstructed image. The analysis of noise amplifications will eventually provide a quantitative measure of how appropriate a chosen array design is for parallel MRI.

While quantitative measures of array performance are useful for evaluating a specific array designs once they have been chosen, it is also useful to have a more intuitive picture of the design choices that lead to good arrays for parallel MRI. An intuitive picture can be formed by

examining the process of coil array spatial encoding from several qualitative perspectives. Each individual perspective that will be discussed is, at some level, equivalent. However, each perspective still provides its own particular insights into coil design.

1.6.a Emulation of Spatial Harmonics

Coil arrays can provide spatial information about a sample by emulating the spatial modulations provided by the magnetic field gradients that have been omitted. This idea is the basis of the SMASH technique (7). Specifically, if a set of coefficients are found such that

$$\sum_{l=1}^{N} w_l C_l(\mathbf{r}) = e^{i\Delta\mathbf{k}\cdot\mathbf{r}}, \qquad [1.16]$$

the same linear combination can be applied to the acquired MR data

$$\begin{aligned}\sum_{l=1}^{N} w_l S_l(\mathbf{k}) &= \int_{sample} \left(\sum_{l=1}^{N} w_l C_l(\mathbf{r}) \right) M(\mathbf{r}) \exp(i\mathbf{k}\cdot\mathbf{r}) d^3\mathbf{r} \\ &= \int_{sample} M(\mathbf{r}) \exp(i\Delta\mathbf{k}\cdot\mathbf{r}) \exp(i\mathbf{k}\cdot\mathbf{r}) d^3\mathbf{r} \\ &= \int_{sample} M(\mathbf{r}) \exp(i(\mathbf{k}+\Delta\mathbf{k})\cdot\mathbf{r}) d^3\mathbf{r} \\ &= S(\mathbf{k}+\Delta\mathbf{k})\end{aligned} \qquad [1.17]$$

The effect of applying the coefficients w_l is to "move" the acquired data in k-space by a distance $\Delta\mathbf{k}$.

The accuracy of the reconstructed line $S(\mathbf{k}+\Delta\mathbf{k})$ depends on the accuracy of the linear fit in Equation [1.16]. One approach to designing coil arrays is to choose detectors that have linear combinations that approximate spatial harmonics as well as possible. In place of linear combinations of coil sensitivities, a single coil with a harmonic sensitivity profile could also be used. In fact, such detectors have been proposed (42-44).

1.6.b Unfolding of Aliased Data

When data are acquired on a Cartesian k-space grid and then undersampled by a factor, R, the reconstructed image is aliased, with signal intensity from different parts of the sample "folding" on top of each another. Each reconstructed pixel represents the sum of R equally-spaced voxels across the field-of-view. If the sensitivity for coil l is large at a point x_0 and small at the aliased points $x_0 \pm \Delta x$, then the signal from coil l will principally represent the magnetization at x_0 and not at the aliased points:

$$S_l(x_0) \approx C_l(x_0)M(x_0). \qquad [1.18]$$

The Partially Parallel Imaging with Localized Sensitivities (PILS) reconstruction technique (14) is based on the assumption of completely localized coil sensitivities. The subencoding reconstruction technique (5) as well as the image-domain formulation of SENSE (11) operate using a similar principle, but allow the coil sensitivities to not be completely localized.

Viewing the parallel MRI reconstruction as the unfolding of aliased pixels suggests that coil arrays with elements whose sensitivity profiles are targeted to a specific region of the field-of-view should be very effective at reconstructing undersampled data. In addition, it is also possible to distinguish different regions of a sample by employing coils that have different phase variations between the different aliased regions of the sample. Differences in phase have been exploited in order to use a quadrature pair of coil elements for parallel MRI (40) as well as the coils with harmonic sensitivity profiles that were discussed in the last section (42-44).

1.6.c Broadening of the Acquired k-Space Data

The Fourier transform of the product $C(\mathbf{r})M(\mathbf{r})$ in Equation [1.9] can be written as the convolution of the two functions' Fourier transforms, $\tilde{C}(\mathbf{k})$ and $\tilde{M}(\mathbf{k})$:

$$S_l(\mathbf{k}) = \int \tilde{C}_l(\mathbf{k}')\tilde{M}(\mathbf{k}-\mathbf{k}')d^3\mathbf{k}'. \qquad [1.19]$$

The acquired signal from a single receiver coil contains information about the targeted point in k-space, $\mathbf{k}$, together with several of the surrounding k-space points. The amount of spatial

frequency information that is acquired at one time by any coil is determined by the width of that coil's sensitivity profile in k-space. Therefore, the widths of component coils' spatial frequency spectra set an upper bound on the allowable distance between the acquired k-space points and the missing k-space points that need to be reconstructed (54). Several parallel imaging techniques (16,18,19) exploit the limited spatial frequency content of the coil sensitivities in order simplify the reconstruction of undersampled data.

1.6.d Generalized Spatial Projections

The formal grouping of the coil sensitivity together with the sinusoidal modulations induced by the gradients into an encoding matrix (Eq. [1.13]) suggests that each acquired piece of data is a "generalized projection" through the sample (16). Coil array sensitivities can be tailored for parallel imaging such that they lead to overall projection functions that are as spatially orthogonal as possible. Incidentally, while much focus is placed on designing coil sensitivities to complement the gradient-encoded Fourier harmonics, it might also be possible to implement non-Fourier gradient encoding schemes that complement the coil sensitivities.

1.7 Quantitative Analysis of Array Performance

The spatial encoding capabilities of coil arrays may be analyzed quantitatively by measuring the signal-to-noise ratio of the reconstructed undersampled data. When an image acquisition is accelerated using parallel MRI techniques, the reduction in scan time comes at a cost in terms of the SNR of the final image. As mentioned earlier, the Fourier transform-based reconstruction of fully-sampled data has the effect of averaging the noise associated with each acquired k-space line. Thus, if the noise of each k-space point obtained from coil l has variance σ_l^2, each pixel reconstructed from that coil will have noise (per unit signal) with variance equal to

$$\left[\sigma_l^2\right]_{\text{image pixel}} = \frac{1}{N}\sigma_l^2, \qquad [1.20]$$

where N is the total number of acquired k-space points. This implies that R-fold undersampled data that are reconstructed with parallel image will have a reduction in SNR/pixel of at least $\sqrt{R}$.

The second source of SNR loss in parallel MRI, which has been discussed qualitatively in the previous section, occurs when noise is amplified by the non-orthogonal transformations required by the parallel MR reconstruction. In order to understand these noise amplifications quantitatively, we note that the noise power of an *R*-fold accelerated SENSE reconstruction can be calculated from the encoding matrix, Eq. [1.13] (11),

$$\left(\sigma_j^{SENSE}\right)^2 \propto \left[\left(\mathbf{B}_R^{\dagger}\boldsymbol{\Psi}^{-1}\mathbf{B}_R\right)^{-1}\right]_{j,j}, \qquad [1.21]$$

where $\mathbf{B}_R$ is the encoding matrix corresponding to an *R*-fold accelerated acquisition. Using the same array in the absence of parallel imaging, the encoding matrix is $\mathbf{B}_{\text{full}}$ and the noise power is given by

$$\left(\sigma_j^{FULL}\right)^2 \propto \left[\left(\mathbf{B}_{\text{full}}^{\dagger}\boldsymbol{\Psi}^{-1}\mathbf{B}_{\text{full}}\right)^{-1}\right]_{j,j}. \qquad [1.22]$$

For an image with uniform Cartesian sampling, the square matrix $\mathbf{B}_{\text{full}}^{\dagger}\boldsymbol{\Psi}^{-1}\mathbf{B}_{\text{full}}$ is diagonal, and hence,

$$\left[\left(\mathbf{B}_{\text{full}}^{\dagger}\boldsymbol{\Psi}^{-1}\mathbf{B}_{\text{full}}\right)^{-1}\right]_{j,j} = \left(\left[\mathbf{B}_{\text{full}}^{\dagger}\boldsymbol{\Psi}^{-1}\mathbf{B}_{\text{full}}\right]_{j,j}\right)^{-1}. \qquad [1.23]$$

Moreover, it is shown in Appendix A that, for Fourier sampling patterns, the diagonal elements of the matrix $\mathbf{B}_R^{\dagger}\boldsymbol{\Psi}^{-1}\mathbf{B}_R$ are related to the elements of the matrix $\mathbf{B}_{\text{full}}^{\dagger}\boldsymbol{\Psi}^{-1}\mathbf{B}_{\text{full}}$ through the simple relation:

$$\left[\mathbf{B}_R^{\dagger}\boldsymbol{\Psi}^{-1}\mathbf{B}_R\right]_{j,j} = \frac{1}{R}\left[\mathbf{B}_{\text{full}}^{\dagger}\boldsymbol{\Psi}^{-1}\mathbf{B}_{\text{full}}\right]_{j,j}. \qquad [1.24]$$

This leads to a compact expression for the SNR penalty for parallel imaging (11)

$$SNR^{SENSE} = \frac{SNR^{FULL}}{\sqrt{R\left[\left(\mathbf{B}_R^{\dagger}\boldsymbol{\Psi}^{-1}\mathbf{B}_R\right)\right]_{j,j}\left[\left(\mathbf{B}_R^{\dagger}\boldsymbol{\Psi}^{-1}\mathbf{B}_R\right)^{-1}\right]_{j,j}}}. \qquad [1.25]$$

This expression for the SNR changes caused by the parallel MRI reconstruction explicitly assumes a uniform Cartesian k-space sampling pattern. However, the more general expressions in Equations [1.21] and [1.22] can still be used for other sampling patterns. The factor of $\sqrt{R}$ in the denominator of Equation [1.25] is simply the SNR loss due to reduced noise averaging described above. The second term describes a spatially-dependent amplification of noise, which has become known as the "g-factor:"

$$g_j \equiv \sqrt{\left[\left(\mathbf{B}_R^{\dagger}\boldsymbol{\Psi}^{-1}\mathbf{B}_R\right)\right]_{j,j}\left[\left(\mathbf{B}_R^{\dagger}\boldsymbol{\Psi}^{-1}\mathbf{B}_R\right)^{-1}\right]_{j,j}}. \qquad [1.26]$$

The g-factor is (by definition) always greater than one, and it depends on the geometry of the coil sensitivity functions. Because of this geometry dependence, the g-factor has become an attractive figure of merit for assessing the performance of coil arrays for parallel MRI. While the g-factor is a generally useful measure, it is important to recognize that any changes in coil geometry will also change the coil's baseline SNR (Eq. [1.22]). Improvements in g-factor are not valuable when they come at the cost of degradations in the overall array performance. It is also important to recognize that the g-factor is a function of *both* the coil sensitivities and the pattern of acquired k-space lines. Therefore, the g-factor will, in general, be different for different undersampling factors, object sizes, and image planes. Finally, while the overall SNR performance of the array has been divided out of the expression for the g-factor, there is still a second-order dependence of g on the noise covariance matrix $\boldsymbol{\Psi}$. Drastic changes in an array's noise power can affect the array's g-factor.

Equations [1.22] and [1.25] provide a set of analytical tools for evaluating the performance of any coil array for parallel MRI. In order to make use of these expressions, it is necessary to know 1) the coil sensitivities, $C_l(\mathbf{r})$, 2) the pattern of the k-space acquisition, and 3) the noise covariance matrix $\boldsymbol{\Psi}$. The k-space acquisition pattern is determined by the desired image plane geometry and pulse sequence. The coil sensitivities and noise covariance matrix can, of course,

be measured empirically at the time of imaging. However, for understanding and designing coil arrays, it is useful to have methods for predicting $C_l(\mathbf{r})$ and Ψ computationally. The goal of the next section is to derive expressions for $C_l(\mathbf{r})$ and Ψ in terms of the coil array geometry as well as the basic electromagnetic interactions between the coil and the sample.

1.8 Electrodynamic Determination of Coil Sensitivity and Noise Characteristics

In the formal equations for parallel imaging, the coil sensitivity $C_l(\mathbf{r})$ represents a descriptive image processing concept, which quantifies the local spatial modulations induced by a surface coil. Similarly, the noise vector $\mathbf{n}$ in Equation [1.14] is based on a phenomenological description of noise and its correlations. In order to speak meaningfully about designing coil arrays with tailored sensitivity patterns, it is important to relate the descriptive parameters $C_l(\mathbf{r})$ and $\mathbf{n}$ to the more fundamental electrical characteristics of a coil array.

1.8.a Coil Sensitivity

NMR detectors are typically composed of resonant structures that consist of one or more current loops. Precessing magnetization creates a time-varying magnetic flux through each loop, leading to an induced voltage

$$V = -\frac{\partial}{\partial t}\int \mathbf{B}^{\text{magnetization}} \cdot \hat{\mathbf{n}} da\,, \qquad [1.27]$$

where $\hat{\mathbf{n}}$ is a unit vector normal to the surface bounded by the conductor. The integral in Equation [1.27] is generally quite cumbersome to perform directly. The integration can be simplified by resorting to the principle of reciprocity (55), which states that the flux induced through a coil by precessing magnetization can be written in terms of $\hat{\mathbf{B}}^{\text{coil}}$, which is the magnetic field that would be generated by a unit current flowing around the coil

$$\int \mathbf{B}^{\text{magnetization}} \cdot \hat{\mathbf{n}} da = \int \hat{\mathbf{B}}^{\text{coil}} \cdot \mathbf{M} d^3\mathbf{r}\,. \qquad [1.28]$$

If the transverse magnetization is written as the real part of a complex number, and the time dependence is assumed to be $\mathbf{M} = \mathbf{M}_0 e^{-i\omega t}$, then the voltage induced in the receiver coil is

$$V = i\omega \int \hat{\mathbf{B}}^{\text{coil}} \cdot \mathbf{M} e^{-i\omega t} d^3\mathbf{r} . \qquad [1.29]$$

Thus, the receiver coil imposes a spatial modulation on the sample magnetization.

Comparing Equation [1.5] for the MR signal with Equation [1.29] suggests the following relationship between the coil sensitivity, $C(\mathbf{r})$, and $\hat{\mathbf{B}}^{\text{coil}}$:

$$C(\mathbf{r}) = \hat{\mathbf{B}}_x^{\text{coil}}(\mathbf{r}) - i\hat{\mathbf{B}}_y^{\text{coil}}(\mathbf{r}) . \qquad [1.30]$$

1.8.b Coil Noise

Noise in an MRI experiment can be divided broadly into noise that arises from the sample itself and noise that arises from the receiver circuitry and the surrounding environment. Noise that is generated by sources outside of the sample can generally be reduced by taking steps such as shielding the MR system, choosing appropriate coil materials, and lowering the temperature of the coil. Thermal noise that comes from the sample itself, however, is to a large extent unavoidable. Because the sample is in equilibrium with the coil, thermal fluctuations induce a voltage, $V_n(t)$, in the coil that is randomly distributed in time, with zero mean and variance equal to (56):

$$\left\langle V_n^2 \right\rangle_{time} = 4kTR\Delta f . \qquad [1.31]$$

In this equation, Δf is the bandwidth of the acquisition and R is the series resistance that the sample presents to the coil. The sample resistance is calculated by computing the ohmic losses due to a current I flowing around the coil (57)

$$R = \frac{1}{|I|^2} \int \sigma(\mathbf{r}) |\mathbf{E}(\mathbf{r})|^2 d^3\mathbf{r} . \qquad [1.32]$$

Here, $\sigma(\mathbf{r})$ is the sample conductivity and $\mathbf{E}(\mathbf{r})$ is the electric field generated by a current I flowing in the coil.

1.8.c SNR for a Single Coil

Equations [1.29]-[1.32] are the principal theoretical tools for predicting the performance of surface coils. The maximum possible magnetization density for polarized spins in a magnetic field with strength B_0 is given by Eq. [1.1]. The maximum signal received from a small unit of magnetization at spatial position, $\mathbf{r}_0$, with volume, ΔV, and uniform spin density, ρ, is

$$\begin{aligned} V_{\max} &= \omega C(\mathbf{r}_0) M_{\max}(\mathbf{r}_0) \\ &= \omega \frac{B_0 \gamma^2 \hbar^2}{4kT} \rho(\mathbf{r}_0)(\Delta V) C(\mathbf{r}_0) \\ &= \omega \frac{B_0 \gamma^2 \hbar^2}{4kT} \rho(\mathbf{r}_0)(\Delta V)\left[\hat{B}_x^{\text{coil}}(\mathbf{r}_0) - i\hat{B}_y^{\text{coil}}(\mathbf{r}_0)\right] \end{aligned} \quad . \qquad [1.33]$$

The performance of a coil is typically quantified in terms of the signal-to-noise ratio (SNR), which is the signal divided by the standard deviation of the noise:

$$SNR_{\max} = \omega \frac{B_0 \gamma^2 \hbar^2}{\sqrt{\Delta f}\,(4kT)^{3/2}} \rho(\mathbf{r}_0)(\Delta V) \frac{\left|B_x^{\text{coil}}(\mathbf{r}_0) - iB_y^{\text{coil}}(\mathbf{r}_0)\right|}{\left(\int \sigma |\mathbf{E}(\mathbf{r})|^2 \, d^3\mathbf{r}\right)^{1/2}} . \qquad [1.34]$$

It is notable that, with the exception of the receiver bandwidth, Δf, there are no adjustable parameters in Equation [1.34]. The value of every quantity is completely determined by the spatial arrangement and physical composition of the receiver coil and the sample. Furthermore, any changes in coil design are likely to affect both the numerator and the denominator of Equation [1.34]. The SNR of a receiver coil represents a balance between a coil's sensitivity to signal arising from a specific point in the sample and the coil's sensitivity to noise arising from the entire sample.

1.8.d SNR Optimization for a Single Coil

The competition between signal and noise embodied in Equation [1.34] can be demonstrated by the well-known determination of the optimum size of a simple circular surface coil (58,59). Consider a simple circular loop coil with radius a placed above an infinite half plane with uniform conductivity σ (for small surface coils, this is a good approximation of the body). For low field strengths (and low temporal frequencies), the magnetic field at a distance z below the coil along its axis can be calculated using the Biot-Savart equation

$$\mathbf{B} = \frac{\mu_0 I}{2} \frac{a^2 \hat{\mathbf{x}}}{\left(a^2 + z^2\right)^{3/2}}. \qquad [1.35]$$

The integral in the denominator of Equation [1.34] can be calculated analytically for a coil with this geometry (59) :

$$\int \sigma \left|\mathbf{E}(\mathbf{r})\right|^2 d^3\mathbf{r} = \sigma \omega^2 \mu_0^2 I^2 \frac{a^3}{3}. \qquad [1.36]$$

From Equation [1.34], we have

$$SNR_{\max} = \sqrt{3} \frac{B_0 \gamma^2 \hbar^2}{\sqrt{\Delta f}\left(4kT\right)^{3/2}} \rho(\mathbf{r}_0)(\Delta V) \sqrt{\frac{a}{\left(a^2 + z^2\right)^3}}. \qquad [1.37]$$

Differentiating this expression with respect to the coil radius a, we see that for a given depth z, the optimum coil radius is $a = z/\sqrt{5}$ (58,59).

In this example, the simple geometry of the coil and the sample made the calculations very easy. The expression in Equation [1.34], however, is a quite general tool for coil design. The equation may be applied to any sample and coil geometry, even if the explicit field calculations become more cumbersome. For coils that are designed to be used at relatively low magnetic field strengths (1.5 T and lower), a simple Biot-Savart calculation is generally used to calculate the fields. At higher field strengths, however, the wave nature of the fields becomes important, and a

full solution to Maxwell's Equations is necessary. The finite difference time domain method has been popular for calculating coil sensitivities at high field strengths (60,61). Another approach to simulating the performance of coils at high field is provided in reference (62).

1.8.e Coil Arrays: Sensitivity and Noise Correlations

Single surface coils achieve a high sensitivity to MR magnetization at a given depth while maintaining limited sensitivity to noise sources in the rest of the sample. The principal drawbacks of surface coils are that a) their spatial sensitivity patterns are non-uniform and b) they have high SNR over limited regions of the sample. In order to provide high SNR over a large field-of-view, arrays of surface coils are used. Each coil in an L-coil array will have a sensitivity equal to

$$C_l(\mathbf{r}) = \left[\hat{\mathbf{B}}_x^{\text{coil}}\right]_l(\mathbf{r}) - i\left[\hat{\mathbf{B}}_y^{\text{coil}}\right]_l(\mathbf{r}). \qquad [1.38]$$

If the coils are combined using a set of coefficients w_l, then the total noise power of the array is given by

$$\begin{aligned}\sigma_{array}^2 &= \frac{4kT\Delta f}{|I|^2}\int\sigma(\mathbf{r})\left|\sum_l w_l\mathbf{E}_l(\mathbf{r})\right|^2 d^3\mathbf{r} \\ &= \frac{4kT\Delta f}{|I|^2}\sum_l |w_l|^2\int\sigma(\mathbf{r})|\mathbf{E}_l(\mathbf{r})|^2 d^3\mathbf{r} + \frac{4kT\Delta f}{|I|^2}\sum_{l,l'\neq l} w_l w_{l'}^*\int\sigma(\mathbf{r})\mathbf{E}_l(\mathbf{r})\cdot\mathbf{E}_{l'}^*(\mathbf{r})d^3\mathbf{r}. \qquad [1.39]\end{aligned}$$

The noise covariance matrix Ψ is given by

$$\Psi_{ll'} = \frac{4kT\Delta f}{|I|^2}\int\sigma(\mathbf{r})\mathbf{E}_l(\mathbf{r})\cdot\mathbf{E}_{l'}^*(\mathbf{r})d^3\mathbf{r}. \qquad [1.40]$$

The field definitions of $C_l(\mathbf{r})$ (Eq. [1.38]) and $\boldsymbol{\Psi}$ (Eq. [1.40]) provide the formal tools for analyzing the SNR of a given coil array. A classic study (1) has employed this formalism to determine the optimum set of weights for combining array data. An explicit application of this formalism for the design of a cardiac coil array for parallel MRI is given in (63). The optimum combination of coil data for parallel imaging specified by Equation [1.15] (11) reduces to that

found in Reference (1) when there is no undersampling. Because the array sensitivities are different at every point, there will be a separate optimum set of weighting coefficients for the reconstruction of each pixel. Incidentally, if the coil sensitivity functions are known, then Equation [1.15] also compensates for non-uniform sensitivity variations (1,11).

1.8.f Depth Penetration and Coil Size

As was outlined earlier, when a single circular surface coil is used for imaging at a depth z, the maximum SNR is achieved when the surface coil radius is equal to $z/\sqrt{5}$. A coil that is smaller than this optimum radius will have a smaller SNR at depth z, and it cannot be used to "see" as far into the sample as an optimized coil can. However, the same thing is not true when smaller coils are organized into arrays. If a large coil is broken into a set of N smaller coils occupying the same area, then the superposition principle for electromagnetic fields implies that a simple combination of smaller coils must give the same sensitivity and the same noise as the larger coil. Because the reconstruction specified by Equation [1.15] is the optimum linear combination of coils, the combined SNR of the array of small coils must be at least high as the SNR of the corresponding large coil.

The SNR of a single large coil that has been optimized for imaging at a depth z below the surface of an infinite half plane with uniform conductivity can be compared to the SNR of an infinite number of smaller coils that make up the same area as the larger coil. When this is done, it is found that the optimum SNR for infinite number of smaller coils is only 40% larger than the SNR of a single depth-optimized coil (59). Of course, the array of smaller coils will have a better SNR at points closer to the array. Still, the modest gain in SNR that is predicted for even an infinite number of coils has provided little motivation for developing arrays with large numbers of elements for conventional gradient-encoded imaging.

1.8.g Coil Interactions

In the preceding discussion of the behavior of coil arrays, it has been assumed that the coils do not interact. That is, the sensitivity of coil l in the presence of the other L-1 coils in the array is the same as the sensitivity of coil l when it is used alone. This assumption will not be true if there is mutual inductance between the two coils. In the presence of mutual inductance, currents that

are induced in a particular coil will themselves induce currents in the other coils. If the mutual inductance is large enough, it may be difficult to have all of the array elements resonate at the same frequencies. Even for smaller amounts of mutual inductance, array elements are expected to share their received signals and noise.

The mutual inductance between two coils can be computed from the overlap integrals of their magnetic fields:

$$M_{ll'} \propto \int \mu \mathbf{B}_l(\mathbf{r}) \cdot \mathbf{B}_{l'}^*(\mathbf{r}) d^3\mathbf{r} \,. \qquad [1.41]$$

Several strategies have been proposed for removing the effects of mutual inductance. First, the overlap of adjacent coil elements may be carefully adjusted so that the shared flux between the two coils is zero (1). Alternatively, capacitive or inductive networks can be built between coils that are able to exactly cancel the mutual inductance between them (64,65). A method for using digital post-processing to emulate the effects of these lumped-element networks has been described computationally (66). Finally, specialized preamplifiers can be designed that present a large impedance to current flow at the input of each coil (1,67). Because very little current can flow in response to the sample magnetization, the interactions between coil elements are limited.

1.9 Practical Design Considerations

In the past few years, a large number of array designs have been proposed with the objective of improved parallel MRI performance. Rather than present a comprehensive review of all of these designs, this section will present select examples that illustrate general design principles.

1.9.a Linear Arrays – Choice of Acceleration Direction

In conventional gradient-encoded MRI, coil array design is largely independent of the choice of pulse sequence. In parallel MRI, however, the two tasks are less separable. As discussed earlier, coil arrays for parallel MRI work best when their elements have sensitivity variation in the direction of k-space undersampling. Therefore, the choice of the k-space sampling strategy – which is traditionally the province of pulse sequence designers – is important for determining the coil array design in parallel MRI.

Consider the example of two-dimensional abdominal imaging in an axial plane. The field of view in these cases is typically rectangular, with the left-right (LR) dimension larger than the anterior-posterior (AP) dimension. It is possible to distribute more coil array elements in the LR direction than in the AP dimension. Therefore, from a coil design perspective, acceleration in the LR dimension is more attractive. On the other hand, in most sequence acquisition strategies, the longer dimension is chosen for the frequency-encode dimension. Acquisition in the frequency-encode dimension is typically limited by the receiver bandwidth and the absolute gradient strength, and so not much speed gain is achieved from undersampling in this direction. While the parallel MRI reconstruction might benefit from a change in phase-encode direction from AP to LR, this strategy would require more phase-encoding steps in order to acquire the baseline image. In other words, this approach would require lengthening the scan time before it was accelerated. Therefore, for 2D axial images, undersampling is most often performed in the AP direction, despite the fact that this direction is more challenging in terms of coil-array spatial encoding.

The preceding example illustrates the intimate and complex connection between coil design and acquisition strategy in parallel MRI. It is true that the most direct method of image acceleration is simply undersampling in the same phase-encode direction that is normally used for imaging. On the other hand, if the g-factor in the LR direction is low enough, the time required to obtain the extra phase-encode steps for sampling in that direction could be offset by reducing the sampling density. Changing the acquisition strategy in order to take advantage of the spatial encoding properties of the array might yield a final image with better SNR while achieving the same net reduction in scan time.

The integrated strategy of combining sequence design with coil design introduces some logistical complexity, but the potential gains are quite promising. This approach has recently been used in the application of a 32-element array to abdominal imaging, where rather than simply accelerating a standard clinical imaging protocol, non-conventional phase-encode directions were chosen in order to achieve a net image acquisition that would otherwise not be possible (68).

1.9.b Importance of Coil Phase

Because the coil sensitivity is a complex valued function of position, it is implicit in the parallel MRI reconstruction algorithm (Eq. [1.15]) that the phases of the coil sensitivities are just as important for spatial encoding as are the magnitudes. This principle was illustrated specifically in a study showing that a crossed butterfly coil and a loop coil could be used for SENSE imaging (40). Even though the magnitudes of the coils' sensitivities had the same basic shape, the phases of their sensitivities were quite different, and thus parallel image reconstruction was possible.

The contributions of coil phase to spatial encoding were also important in the cardiac array design presented in (63). In that study, it was shown that acceleration in the AP direction was aided by constructing a coil array with a larger inter-element spacing than they would have in a conventional array. This spacing had little effect on the relative magnitudes of the coil sensitivities, but it did produce variations in coil phase that were useful in the parallel MRI reconstruction.

1.9.c Multi-Dimensional Encoding

In Section 1.9.a, it was shown that it is important to design coil arrays with sensitivity variation in the direction of the undersampled phase-encoding. However, there are imaging protocols in which several different image planes are acquired, each with a different phase-encoding direction. In addition, there are applications such as cardiac imaging where the precise image plane orientation is dependent on the patient's individual anatomy, which cannot always be predicted beforehand. Finally, it has been shown that parallel MRI performance is maximized in three-dimensional imaging sequences when data are undersampled simultaneously in two phase-encode directions (69). For all of these reasons, it is important to design arrays that are capable of simultaneous encoding in multiple directions.

The most straightforward method of accomplishing multidimensional encoding is by uniformly tiling coils along the surface of a subject's body. This can be realized as either grids on a flat surface or else as arrays of elements that are wrapped entirely around the patient's head or abdomen. The difficulty associated with this tiling approach is that it is an inefficient use of array

elements. If the total number of available receivers is fixed, then there will be fewer elements in any specific direction than there would be in an equivalent linear array. A variety of approaches have been suggested to allow individual coil elements to participate in spatial encoding along several directions at once. A concentric coil has been introduced that uses concentrically placed elements with varying numbers of loops that permit spatial variation in multiple directions (70,71). The design, construction, and validation of this array is the topic of Chapter 2. Triangular-shaped elements have been suggested as another means for accomplishing multidirectional encoding (72). Recently, an array with concentrically-placed elements and a slightly different looping structure than in references (70,71) has also been proposed (73).

1.9.d Use of Volume Coils

While the majority of coil array designs that have been used for parallel MRI have been based on coils with spatially localized sensitivities, so-called volume coils have also been used for their spatial encoding properties. An early example of this approach employed two coils, one with a uniform sensitivity, and the other with a linear gradient in sensitivity (4). Other examples, which were mentioned briefly in Section 1.6.a, were coils whose sensitivities were specifically tailored to produce a single spatial harmonic across the imaging volume (42-44). A second approach has involved constructing a birdcage with two degenerate modes, each with a distinct sensitivity pattern (45). Half-volume birdcage coils (46) and half-volume TEM coils (74) have also been explored.

1.9.e Limited Field-of-View

In making an effort to distribute as many coil elements around the patient as possible, it is important to keep in mind that the best way to accelerate a scan is to keep the time of the fully-encoded scan as short as possible. In order to keep the required field of view as small as possible, arrays should be focused around the desired anatomy as much as possible. Of course, the desire to build arrays with targeted sensitivities needs to be weighed against the competing desire to build arrays that are suited to a variety of patient shapes and sizes.

1.9.f Influence of Field Strength

A lot of attention has recently been given to the design of coil arrays for parallel MRI at magnetic field strengths larger than 1.5 T. It has been shown that the shapes of coil sensitivities

change as the field strength increases (61,75). A coil array at a higher field strength might perform differently than a coil array with the exact same geometry would at a lower field strength (76).

1.10 Experimental SNR Analysis for Parallel MRI

The major criteria for evaluating coil array performance for parallel MRI are based on the SNR of the reconstructed images. However, measuring the SNR of an image that has been reconstructed using parallel MRI is significantly more complicated than it is for images that have been fully acquired using gradient-encoding. Traditionally, the image SNR in MRI has been measured by choosing two regions of interest: one region inside the sample, and one region in the background noise. The mean of the region within the sample is used as the signal and the standard deviation of the region outside of the sample is used as an estimate of the noise.

This traditional approach to measuring SNR is problematic in the context of parallel MRI for two reasons. The first reason is related to the use of magnitude data, rather than complex image pixels. The magnitude operation is non-linear, and it introduces a bias into regions of the image that have low SNR. Even outside of the context of parallel MRI, this can introduce measurement errors. The source of these errors and some suggested corrections are described in Reference (77). The analysis becomes even more complex in parallel MRI because in parallel reconstructions, the SNR for every pixel (and thus the noise bias) is generally different (78). Because of these complications, it is nearly always advisable to perform SNR analyses on complex-valued images.

The second difficulty encountered when measuring the SNR of a parallel MRI-reconstructed image occurs even when complex-valued data are used for the measurement. Because the g-factor is spatially varying, a noise estimate taken in one region (in this case, outside of the sample) is not reflective of the noise in other regions. Furthermore, the noise between pixels in parallel MRI is generally correlated (11) (although, to be fair, the noise is typically not correlated between *adjacent* pixels), and the statistical analysis of an ROI is does not reliably correspond to an equivalent temporal sampling. Finally, many implementations of parallel MRI perform a

masking or other non-linear operation on regions outside of the sample, which will further complicate noise measurements from those regions.

With these complications in mind, there are two practical approaches to evaluating the SNR of parallel MRI data. If the noise covariance matrix, $\mathbf{\Psi}$, and the coil sensitivities, $C_l(\mathbf{r})$, of the array have been measured, then Equation [1.24] can be used to calculate the noise power in each reconstructed pixel, and Equation [1.25] can be used to calculate the g-factor of each pixel. Because the noise in any region of the (complex-valued) image should still have zero mean, an average over that region can be used as a reasonable estimate of the signal. The ratio of the signal to the noise power in each pixel gives the SNR in each pixel, and then an average SNR over the entire region can be reported. The advantage of this approach is that it is simple to implement and readily applicable to *in vivo* acquisitions. The disadvantage is that the SNR of the image is, in some sense, being calculated from a theoretical model and not measured.

An alternative approach involves the use of an imaging phantom (79). A repeated set of undersampled acquisitions is performed and reconstructed using a parallel MRI technique of choice. The mean and standard deviation over the set of replicas for each (complex-valued) pixel in the image is measured, creating an SNR map. The average values over different regions of the SNR map are then reported. Because of the number of repetitions involved, this approach is not practical for *in vivo* imaging. Furthermore, in this approach, both thermal noise and intrinsic system instabilities will contribute to the measured noise. The long-term system instabilities might have various causes, including variations in the RF transmitter power or changes in the temperature of the components that make up the receiver circuitry. The relative contributions of system instabilities to the measured noise (compared to thermal noise) can be minimized by using pulse sequences with relatively low baseline SNR. Some balance is necessary when using this strategy, because if the SNR is too low, more samples will be required to measure each pixel's mean and standard deviation. The resulting increase in scan time may potentially increase the influence of the long-term system variations. Recognizing these subtleties, the phantom-based approach is still attractive because it represents an actual measurement of SNR rather than a model-based computation. This approach is used for all of the SNR measurements in this work, and more details on the precise implementation are provided in the appropriate chapters.

1.11 Summary

This chapter has been devoted to introducing the formalism and basic techniques of parallel MRI, with an emphasis on implications for coil array design. The remainder of the dissertation will build upon these ideas in order to examine three important fundamental and practical issues related to using coil arrays for spatial encoding in MRI. In the next chapter, a concentric coil array will be described for efficiently using four array elements for multidimensional encoding. In the chapter that follows, inductive coupling and its impact on the use of arrays for parallel MRI will be discussed. Finally, a set of theoretical calculations will be presented that seek to establish fundamental limits on the spatial encoding properties of any realistic coil array.

1.12 Appendix A: Encoding Matrix Norm For Different Sampling Patterns

The encoding matrix norm for an accelerated reconstruction is given by

$$\left[\mathbf{B}_R^{\dagger}\boldsymbol{\Psi}^{-1}\mathbf{B}_R\right]_{j,j} = \sum_{(lm),(l'm')} \left[\mathbf{B}_R\right]^{*}_{(l'm'),j} \left[\boldsymbol{\Psi}^{-1}\right]_{(l'm'),(lm)} \left[\mathbf{B}_R\right]_{(lm),j} . \qquad [1.42]$$

Because the noise is uncorrelated between acquired k-space lines, the noise covariance matrix and its inverse are block-diagonal and independent of *m*,

$$\left[\boldsymbol{\Psi}^{-1}\right]_{(l'm),(lm)} = \sum_{m'} \left[\boldsymbol{\Psi}^{-1}\right]_{(l'm'),(lm)} \delta_{m,m'} . \qquad [1.43]$$

Inserting this into Eq. [1.42], we have

$$\left[\mathbf{B}_R^{\dagger}\boldsymbol{\Psi}^{-1}\mathbf{B}_R\right]_{j,j} = \sum_{(lm),(l')} \left[\mathbf{B}_R\right]^{*}_{(l'm),j} \left[\mathbf{B}_R\right]_{(lm),j} \left[\boldsymbol{\Psi}^{-1}\right]_{(l'm),(lm)} . \qquad [1.44]$$

Inserting the definition of the encoding matrix (Eq. [1.13]):

$$\begin{aligned} \left[\mathbf{B}_R^{\dagger}\boldsymbol{\Psi}^{-1}\mathbf{B}_R\right]_{j,j} &= \sum_{(lm),(l')} C_l^{*}(\mathbf{r}_j) e^{-i\mathbf{k}_m\cdot\mathbf{r}_j} C_{l'}(\mathbf{r}_j) e^{i\mathbf{k}_m\cdot\mathbf{r}_j} \left[\boldsymbol{\Psi}^{-1}\right]_{l',l} \\ &= \sum_{(lm),(l')} C_l(\mathbf{r}_j) C_{l'}^{*}(\mathbf{r}_j) \left[\boldsymbol{\Psi}^{-1}\right]_{l',l} \\ &= n_k^R \sum_{l,l'} C_l(\mathbf{r}_j) C_{l'}^{*}(\mathbf{r}_j) \left[\boldsymbol{\Psi}^{-1}\right]_{l',l} \end{aligned} , \qquad [1.45]$$

Where n_k^R is the number of k-space lines in the undersampled acquisition. Note that this expression does not depend on the details of the k-space sampling strategy. If we replace the encoding matrix for the accelerated scan, $\mathbf{B}_R$, with the encoding matrix for the unaccelerated scan, $\mathbf{B}_1$, using the same coil array,

$$\begin{aligned}\left[\mathbf{B}_1^{\dagger}\boldsymbol{\Psi}^{-1}\mathbf{B}_1\right]_{j,j} &= n_k^1\sum_{l,l'} C_l(\mathbf{r}_j)C_{l'}^{*}(\mathbf{r}_j)\left[\boldsymbol{\Psi}^{-1}\right]_{l',l} \\ &= Rn_k^R\sum_{l,l'} C_l(\mathbf{r}_j)C_{l'}^{*}(\mathbf{r}_j)\left[\boldsymbol{\Psi}^{-1}\right]_{l',l}. \\ &= R\left[\mathbf{B}_R^{\dagger}\boldsymbol{\Psi}^{-1}\mathbf{B}_R\right]_{j,j}\end{aligned} \qquad [1.46]$$

This is the expression given in Eq. [1.24].

Chapter 2.
Concentric Coil Arrays for Multidimensional Spatial Encoding in Parallel MRI

2.1 Introduction

Arrays of surface coils that are designed for parallel MRI are usually tiled in either one-dimensional strips or two-dimensional grids. Arrays that are aligned in strips perform very well when used to reconstruct undersampled data along the principal axis of the array, but they can perform poorly when the undersampled data are disposed in a direction perpendicular to the array. Grid-type arrays provide multiple dimensions of spatial encoding, but when the number of coil elements is fixed, these arrays provide fewer coils in any given direction than their one-dimensional counterparts. Reducing the inductive coupling interactions between coils in a two-dimensional array can also be challenging.

This chapter presents an alternative method for arranging coils within an array. Coils are not tiled spatially, but are instead placed concentrically on top of each other. The conductor path of each coil element is crossed to produce periodic alterations in current density that minimize the mutual inductance and correlated noise between array elements. The spatial encoding properties

of this array, which we call a "concentric coil array," reflect the advantages of the varying phase (40) as well as the varying magnitude of each coil's spatial sensitivity pattern.

We begin with a general theoretical description of concentric coil arrays, and proceed to discuss the symmetry conditions that are necessary for canceling mutual inductance and noise correlations. We present calculations that determine the optimum size for concentric array elements at a specific depth. We then describe the construction of a 4-element concentric array, and compare the performance of this array with that of more conventional array designs. In particular, we explore the sensitivity of candidate coil arrays to changes in the direction of undersampling.

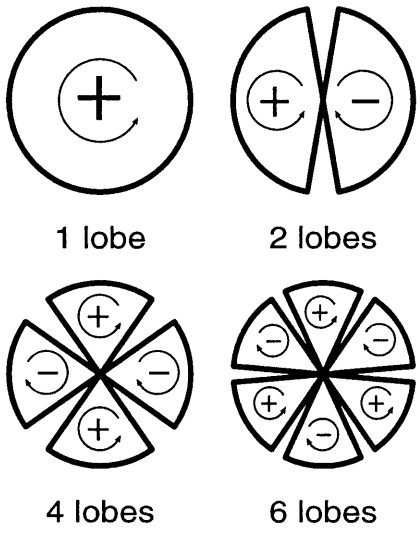

Figure 2.1 Examples of concentric elements with various numbers of lobes. The individual lobes are portrayed as circular segments, but this need not be the case in practice.

2.2 Theory

The current path of each element in a concentric array is divided into a series of "lobes" (Figure 2.1). The currents that flow in successive lobes are equal in magnitude but they flow in the opposite directions. A 1-lobed coil is the familiar single loop coil, and a 2-lobed coil is equivalent to a so-called "butterfly" coil, which is often combined as a quadrature pair with a loop coil. The use of a single loop and a 2-lobed coil for parallel imaging has been described previously (40). The coil elements shown in Fig. 2.1 are drawn with current lobes in the shape of circular arcs. In practice, these current lobes may be any shape, as long as the required symmetry of the current pattern is maintained. When concentric coil elements are placed in an array, the symmetries in their currents allow both for inductive isolation and for reduction of correlated noise. The conditions for isolation are described in the following sections.

2.2.a Mutual Inductance

The inductive isolation between a simple loop coil and a 2-lobed coil is familiar and straightforward. If the two coils are placed concentrically, then the magnetic flux that passes through the loop coil due to a single lobe of the 2-lobed coil must be equal and opposite to the magnetic flux that is generated by the second lobe of the 2-lobed coil. Thus, the coils have zero mutual inductance.

The situation is more complex when the number of lobes in each coil is arbitrary. We derive the conditions for inductive isolation by considering two planar concentric coils placed on top of an infinite sample that has uniform conductivity σ. The mutual inductance, M_{12}, between two coils is proportional to the overlap integral of the magnetic fields, $\mathbf{B}_1$ and $\mathbf{B}_2$, that are generated by the currents, I_1 and I_2, flowing in each coil

$$M_{12} = \frac{\mu_0}{I_1 I_2} \int \mathbf{B}_1 \cdot \mathbf{B}_2 d^3\mathbf{r} \ . \qquad [2.1]$$

The coils will be inductively isolated if they satisfy one of two symmetry conditions. The first symmetry condition relies on the behavior of the currents upon reflection by a plane. An *n*-lobed coil has *n/2* planes of reflection symmetry. Reflection about these planes of symmetry leaves the

rotational direction of each lobe's current unchanged (Figure 2.2a). Because the lobe currents do not change when they are reflected, the magnetic field that they generate will also have reflection symmetry. Formally, a plane of symmetry can be denoted by a vector, **s**, and the operator that reflects a vector about that plane is $\mathbf{P}_s$. The reflection symmetry of the magnetic field is written as,

$$\mathbf{B}(\mathbf{P}_s\mathbf{r}) = \mathbf{P}_s\mathbf{B}(\mathbf{r}). \qquad [2.2]$$

An *n*-lobed coil also has *n/2* antisymmetric planes (Figure 2.2b). When a coil is reflected about an antisymmetric plane, the current flowing in each of the coil's lobes is inverted. When the coil's magnetic field is reflected about an antisymmetric plane, **a**, the magnetic field is inverted:

$$\mathbf{B}(\mathbf{P}_a\mathbf{r}) = -\mathbf{P}_a\mathbf{B}(\mathbf{r}). \qquad [2.3]$$

When two concentric coils are aligned such that a symmetric plane, "$\mathbf{s}_1$," from one coil coincides with an antisymmetric plane, "$\mathbf{a}_2$," from a second coil then the dot product of their magnetic fields is antisymmetric upon reflection by this common axis $\mathbf{P} \equiv \mathbf{P}_a = \mathbf{P}_s$:

$$\mathbf{B}_1(\mathbf{Pr}) \cdot \mathbf{B}_2(\mathbf{Pr}) = -\mathbf{P}\mathbf{B}_1(\mathbf{r}) \cdot \mathbf{P}\mathbf{B}_2(\mathbf{r}) = -\mathbf{B}_1(\mathbf{r}) \cdot \mathbf{B}_2(\mathbf{r}). \qquad [2.4]$$

The antisymmetric dot product causes the overlap integral in Equation [2.1] to vanish, and the two coils are inductively isolated.

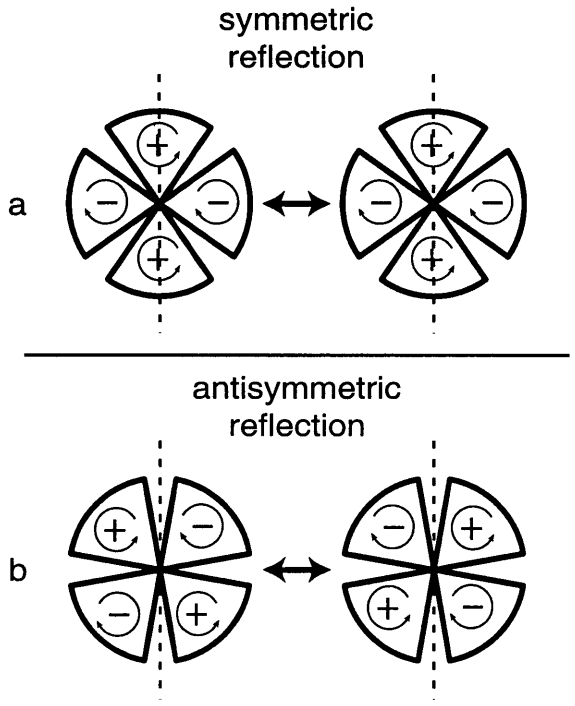

Figure 2.2 Examples of the symmetric (a) and antisymmetric (b) reflection planes of a 4-lobed coil.

The second condition for coil isolation is based on the rotational symmetries of the coils. When a coil with n lobes is rotated by an angle $2\pi/n$, then the current in each lobe is inverted (Figure 2.3a). If $\mathbf{R}(\theta)$ is a matrix that causes a rotation θ about the y-axis,

$$\mathbf{R}(\theta)=\begin{bmatrix}\sin(\theta) & 0 & \cos(\theta)\\ 0 & 1 & 0\\ \cos(\theta) & 0 & -\sin(\theta)\end{bmatrix}, \qquad [2.5]$$

the current density and the magnetic field of an n-lobed coil have the symmetries

$$\mathbf{J}^n\left(\mathbf{R}\left(w\frac{2\pi}{n}\right)\mathbf{r}\right)=(-1)^w\mathbf{R}\left(w\frac{2\pi}{n}\right)\mathbf{J}^n(\mathbf{r})$$
$$\mathbf{B}^n\left(\mathbf{R}\left(w\frac{2\pi}{n}\right)\mathbf{r}\right)=(-1)^w\mathbf{R}\left(w\frac{2\pi}{n}\right)\mathbf{B}^n(\mathbf{r}) \qquad w=1\ldots n. \qquad [2.6]$$

In Appendix A (Section 2.7), it is shown that if an *m*-lobed coil is placed on top of an *n*-lobed coil, and *d* is the greatest common denominator of *m* and *n*, then the integral in Eq. [2.1] will be zero as long as exactly one of the integers, *m/d* and *n/d,* is odd. This condition for decoupling depends only on the ratio between the numbers of lobes in the two coils, and makes no assumption about their relative orientations. Figure 3b supplies examples of coil pairs in which this condition is and is not satisfied. A 4-lobed coil will be inductively isolated from a 2-lobed coil ($d=2, m/d=1, n/d=2$), but a 6-lobed coil will not be isolated from a 2-lobed coil ($d=2$, $m/d=1$, $n/d=3$). While the 6- and 2-lobed coils (when used together) do not meet the conditions for decoupling based on angular symmetry, they can still be isolated by aligning their symmetric and antisymmetric reflection planes according to Eq. [2.3].

2.2.b Noise Correlations

The noise correlation between two coil elements is proportional to the overlap integral of the electric fields produced by currents in those two coils (1):

$$k_{12}=\frac{1}{I_1 I_2}\int\sigma\mathbf{E}_1\cdot\mathbf{E}_2^* d^3\mathbf{r}\ . \qquad [2.7]$$

If the sample is homogeneous and much larger than the coil, the electric field will share the rotational symmetries of the current density and the magnetic field (Eq. [2.6]):

$$\mathbf{E}^n\left(\mathbf{R}\left(w\frac{2\pi}{n}\right)\mathbf{r}\right)=(-1)^w\mathbf{R}\left(w\frac{2\pi}{n}\right)\mathbf{E}^n(\mathbf{r}) \quad w=1\ldots n \qquad [2.8].$$

The same conditions of rotational symmetry that make the mutual inductance zero will also cause the overlap integral in Eq. [2.7] to be zero.

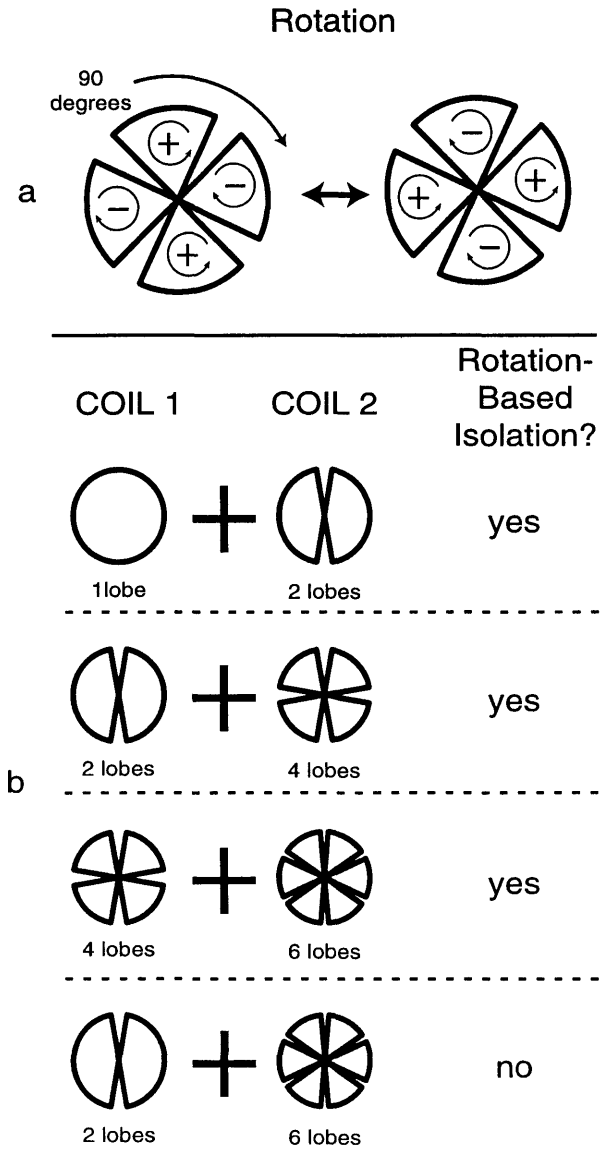

Figure 2.3 (a) Illustration of the rotational symmetry of a 4-lobed coil. A 90 degree rotation causes inversion of all of the lobe currents. (b) Pairs of coils that do and do not meet the rotation symmetry condition for electrical isolation.

The reflection symmetries of the electric field are opposite to those of the magnetic field (the fields are related to each other by a cross product), and therefore

$$\begin{aligned} \mathbf{E}(\mathbf{P}_s\mathbf{r}) &= -\mathbf{P}_s\mathbf{E}(\mathbf{r}) \\ \mathbf{E}(\mathbf{P}_a\mathbf{r}) &= \mathbf{P}_a\mathbf{E}(\mathbf{r}) \end{aligned} . \qquad [2.9]$$

When symmetric and antisymmetric planes of two coils coincide, the dot product of their electric fields is odd with respect to reflection. The reflection symmetry condition and rotational symmetry condition for removal of mutual inductance therefore both apply to the removal of noise correlations as well.

2.3 Methods

2.3.a Simulations of Coil Array Performance

The performance of candidate concentric coil array designs was evaluated for both parallel imaging and conventional gradient-encoded imaging by following the method outlined in (63). This method requires calculation of the spatial sensitivity pattern of each coil, $C(\mathbf{r})$, and the noise covariance matrix, $\boldsymbol{\Psi}$. The diagonal elements of $\boldsymbol{\Psi}$ correspond to the total noise variance in each coil, while the off-diagonal elements of $\boldsymbol{\Psi}$ describe the noise correlations between pairs of coils.

The Biot-Savart law was used to calculate the magnetic field per unit current generated by the coil, $\hat{\mathbf{B}}^{\text{coil}}(\mathbf{r})$, and the sensitivity pattern was determined using the principle of reciprocity (80),

$$C(\mathbf{r}) = \hat{\mathbf{B}}_x^{\text{coil}}(\mathbf{r}) - i\hat{\mathbf{B}}_y^{\text{coil}}(\mathbf{r}). \qquad [2.10]$$

The noise power in each coil was calculated by integrating the square of the electric field produced by a unit current in each coil (1). Analytical expressions were used to compute the sample-induced noise in rectangular coils, 2-lobed coils and 4-lobed coils. The derivation of these analytical expressions is described in Appendix B (Section 2.8). As discussed earlier, appropriately selected concentric coil elements should experience no noise correlations and so the noise covariance matrix is diagonal.

2.3.b Concentric Coil Array Prototype

In order to take advantage of the analytical expressions for noise power, the initial prototype concentric coil array was built with rectangular lobes (Figure 2.4). Four elements were constructed on two sides of a PVC substrate. Two 2-lobed coils were placed on the front (anterior) side of the circuit board and a square loop was placed together with a 4-lobed coil on the back of the circuit board. The exact dimensions of each element are shown in the figure.

Precise alignment of the coil array elements was required to meet the symmetry conditions required for inductive isolation. This alignment was achieved by specifying the conductor paths using the Gerber plotting language (*Barco Graphics NV, Gent, Belgium*). The coil elements were then milled from a copper sheet using a computer-controlled router (*Quick Circuit 7000, T-Tech, Inc. Atlanta, GA)*. The conductor paths in all of the coils were 0.25 inches wide. Capacitors were distributed symmetrically along each current path. In situations where the conductor paths crossed, 0.25-inch copper tape was added, together with electrically insulating adhesive tape to separate each layer.

Reflection (S11) and transmission (S12) parameters were measured using a network analyzer and a multiport test set (*Model 8712ES Agilant Technologies*). Each coil was connected to a matching network similar to that found in (1). Coils were matched to 50 ohms at 63.86 MHz when placed on a human chest, and a pin-diode deactivation circuit isolated each coil during body coil transmit. Shielded baluns[2.1] were added at the input of each coil to reduce cable currents. Each coil was connected to low-impedance preamplifiers (*NMP-001, Nova Medical, Wakefield MA USA*).

[2.1] Baluns supplied by R. Giaquinto of General Electric Global Research Center, Niskayuna NY

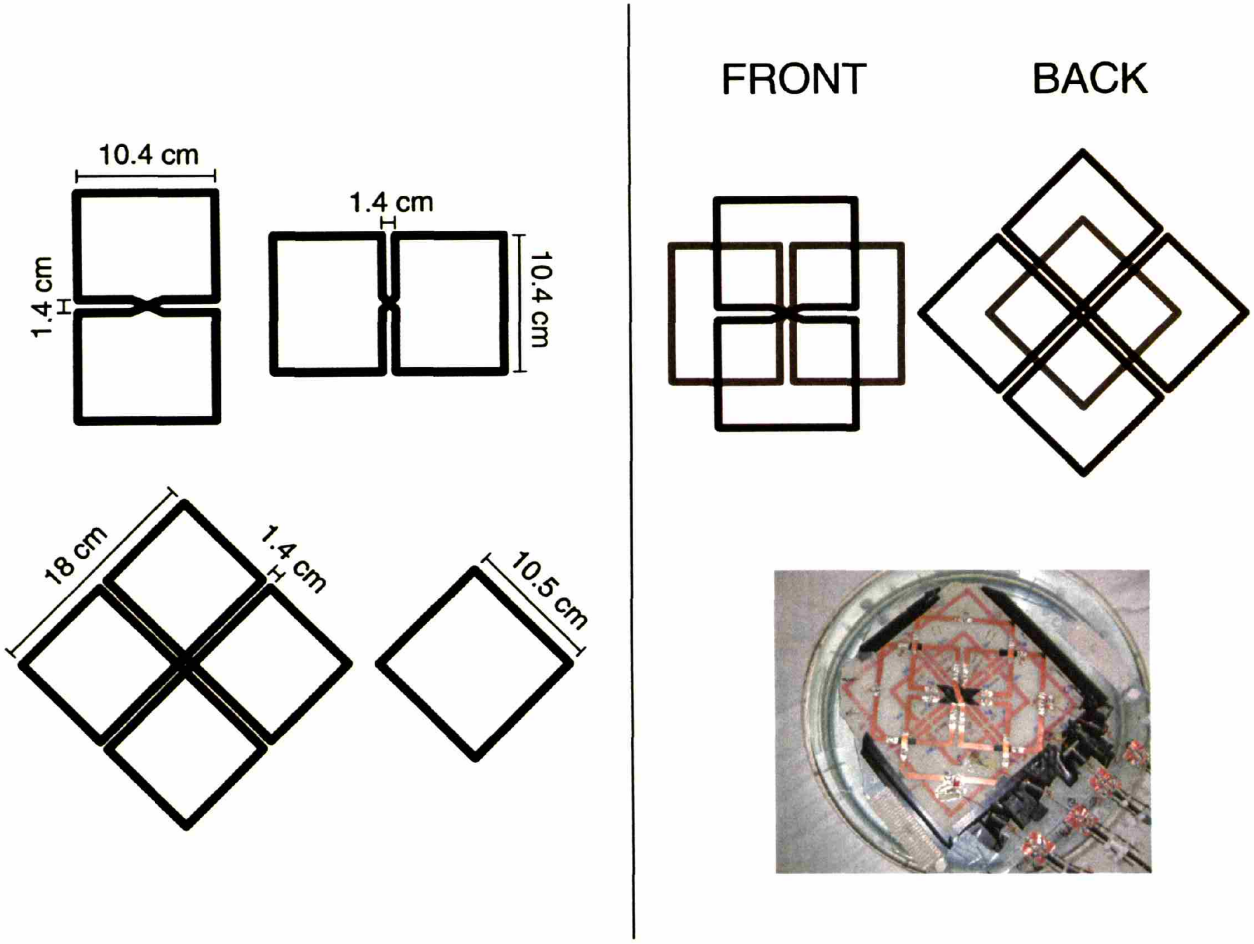

Figure 2.4 Schematic layout and photograph of the prototype concentric array.

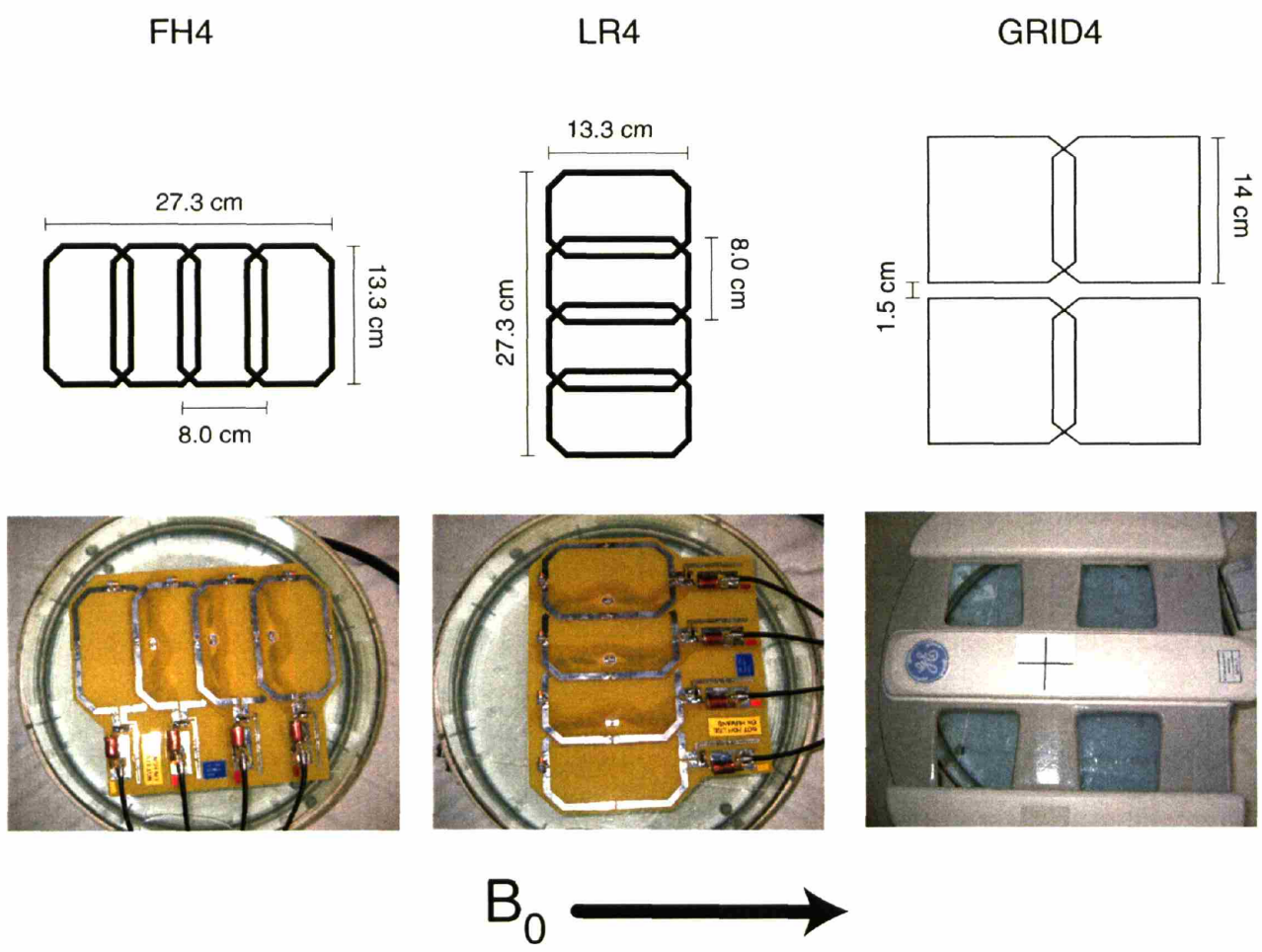

Figure 2.5 Schematic diagrams and photographs of the 4-element arrays used for comparison with the concentric array. See text for a detailed description of each array.

2.3.c Comparison Arrays[2.2]

Three general arrangements of coil elements were considered as alternatives to the concentric array. These alternatives included (Figure 2.5):

1. 4 rectangular elements distributed linearly from left to right (LR4)
2. 4 rectangular elements distributed linearly from foot to head (FH4)
3. 4 rectangular elements arrayed in a 2x2 grid (GRID4)

The LR4 and FH4 coils consisted of the same physical array of four elements rotated by 90 degrees. The array was originally constructed for a different study. Each rectangular element in the array had dimensions 8.0 x 13.3 cm. The four elements were arranged in a straight line with a fixed inter-element overlap of 1.6 cm that eliminated the inductive coupling between adjacent elements. Each coil element had distributed capacitors, a pin-diode-activated blocking network, and shielded baluns.

The 2 x 2 grid array consisted of the anterior four elements from a clinical 8-channel cardiac array (*GE Medical Systems, Waukesha Wisconsin*). Each element was 14 x 14 cm. The elements were overlapped in the foot-head direction but gapped by 1.5 cm in the left-right direction.

2.3.d Image Acquisition

Each candidate coil array was placed on top of a cylindrical imaging phantom with a diameter of 40cm. The coil and phantom were then placed at the isocenter of a 1.5 T General Electric TwinSpeed Scanner (*GE Medical Systems, Waukesha Wisconsin*).

Images were acquired in five different image planes (Figure 2.6). The first image plane was sagittal, and the remaining planes were rotated from the sagittal plane into the axial plane with angles of 22, 45, 67, and 90 degrees about the central axis of the phantom. Two sets of 128 identical gradient-echo acquisitions (TE 3.3-4.0 ms, TR 6.7-8.4 ms, flip angle 1°, BW 15.63 kHz, slice thickness 5 mm, matrix size 128 x 128, FOV 32 cm) were obtained for each image plane. The variation in values for TE and TR reflect changes in gradient performance for different

[2.2] The LR4/FH4 array was constructed by R. Giaquinto of General Electric Global Research Center, Niskayuna NY

image planes, but TE and TR were held constant for the acquisition of any given image plane. The first set of 128 images comprised the data for the parallel image reconstructions. The second set of 128 images was averaged in order to generate coil sensitivity information with high signal-to-noise. The boundaries of each image plane in the direction parallel to the coil array were chosen so that the image plane was contained entirely within the phantom. This choice of image plane was intended to eliminate the influence of the phantom's boundaries on the parallel image reconstructions. Aliasing of the fully-sampled data was avoided by placing the (oversampled) frequency-encode along the axis that was contained entirely within the phantom. The central 51 lines of the image (containing the phantom in the phase-encode direction) were extracted from each image and used as data for the parallel imaging reconstruction (Figure 6). In order to make the data appropriate for both 2- and 3-fold accelerations, the outer eight pixels were removed from the frequency-encode direction, giving a net matrix size of 51x120, and a net FOV of 25x12.75 cm.

Noise data were taken from the signal-free region of all of the 128 repetitions within each acquisition. The noise samples from each coil, l, were placed together in a long column vector, $\mathbf{n}^l$, and the noise covariance matrix, Ψ, was computed as

$$\Psi_{ll'} = \sum_j n_j^l \left(n_j^{l'}\right)^* . \qquad [2.11]$$

Undersampled data sets were generated from the fully-sampled images by extracting those lines of the raw k-space data that would have been obtained in an undersampled acquisition. As mentioned above, we wished to emulate undersampling in the direction transverse to the coil array, which was the *frequency-encode* direction for our acquisitions. We chose to acquire this direction with frequency-encoding so that the field-of-view could be kept to a reasonable size within the 40 cm phantom.

Each undersampled image was reconstructed using a cartesian SENSE reconstruction (11) using *in vivo* coil sensitivities (thus, there was no need for a body coil reference (16)). No extra sensitivity processing or numerical conditioning such as that used in (11) or (16) was employed.

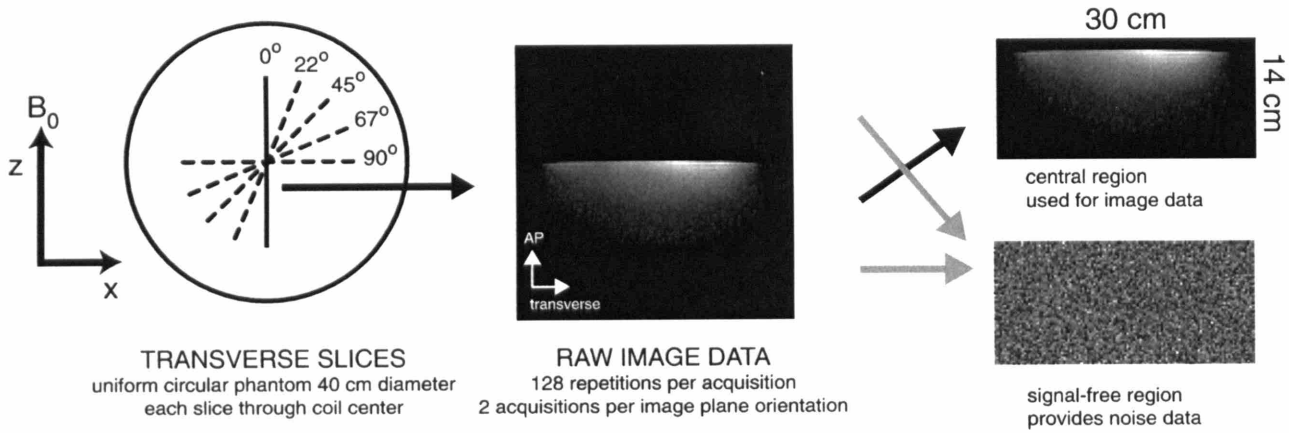

Figure 2.6 Illustration of the data acquisition procedure, including the selection of image plane orientations and data for reconstruction. An identical procedure was used for each comparison array.

Cardiac images were acquired in a short-axis and a long-axis image plane using a cardiac-triggered SSFP pulse sequence with the coil placed on the chest of an adult male volunteer. For each image plane, two identical acquisitions of 20 cardiac phases each were acquired in a single breath hold. The images from 20 phases of one acquisition were averaged together to yield a sensitivity data set with high SNR and low spatial resolution. Image data was obtained by decimating the second data set in k-space, extracting those points that would correspond to 2- and 3-fold undersampled acquisitions. Noise data were obtained by using a small signal-free region of each complex-valued image. As with the reconstructions of the phantom data, no body-coil image was used.

2.3.e SNR Measurement

SNR was quantified by performing parallel imaging reconstructions on all 128 identical acquisitions. The pixel-by-pixel mean taken over all acquisitions was used as an estimate of the signal and the pixel-by-pixel standard deviation was used as a measure of the noise. Thus, a pixel-by-pixel SNR map was created.

We computed the geometry factor, or "g-factor," which is defined for pixel j as (11)

$$g_j = \frac{SNR_{full}(j)}{\sqrt{R} \cdot SNR_R(j)}, \qquad [2.12]$$

where R is the acceleration factor or amount of undersampling; $SNR_{full}(j)$ and $SNR_R(j)$ refer to the SNR of the fully gradient-encoded image and the R-fold accelerated parallel MR image, respectively. The g-factor is always greater than 1, and reflects SNR losses due to the non-unitary transformations involved in the parallel imaging reconstruction.

Each candidate 4-element coil array was built with a slightly different spacing between the elements of the coil array and the phantom. These differences were calibrated by placing a small saline bag on top of each array and then measuring the distance in the MR image between the saline bag and the top of the water within the phantom. Naturally, the saline bag was removed before making SNR measurements. All measurements reported in this chapter were made at a

given depth *measured from the coil conductors*. Note, however, that the GRID4 array was a clinical array and was surrounded by cushioning and insulation. Because it was difficult to determine the exact location of the conductor elements, the depth measurements for this coil likely have more uncertainty than they do for the other candidate coil arrays.

2.4 Results

2.4.a Coil Size Optimization

The sensitivity pattern of a multi-lobed coil depends on its orientation with respect to the main magnetic field (Figure 2.7a). When a 2-lobed coil is placed with its crossed conductors parallel to the main field, the coil has maximum sensitivity at its center. As the coil is rotated, its sensitivity pattern changes until at last there is a linear null in the center of its sensitivity pattern. At this angle, there are a pair of sensitivity peaks displaced some distance from the coil center. The spatial sensitivity of a 4-lobed coil shows a crossed pattern, which rotates together with the coil. The signal null directly below the center of the 4-lobed coil is always present.

Because coils with multiple lobes often do not have SNR maxima directly below their centers, the SNR for these coils was characterized by calculating the maximum SNR achieved in the entire image plane. At a depth of 10 cm, the 1-lobed coil reaches an SNR maximum when its diameter is about 8 cm (Figure 2.7b). This is consistent with the generally accepted result for a simple loop coil (58,59). When the 2-lobed coil is oriented at 0 degrees (and its aspect ratio is kept constant), the SNR maximum occurs at a much larger overall coil size. The peak in SNR for the 4-lobed coil similarly occurs at a larger coil size than either the 1- or 2-lobed coils. The values of the peak SNRs for the 2- and 4-lobed coils are lower than the peak SNR for a simple loop. However, the peaks in SNR for the multi-lobed coils are broader than the peak in SNR for the loop coil.

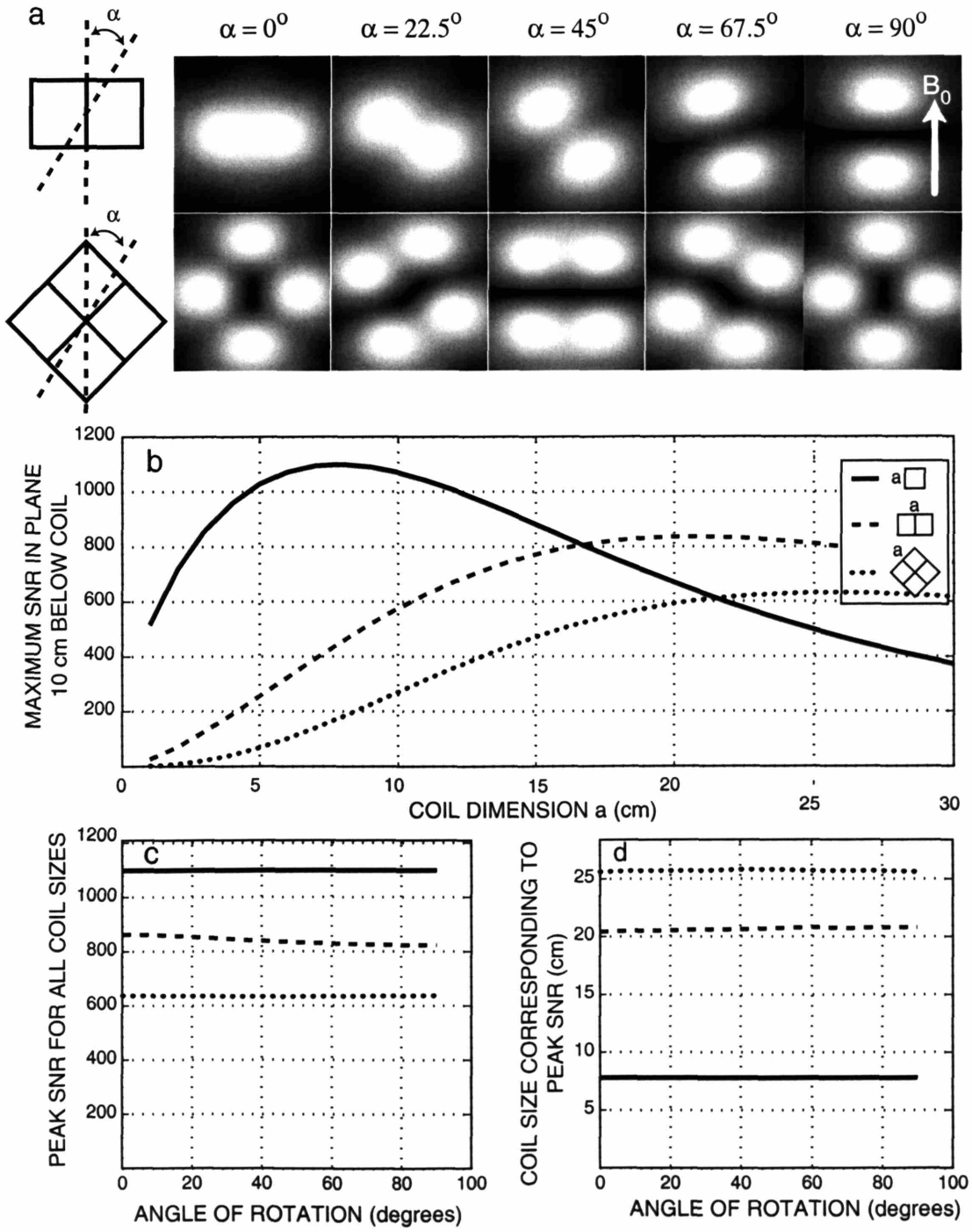

Figure 2.7 a) Sensitivity of concentric elelements as a function of axial rotation. b) Size optimization of 1-, 2-, and 4-lobed concentric coils. c) Peak value of SNR vs. coil size as a function of axial rotation for each coil. d) Coil sizes leading to the peak SNR values shown in (c).

While the spatial distribution of concentric coil sensitivities can change dramatically as the coils are rotated, the height of the SNR peaks show very little variation as a function of angle (Figure 2.7c). The optimum coil sizes for concentric coils also change by only a small amount when the coils are rotated (Figure 2.7d). The broad SNR peaks of concentric coils together with their angular invariance imply that coil size and angular orientation are adjustable parameters when choosing a coil array layout.

2.4.b Concentric Array Bench Test and Measured Sensitivity Profiles

Plots of the reflection coefficient for each of the four coils in the prototype 4-element concentric array (Fig. 2.4) are shown in Figure 2.8a. There is a single peak in the reflection coefficient for each coil. The isolation between each pair of coil elements measured at 63.86 MHz (Table 2.1) ranges from a minimum of –10.4 dB to a maximum of –35.1 dB.

Coronal images of a phantom acquired using each component coil (Figure 2.8b) are consistent with the expected simulated sensitivity profiles. The slight asymmetry in the amplitude of some coils' sensitivity profiles – particularly 2-lobed coil B and the 4-lobed coil – most likely reflects a small amount of residual inductive coupling between array elements.

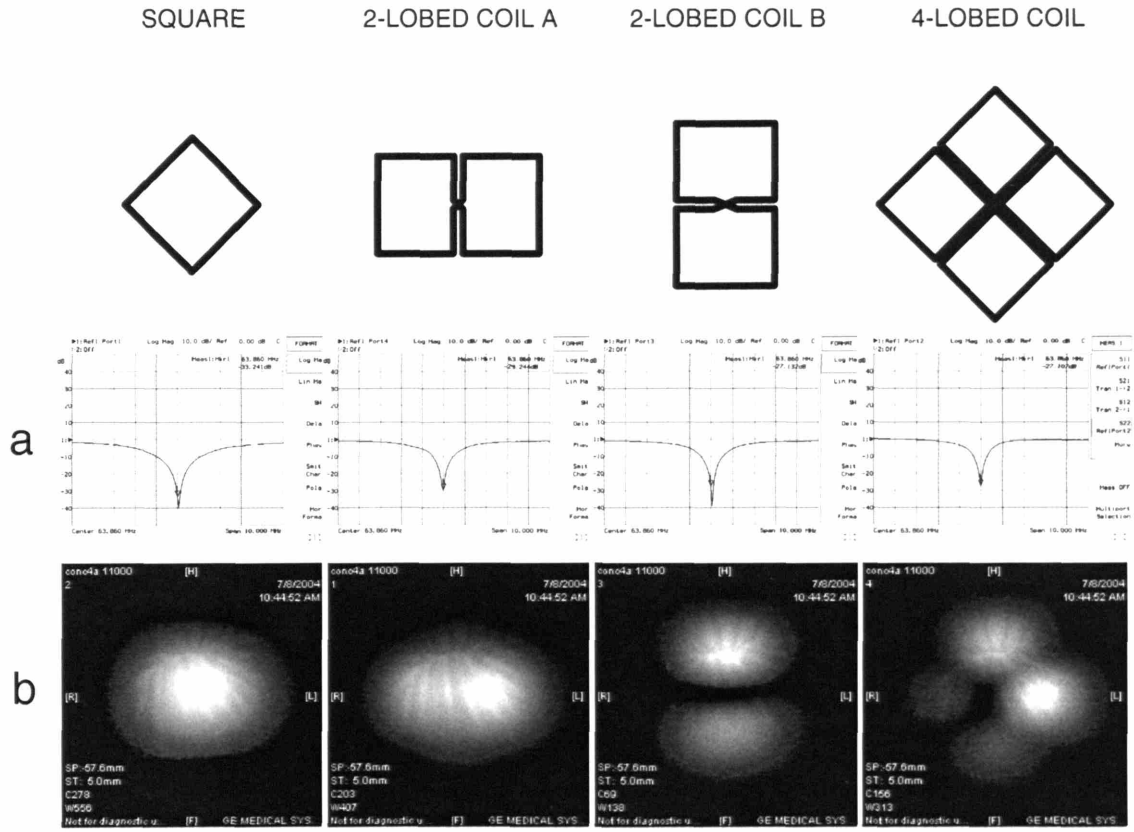

Figure 2.8 a) Measurements of the reflection coefficient for each array element. b) Sample coronal images of a uniform phantom obtained from each element in the concentric array.

2.4.c Array Performance – Baseline SNR

Each 4-element array considered in this work has an overall SNR profile (in the absence of parallel imaging) that reflects the distribution and spatial extent of the coil elements within each array (Figure 2.9a, first row). Because the TE and TR were different for every image plane angle (see Section 2.3.d), the SNR values for different image plane angles are not directly comparable.

However, the SNR values of different arrays for the same image plane angles are comparable. At a depth of 8 cm below the plane of the coil, the concentric array (red trace) has an SNR equal to or greater than all of the comparison arrays at all angles. When the imaging plane is oriented along the main axis of either the FH4 or LR4 arrays (green and brown traces, respectively), these arrays have broad SNR profiles, but their SNR profiles become much narrower in planes perpendicular to their main coil axes.

The SNR profile of the concentric array, along with the GRID4 array (blue trace), demonstrates very little change as a function of angle. The SNR profile of the GRID4 array is broader than that of the concentric array, but the actual SNR value is lower.

2.4.d Array Performance – Accelerated Imaging

When the 4-element arrays are used in parallel imaging reconstructions of 2- and 3-fold undersampled data (Figure 2.9a, second and third rows), their SNR decreases correspondingly. The pattern of noise amplification – which is quantified by the g-factor – has a characteristic peaked pattern for each acceleration factor (Figure 2.9b).

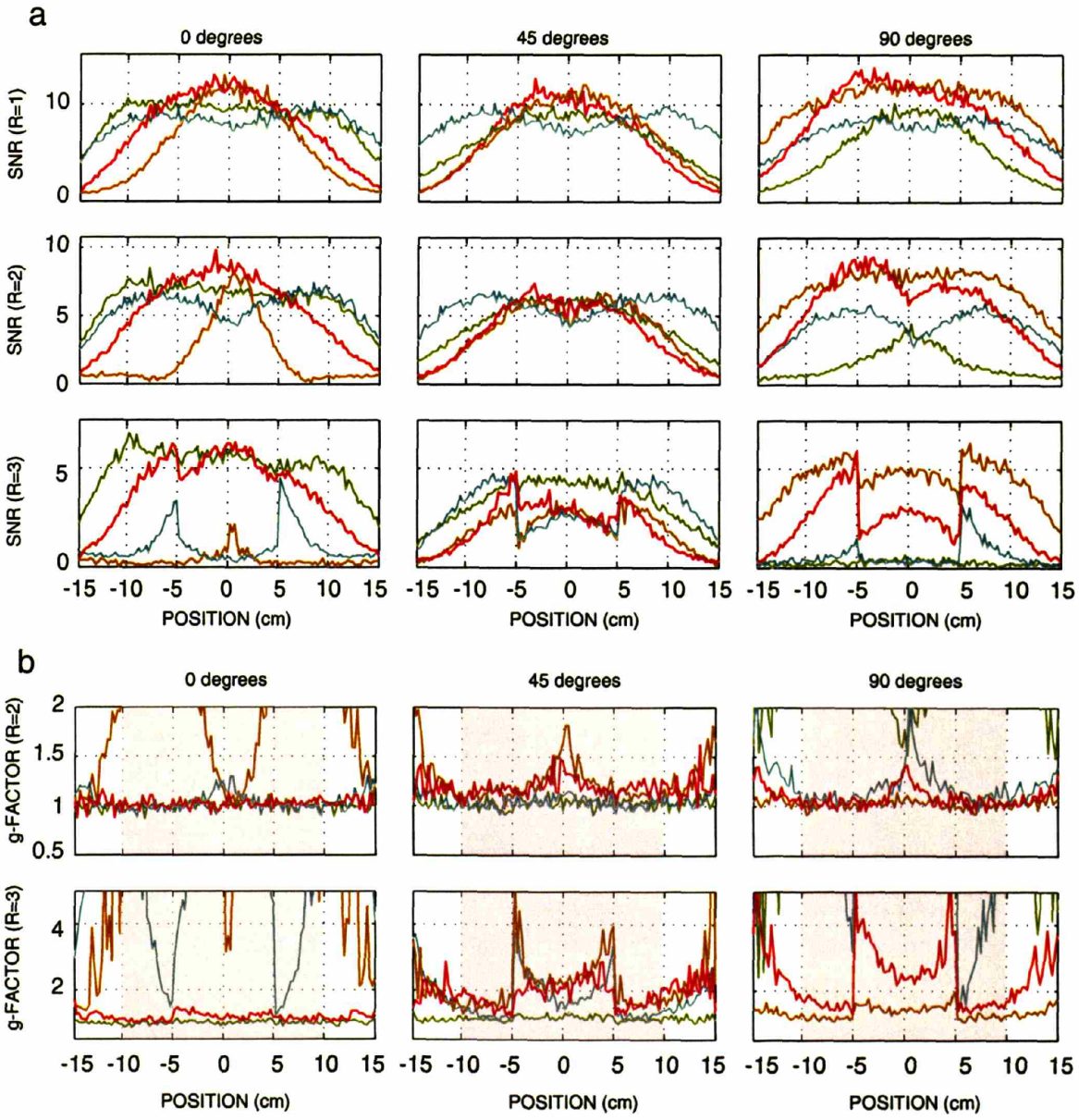

Figure 2.9 SNR (a) and g-factor (b) profiles through the center of the phantom 8 cm below coil array elements for various image planes (see text for information about depth measurements). Shaded regions of g-factor plot indicate region used for g-factor averages in Fig. 2.10.

The peak value of each g-factor profile as well as the average g-factor measured over the central 20 cm (indicated by the shaded region of Figure 2.9b) is shown as a function of image plane orientation in Figure 2.10. At an acceleration factor of 2, the concentric array and the GRID4 array have average g-factor values below 1.3 for all image plane orientations. The two linear arrays have low g-factors when the image plane orientation is aligned with the arrays, but they have much larger g-factors when the image plane is perpendicular to the array axes.

At an acceleration factor of 3, the arrays all have correspondingly higher g-factors. The variation of g-factor with angle for each array is similar to that seen at an acceleration factor of 2, with some important exceptions. The GRID4 array has a g-factor greater than 5 for an acceleration factor of 3 in the 0- and 90-degree image planes, while the same array has a g-factor of less than 1.5 in both image planes at an acceleration factor of 2. The concentric array performs less well in the 67- and 90-degree image planes for 3-fold accelerated imaging than it does for the same image planes and a 2-fold acceleration. However, the concentric array is the only array that has an average g-factor less than three for 3-fold accelerated imaging in both the 0- and 90-degree image planes.

2.4.e Array Performance – In-Vivo Imaging

The reconstructed images of a single cardiac phase from the short- and long-axis cardiac acquisitions are shown in Figure 2.11. The images show adequate sensitivity throughout the myodcardium. There are no visible image artifacts in the accelerated images, except for the loss in signal-to-noise that would be expected when using parallel imaging. Both the accelerated and the unaccelerated images show a small amount of residual of geometrical distortion because our reconstruction did not include a "gradwarp" correction for gradient non-linearities.

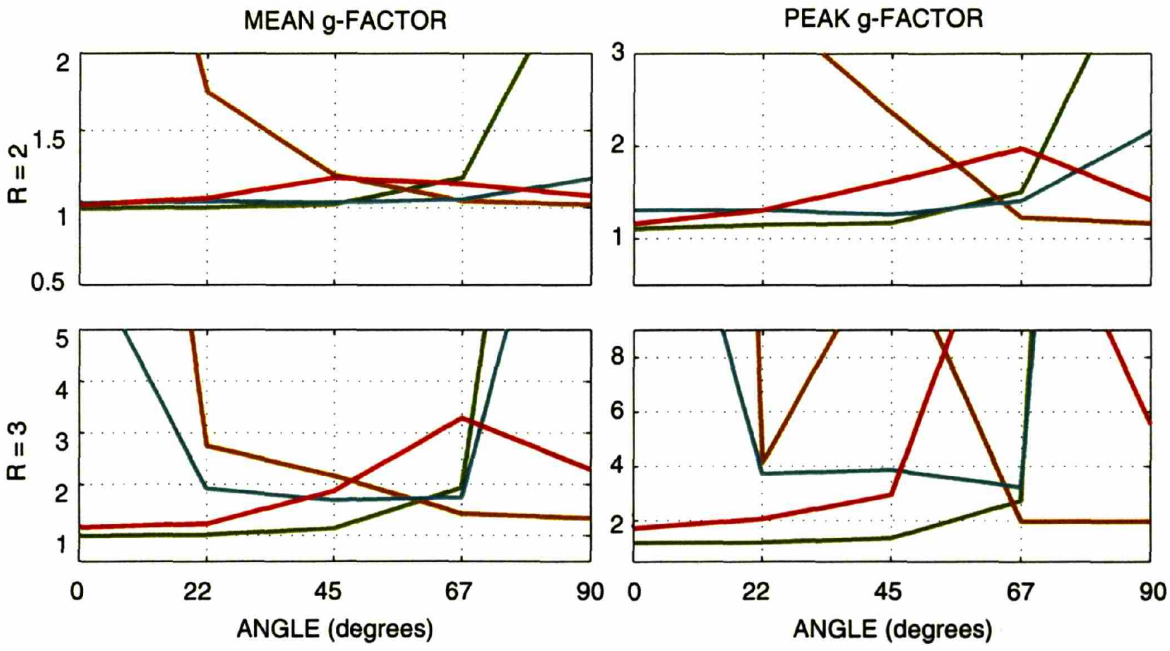

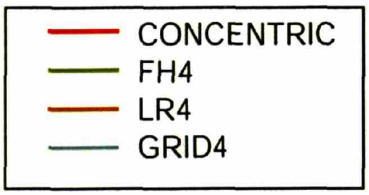

Figure 2.10 (a) average and (b) peak g-factor measured from each transverse image plane at a depth of 8 cm below coil array elements (see text for information about depth measurements). Average and peak measurements are made using the central 20 cm of the image plane, indicated by the shaded regions of the plots from Fig. 2.9b.

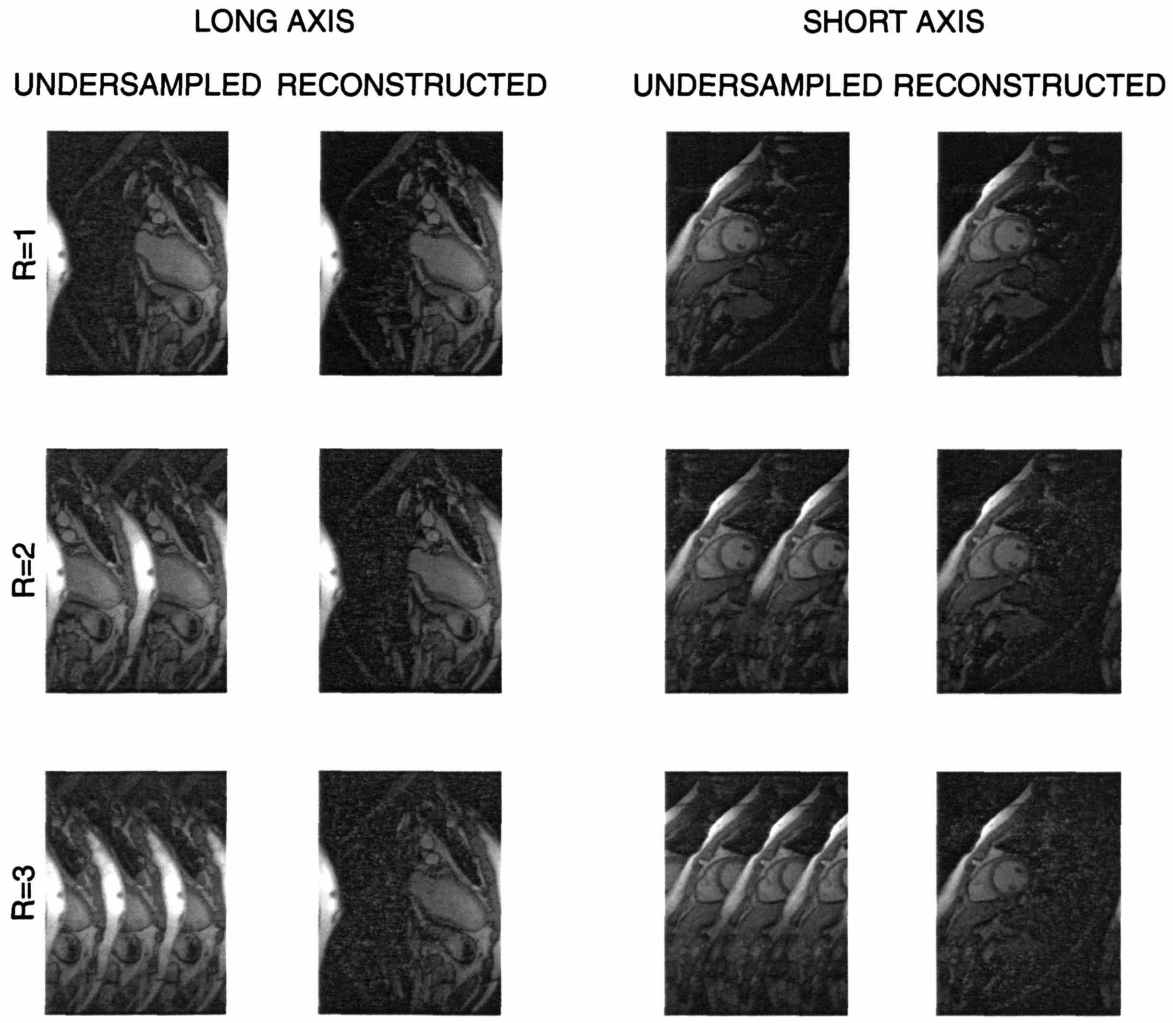

Figure 2.11 Undersampled and reconstructed long- and short-axis cardiac images for acceleration factors of 1, 2, and 3.

2.5 Discussion

We have presented a new type of coil array design that is intended to provide flexibility in the choice of image planes and undersampling directions for parallel magnetic resonance imaging. These arrays consist of elements placed concentrically on top of each other. While individual array elements with more lobes may have lower SNR than single loops, the SNR of the composite array is comparable to equivalent loop-based arrays.

The two 4-element linear array configurations considered in this work are both well-suited for parallel reconstructions of 2- and 3-fold undersampled data along their principal axes. However, each linear array performs very poorly when the image plane is rotated 90 degrees away from the main array axis.

The 4-element concentric array and the GRID4 array, by contrast, are able to reconstruct 2-fold undersampled data with a low g-factor at any angle. This reflects the fact that both types of arrays have coil sensitivities with variations in multiple directions. For acceleration factors of three, however, the grid array performs very poorly in both the 0- and 90-degree image planes. This degradation in performance occurs because the grid array has only two effective coils in those directions. The concentric array, by contrast, performs just as well as the FH4 linear array for an acceleration factor of 3 in the 0-degree image plane (which is along the principal axis of FH4). The concentric array performs worse in the 90-degree image plane, however, because one of the 2-lobed coils (coil B from Figure 2.8) has a sensitivity null in the 90-degree plane. Thus, only three out of four coils are available for the parallel reconstruction in that direction. It should be noted, however, that the effects of this sensitivity null are particularly dramatic for the experiment shown here because these experiments only examine performance through the center of the phantom, which is in the middle of the sensitivity null of the 2-lobed coil B. The array is expected to perform slightly better for reconstructing image lines parallel to but displaced from the central line. Still, although the concentric array performs more poorly for a 3-fold acceleration at 90 degrees than it performs at 0 degrees, the average g-factor of the concentric array is still lower than any of the candidate arrays besides the LR4 array (which has a principal axis of 90 degrees).

Our prototype concentric coil array has been built using rectangular lobes. This has allowed us to simulate its performance using the analytic formulation of the noise power for these coils presented in Appendix B. Other lobe shapes may be advantageous in some applications, and they should be considered in future designs.

In addition to offering flexibility in the choice of shape for the coil lobes, concentric arrays allow for a large amount of variation in terms of coil sizes and angular offsets. While much of this

chapter has been devoted to describing a particular prototype, several general conclusions about concentric arrays can be taken and applied to other designs. First, the decrease in the peak SNR seen with larger numbers of coil lobes (Figure 2.4) implies that it is best to build a concentric array with elements that have as few lobes as possible. The sharpness of the SNR peak for the single-loop coil implies that there is not much room for variation in coil size for that coil. The single-loop coil should almost always be simply optimized for the particular imaging depth. However, the sizes of the 2-lobed and 4-lobed coils can be varied over a larger range without losing SNR (the two 2-lobed coils also need not be the same size).

The maximum number of elements that can eventually be incorporated into a single concentric coil array remains to be determined. A second 4-lobed coil can certainly be incorporated into the design presented here. One of the most significant practical challenges to building concentric arrays with many elements will be the number of wires that need to cross in the center of each coil. The use of multi-layer circuit board techniques may solve this problem. Another practical difficulty is the length of conductor that will be required to bring the current into the center and then back out for each element. This added conductor has the potential to introduce more noise. This added noise is especially problematic considering that the sensitivity of higher-order concentric elements is mostly concentrated towards the coils' peripheries, and therefore the central conductors would contribute copper noise without making any appreciable contribution to the received signal. Alternative resonant structures such as grid-arrays (81) may be able to maintain the current symmetries required by Eqs. [2.3] and [2.6] while minimizing the amount of current that must flow through the center of the coil.

The multidimensional spatial encoding properties of concentric coil arrays are ideal for applications such as cardiac imaging, where several image planes are required and the absolute orientations of those image planes are usually not known beforehand. Coil arrays with sensitivity variations in several directions are also useful for accelerating three-dimensional image acquisitions. In these types of acquisitions, it has been shown that simultaneous undersampling and reconstruction in two phase-encode directions yields better SNR than an equivalent amount of acceleration in one direction alone (69). Concentric arrays should prove particularly useful

for accelerating acquisitions that have radial and spiral trajectories, which share the axial symmetry of the coil array.

While this work has focused on the ability of concentric arrays to flexibly accelerate image acquisitions in directions parallel to the coil plane, many applications still require acceleration in the anterior-posterior direction, which is perpendicular to the coil plane. While these applications have not been quantitatively explored here, concentric arrays can be expected to encounter difficulties that are similar to those faced by conventional loop designs when undersampling is perpendicular to the array plane. For these situations, it is probably advisable to have two sets of coils in the array – one set anterior to the patient, and one set posterior.

Concentric coil arrays are intended to complement conventional coil array designs by offering additional ways in which to arrange coil elements. When the number of receiver channels available in an MR system is unlimited, then a design such as the concentric array has fewer clear advantages when compared to a grid array; indeed, the principle of superposition for magnetic fields implies that a sufficiently dense grid of loop coils will eventually be able to duplicate the sensitivity pattern of any RF coil. The concentric design, however, offers a flexible set of coil sensitivities while employing a limited number of array elements. As the number of array elements increases, hybrid designs can be envisioned, where sets of concentric array elements are themselves arrayed in a grid-like fashion.

Using arrays with characteristics of both concentric arrays and grid arrays, it will be more difficult to maintain the symmetry conditions that allow for the electrical isolation of concentric array elements. In fact, as the number of elements included in coil arrays of all types continues to increase and the elements become packed more densely, eliminating the interactions between elements is expected to be a significant challenge. The next chapter examines these electrical interactions, especially inductive coupling, in a more detailed fashion and attempts to assess their effects on parallel MRI reconstructions.

2.6 Table 2.1 Concentric Array Reflection Coefficient Measurements

Coil transmission coefficient (S21) for concentric array loaded on a human chest (dB)

	2-lobed coil A	2-lobed coil B	4-lobed coil
square	-22.6	-25.6	-28.6
2-lobed coil A		-35.1	-19.0
2-lobed coil B			-10.4

2.7 Appendix A: Rotational symmetry conditions for vanishing mutual inductance of concentric arrays

The mutual inductance between an m-lobed concentric coil that produces a magnetic field $\mathbf{B}^m(\mathbf{r})$ and an n-lobed concentric coil with magnetic field $\mathbf{B}^n(\mathbf{r})$ is calculated by evaluating the overlap integral in Equation [2.1]. This integral can be written in cylindrical coordinates ($\mathbf{r} = (\rho, \theta, z)$) in terms of the scalar function $\varphi_{mn} \equiv \mathbf{B}^m(\mathbf{r}) \cdot \mathbf{B}^n(\mathbf{r})$:

$$\int \mathbf{B}^m \cdot \mathbf{B}^n d^3\mathbf{r} = \int_{-\infty}^{\infty} dz \int_0^{\infty} 2\pi\rho d\rho \int_0^{2\pi} \varphi(\rho, \theta, z) d\theta . \qquad [2.13]$$

If d is the greatest common denominator of m and n, and $a \equiv m/d$ and $b \equiv n/d$, then for a given value of ρ and z,

$$\begin{aligned}
\varphi(\theta + \frac{2\pi}{d}) &= \mathbf{B}^m(\theta + \frac{2\pi}{d}) \cdot \mathbf{B}^n(\theta + \frac{2\pi}{d}) \\
&= \mathbf{B}^m(\theta + a\frac{2\pi}{m}) \cdot \mathbf{B}^n(\theta + b\frac{2\pi}{n}) \\
&= (-1)^{a+b} \mathbf{R}\left(a\frac{2\pi}{n}\right)\mathbf{B}^m(\theta) \cdot \mathbf{R}\left(b\frac{2\pi}{m}\right)\mathbf{B}^n(\theta) . \qquad [2.14] \\
&= (-1)^{a+b} \mathbf{B}^m(\theta) \cdot \mathbf{B}^n(\theta) \\
&= (-1)^{a+b} \varphi(\theta)
\end{aligned}$$

In the third line above, we have used the fact that the dot product of two vectors does not change if they are both rotated by the same angles. Because concentric coils have an even number of lobes, d must be an even integer and the angular integration from Equation [2.13] is

$$\int_0^{2\pi} \varphi(\theta)d\theta = \frac{d}{2}\left[\int_0^{2\pi/d} \varphi(\theta)d\theta + \int_{2\pi/d}^{4\pi/d} \varphi(\theta)d\theta\right]$$
$$= \frac{d}{2}\int_0^{2\pi/d}\left(\varphi(\theta) + \varphi(\theta + \frac{2\pi}{d})\right)d\theta \ . \qquad [2.15]$$
$$= \left(1 + (-1)^{a+b}\right)\frac{d}{2}\int_0^{2\pi/d} \varphi(\theta)d\theta$$

If exactly one of the two integers a and b is odd, their sum will be an odd integer and the mutual inductance will be zero.

2.8 Appendix B: Sample-induced noise for coils with rectangular lobes

The calculation of the sample induced noise power for concentric coils with rectangular lobes is a modification of the technique presented in Reference (59) for computing the noise power of a single square coil. The thermal fluctuations induced in a coil by a conductive sample are random with zero mean and standard deviation equal to

$$\sqrt{4k_bT\Delta f R_s}\,, \qquad [2.16]$$

where k_b is Boltzman's constant, T is the absolute temperature, Δf is the bandwidth of the experiment, and R_s is the resistance to current flow in the coil presented by the sample. R_s is determined by calculating the power deposited in the sample per unit current I flowing in the coil. For a half-infinite sample filled with with uniform conductivity σ, the sample loading resistance is given by

$$R_s = \frac{\sigma}{I^2}\int\limits_{\substack{half\\volume}} |\mathbf{E}|^2\, d^3\mathbf{r}\,. \qquad [2.17]$$

When the electromagnetic wavelength corresponding to the field oscillations is large compared to the dimensions of the surface coil (quasi-static case), the electric field $\mathbf{E}$ can be written in terms of the vector potential $\mathbf{A}$

$$\mathbf{E} = -\frac{\partial \mathbf{A}}{\partial t} = -\frac{i\omega\mu_0}{4\pi}\int d^3\mathbf{r}'\frac{\mathbf{J}(\mathbf{r}')}{|\mathbf{r}-\mathbf{r}'|}\,. \qquad [2.18]$$

If the current loop is confined to the plane $z = 0$ and the cross-sectional area is small, then this can be written as an integral over the surface of the coil S. The order of the integrations in Eqs. [17] and [18] can be exchanged, leading to an expression for the noise power of a planar current distribution (Reference (59), Eq. 34):

$$R_s = \pi\sigma\left(\frac{\omega\mu_0 I}{4\pi}\right)^2 \int\frac{g(x,y)dxdy}{\sqrt{x^2+y^2}} \qquad [2.19]$$
$$g(x,y) = \int f(x_1,y_1)f(x_1-x,y_1-x)dx_1dy_1$$

In this expression, $f(x,y)$ is a function that describes the shape of the coil. The function is equal to 1 when it is evaluated at points inside the coil and it is equal to 0 at points outside of the coil. For a rectangular loop coil with dimensions r and s, the convolution integral from Equation [2.19] is

$$g(x,y) = \begin{cases} (r-|x|)(s-|y|) & |x|<\frac{r}{2}, |y|<\frac{s}{2} \\ 0 & otherwise \end{cases} . \qquad [2.20]$$

Equation [2.19] is then evaluated as

$$R_{rect}(r,s) = \pi\sigma\left(\frac{\omega\mu_0 I}{4\pi}\right)^2 4\int_0^{\frac{r}{2}}dx\int_0^{\frac{s}{2}}dy\frac{(r-x)(s-y)dxdy}{\sqrt{x^2+y^2}}$$
$$= \frac{\pi\sigma}{4}\left(\frac{\omega\mu_0 I}{4\pi}\right)^2\left[r^2 s\ln\left(\frac{r+\sqrt{r^2+s^2}}{s}\right)+rs^2\ln\left(\frac{s+\sqrt{r^2+s^2}}{r}\right)-\frac{1}{3}(r^2+s^2)^{3/2}+\frac{1}{3}(r^3+s^3)\right] \qquad [2.21]$$

The noise powers of the two- and four-lobed concentric coils can be derived by superposition. The current pattern in a two-lobed coil can be written as the sum of the currents in two adjacent rectangular coils with opposing current directions. If the electric fields produced by a unit (positive) current in these smaller lobes are $\mathbf{E}_1$ and $\mathbf{E}_2$, the total noise power from the two-lobed coil can be written

$$
\begin{aligned}
R_{\substack{two\\lobes}}(r,s) &= \frac{\sigma}{I^2}\int\limits_{\substack{half\\volume}} \left|\mathbf{E}_1-\mathbf{E}_2\right|^2 d^3\mathbf{r} \\
&= \frac{\sigma}{I^2}\int\limits_{\substack{half\\volume}} \left[\left|\mathbf{E}_1\right|^2+\left|\mathbf{E}_2\right|^2-(\mathbf{E}_1\cdot\mathbf{E}_2^*+\mathbf{E}_1^*\cdot\mathbf{E}_2)\right] d^3\mathbf{r} \\
&= \frac{\sigma}{I^2}\int\limits_{\substack{half\\volume}} \left[\left|\mathbf{E}_1\right|^2+\left|\mathbf{E}_2\right|^2-(\left|\mathbf{E}_1+\mathbf{E}_2\right|^2-\left|\mathbf{E}_1\right|^2+\left|\mathbf{E}_2\right|^2)\right] d^3\mathbf{r} \\
&= 4R_{rect}\left(\frac{r}{2},s\right)-R_{rect}(r,s)
\end{aligned}
\qquad [2.22]
$$

The current in a four-lobed coil can be viewed as the sum of the currents in two two-lobed coils. The total noise power in a four-lobed coil is

$$
\begin{aligned}
R_{\substack{four\\lobes}}(r) &= 4R_{\substack{two\\lobes}}\left(r,\frac{r}{2}\right)-R_{\substack{two\\lobes}}(r,r) \\
&= 16R_{rect}\left(\frac{r}{2},\frac{r}{2}\right)-4R_{rect}\left(r,\frac{r}{2}\right)-4R_{rect}\left(\frac{r}{2},r\right)+R_{rect}(r,r). \\
&= 24R_{rect}\left(\frac{r}{2},\frac{r}{2}\right)-8R_{rect}\left(r,\frac{r}{2}\right)
\end{aligned}
\qquad [2.23]
$$

In the third line, we have used the fact that (from Equation [2.21]) $R_{rect}(\alpha r,\alpha r)=\alpha^3 R_{rect}(r,r)$.

Although there is no analytical form for the noise resistance of concentric coils with more than four lobes (or for coils with arbitrarily-shaped lobes), these coils can be evaluated by numerically integrating the expressions in Equation [2.19].

Chapter 3.
The Effects of Coil Coupling on Parallel MR Image Reconstructions[3.1]

3.1 Introduction

For a long time, the elimination of inductive coupling has been considered an important part of designing radiofrequency (RF) coil arrays for MRI (1). When coils couple inductively, they resonate as a single structure, and it can be very difficult to match the impedance of each element simultaneously to the input impedance of the receiver circuitry. When this match is non-optimal, the preamplifier noise figure can be seriously degraded, leading to an image with a poor signal-to-noise ratio (SNR).

The development of parallel MRI techniques has led to renewed emphasis on removing coupling and maintaining coil isolation. Parallel MRI techniques require a coil array's component-coil sensitivity profiles to be as distinct as possible in order to encode spatial information. When coils couple inductively, they become sensitive to the same regions of the sample. It has thus been

[3.1] The work in this chapter has been published as: "Ohliger MA, Ledden P, McKenzie CM, Sodickson DK. The Effects of Coupling on Parallel MR Image Reconstructions. Magnetic Resonance in Medicine 2004: 52(3):628-639"

feared that coupled coils might contain less distinct spatial information than uncoupled coils, yielding lower quality parallel MRI reconstructions (34,38,63).

When coil arrays are used for spatial encoding in parallel MRI, many of the traditional methods of decoupling coil array elements become more difficult. Overlapping RF coils to eliminate shared magnetic flux (1) leads to stringent constraints on how the elements are placed. This fixed overlap may not always be appropriate for parallel imaging (34,63). Preamplifiers with extremely low input impedances (1,34,67) and lumped-element decoupling networks (64,65) have become the primary techniques for decoupling arbitrarily-placed coil array elements. Still, extending these techniques to large numbers of coils with varying amounts of shared inductance is complex and challenging. Thus, it has become important to quantitatively assess the impact of inductive coupling on parallel image reconstructions, in order to determine how crucial a role decoupling strategies should play in the design of future arrays.

This chapter describes a theoretical and experimental analysis of the impact of inductive coupling on the ability of coil arrays to encode spatial information in parallel image reconstructions. Moderate levels of coupling are explored, representative of residual couplings that might be encountered in practical arrays. These coupling levels are generally not sufficient to affect the preamplifier noise figure, but they do cause array elements to share signal and make their sensitivities less distinct. We show that while the effects of preamplifier noise continue to be important, the intrinsic spatial encoding properties of a coil array remain largely intact in the presence of inductive coupling.

3.2 Theory

3.2.a Circuit Model

The coupling observed in an MR acquisition using a coil array can be described by a simple electronic circuit model. Circuit models have been presented elsewhere to describe the effects of mutual inductance (1,34,65,66,82), and the one we present here repeats some parts of those presentations. Our description is intended to clarify our experimental design, and to emphasize the areas that are crucial to understanding the particular impact of inductive coupling on parallel

MRI. In later sections, we show how the resulting expressions for coupling can be formally integrated into the equations for the parallel MRI reconstruction.

A model for the n_c-coil system used in this work is shown schematically in Figure 3.1. Precessing magnetization, along with noise sources, induces a net voltage with amplitude V_l around each coil. The magnitude of each voltage depends on that coil's spatial sensitivity to precessing magnetization and noise. The sensitivity to both signal and noise can be derived using the principle of reciprocity (1,80,83). In the Appendix, it is shown that the vector of signals **S** received by the coils within the array is related to the induced voltages through the expression:

$$\mathbf{S} \propto \Lambda[\mathbf{Z}^{coil} + \mathbf{Z}^{input}]^{-1}\mathbf{V}, \qquad [3.1]$$

where $\mathbf{Z}^{coil}$ and $\mathbf{Z}^{input}$ are n_c by n_c matrices that describe the impedances of the individual coils within the array and the preamplifiers and matching networks at the coil inputs, respectively. Λ is a diagonal matrix that gives an overall scaling that is defined in the appendix.

The MR signal in any channel is thus, in general, a linear combination of the voltages induced in all of the coils. Two special cases lead to decoupled arrays. As mentioned in the appendix, when the mutual inductances (and resistances) between the coils are zero, then the sum $\mathbf{Z}^{coil} + \mathbf{Z}^{input}$ is diagonal and the MR signal recorded by any receiver is directly proportional to only the voltage induced in the coil connected to that receiver. Alternatively, if the preamplifier input impedances are small, the coil matching circuitry will transform them into large impedances (Eq. [3.20]). The entries of $\mathbf{Z}^{input}$ will be large compared with those of $\mathbf{Z}^{coil}$, and the transformation described by Equation [3.1] will be nearly diagonal, even in the presence of significant mutual inductance.

In order to derive the coupling observed in MR data, consider two array configurations, labeled A and B. In configuration A, the coils have been adequately isolated. In configuration B, the array has been modified, for example by changing the preamplifier input impedances. The vector of induced voltages **V** is completely specified by Faraday's law of magnetic induction. As long as the positions of the coils and the sample are not changed, $\mathbf{V}_A = \mathbf{V}_B \equiv \mathbf{V}$. This relationship,

together with Equation [3.1], yields an expression for the total amount of coupling $\mathbf{M_{AB}}$ seen in the observed MR signal:

$$\begin{aligned}\mathbf{S_B} &= \mathbf{\Lambda_B}[\mathbf{Z_B^{coil}} + \mathbf{Z_B^{input}}]^{-1}\mathbf{V_B} \\ &= \mathbf{\Lambda_B}[\mathbf{Z_B^{coil}} + \mathbf{Z_B^{input}}]^{-1}\mathbf{V_A} \\ &= \mathbf{\Lambda_B}[\mathbf{Z_B^{coil}} + \mathbf{Z_B^{input}}]^{-1}[\mathbf{Z_A^{coil}} + \mathbf{Z_A^{input}}]\mathbf{\Lambda_A^{-1}}\mathbf{S_A} \\ &\equiv \mathbf{M_{AB}}\mathbf{S_A}\end{aligned} \quad . \qquad [3.2]$$

The most important consequence of Equation [3.2] – that the coupled signal $\mathbf{S_B}$ is linearly related to the uncoupled signal $\mathbf{S_A}$ – will be generally true for almost any type of coil array. However, the quantitative evaluation of $\mathbf{M_{AB}}$ (by way of Equation [3.2] and the appendix) for the specific array used in this work will be important when we discuss our experimental design.

In this discussion, the terms "mutual inductance" and "inductive coupling" refer to distinct quantities. "Mutual inductance" specifically refers to L_{ij}, which (in the form $i\omega L_{ij}$) constitutes the inductive component of the shared impedance between two RF coils. "Inductive coupling," on the other hand, refers to the entries of the coupling matrix $\mathbf{M_{AB}}$ in Equation [3.2], and describes the net effect of the shared impedance on the component coil images that are received and reconstructed by the MR scanner. (We identify this coupling familiarly as inductive even though strictly speaking it contains the effects of shared impedance more generally.) The inductive coupling depends on the mutual inductance as well as the impedances of all of the components of the coil array, particularly the preamplifiers. The next section describes how the coupling matrix $\mathbf{M_{AB}}$ affects the parallel MRI reconstruction.

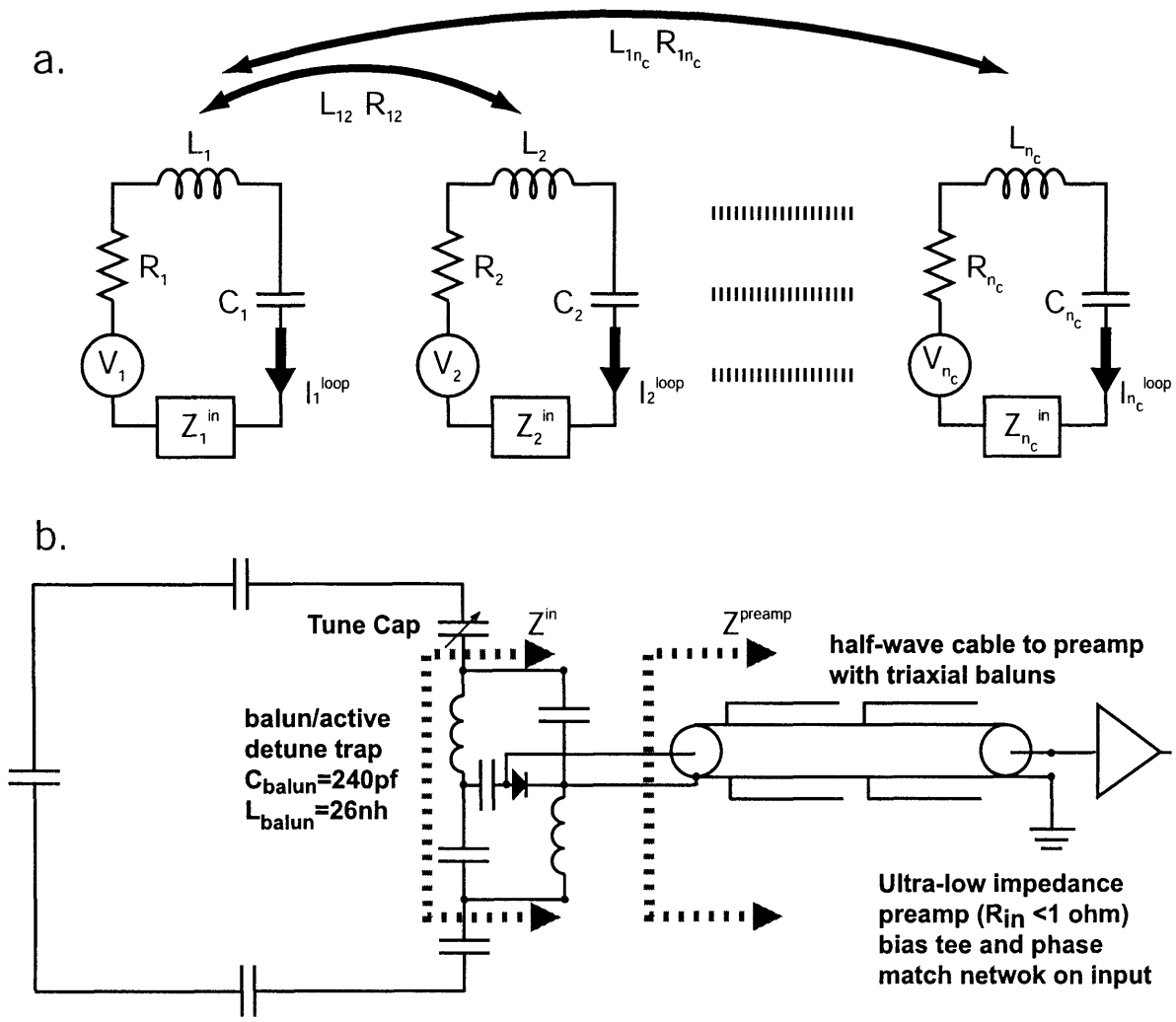

Figure 3.1 (a) Circuit model for coupling analysis. The preamplifier input impedances and matching networks are represented as lumped elements. (b) Detailed circuit model for the coil array elements. The dashed arrows bracket the circuit elements that are collectively represented by the lumped-element impedances, Z_l^{in} and Z_l^{preamp}, that are used in (a) and in the text. [diagram and measurements for (b) by P. Ledden, Nova Medical, inc. Wakefield MA]in

3.2.b Effects of Coupling on Parallel Imaging Reconstructions

For the purposes of image reconstruction, the expression for the total MR signal received by the *l*th component coil in an array at k-space point $\mathbf{k}_m$ due to a distribution of transverse magnetization $\rho(\mathbf{r})$ is discretized and written in the form:

$$S_l(\mathbf{k}_m) \approx \left(\sum_{\text{pixels j}} e^{i\mathbf{k}_m \bullet \mathbf{r}_j} C_l(\mathbf{r}_j) \rho(\mathbf{r}_j) \right) + n_l(\mathbf{k}_m). \qquad [3.3]$$

$C_l(\mathbf{r}_j)$ is the sensitivity function for coil l at spatial position $\mathbf{r}_j$, and n_l is a Gaussian random variable representing white noise, which varies with time and incidentally with k-space position $\mathbf{k}_m$. In generalized parallel imaging approaches (11,16), the sensitivity variations and the gradient modulations for all of the coils are formally combined into a single encoding matrix **B,** defined by

$$B_{(lm),j} \equiv e^{i\mathbf{k}_m \bullet \mathbf{r}_j} C_l(\mathbf{r}_j), \qquad [3.4]$$

and Equation [3.3] is written in matrix form:

$$\mathbf{S} = \mathbf{B}\boldsymbol{\rho} + \mathbf{n}. \qquad [3.5]$$

The entries of the encoding matrix, **B,** are typically derived from one of several types of calibration scans that are described in detail elsewhere (7,11,15-17,51,52). The noise has statistical properties that are defined by the noise correlation matrix,

$$\hat{\boldsymbol{\Psi}} = \left\langle \mathbf{n}\mathbf{n}^{\dagger} \right\rangle_{time}. \qquad [3.6]$$

Here, the angular brackets denote a temporal average over noise samples. In the absence of inductive coupling, the off-diagonal elements of $\hat{\boldsymbol{\Psi}}$ correspond to *intrinsic* noise correlations, which arise due to the coherent reception of common noise sources. Because the noise that accompanies each separately-acquired k-space point is statistically independent, the noise correlation matrix is block diagonal, with the form $\hat{\boldsymbol{\Psi}} = \boldsymbol{\Psi} \otimes \mathbf{I}_k$ (where $\otimes$ is the tensor product

and $\mathbf{I_k}$ is an identity matrix with dimension equal to the number of acquired k-space points). The magnetization density $\boldsymbol{\rho}$ is reconstructed from the acquired signal $\mathbf{S}$ by finding a matrix $\mathbf{B}^{inverse}$ that inverts equation [3.5]. It has been shown that the maximum SNR is obtained by choosing a modified form of the Moore-Penrose Pseudoinverse (11,16)

$$\mathbf{B}^{inverse} = \left(\mathbf{B}^{\dagger}\hat{\boldsymbol{\Psi}}^{-1}\mathbf{B}\right)^{-1}\mathbf{B}^{\dagger}\hat{\boldsymbol{\Psi}}^{-1}. \qquad [3.7]$$

Under the influence of inductive coupling, the signals received by the various array elements can be written as linear combinations of the signals that would have been received by those elements had the detectors been uncoupled. The coil sensitivity functions are similarly transformed in the presence of inductive coupling, with the particular transformation given by the electrical coupling matrix $\mathbf{M_{AB}}$ (Equation [3.2]). Because coupling occurs independently for each of the n_k acquired k-space lines, the measured encoding matrix $\mathbf{B}$ transforms into a coupled matrix $\tilde{\mathbf{B}}$ according to the block diagonal matrix $\hat{\mathbf{M}} \equiv \mathbf{M_{AB}} \otimes \mathbf{I_k}$:

$$\tilde{\mathbf{B}} = \hat{\mathbf{M}}\mathbf{B}. \qquad [3.8]$$

In all expressions, the presence of a tilde denotes a quantity measured using an array that is under the influence of inductive coupling.

Just as coupled coils share voltages that are induced by precessing magnetization, they can be expected to share noise voltages as well. Because of this, noise received by coupled coil array elements is expected to exhibit a higher degree of correlation than it would be in an array with decoupled coil elements. In order to obtain a general idea of how noise correlations change under the influence of coupling, we adopt a simple noise model in which random fluctuations within the MR sample induce a time-varying random voltage around each coil. As mentioned above, and as formalized in Equation [3.6], these noise voltages are intrinsically correlated, even before taking inductive coupling into consideration. Because they are voltage sources, the noise voltages transform according to the same coupling matrix, $\hat{\mathbf{M}}$, as the coil sensitivities, and so we write

$$\tilde{\mathbf{n}} = \hat{\mathbf{M}}\mathbf{n}. \qquad [3.9]$$

The new noise correlation matrix $\tilde{\hat{\mathbf{\Psi}}}$ depends on both the coupling matrix $\hat{\mathbf{M}}$ and the intrinsic noise correlation matrix, $\hat{\mathbf{\Psi}}$:

$$\tilde{\hat{\mathbf{\Psi}}} = \left\langle \tilde{\mathbf{n}}\tilde{\mathbf{n}}^{\dagger} \right\rangle_{time} = \hat{\mathbf{M}} \left\langle \mathbf{n}\mathbf{n}^{\dagger} \right\rangle_{time} \hat{\mathbf{M}}^{\dagger} = \hat{\mathbf{M}}\hat{\mathbf{\Psi}}\hat{\mathbf{M}}^{\dagger}. \qquad [3.10]$$

It is important to make a distinction between intrinsic noise correlations and those introduced by coupling because – as we shall see – the intrinsic correlations described by Equation [3.6] are determined solely by the interaction of the coil array with the sample and thus they cannot be changed, while the additional correlations brought about through inductive coupling can be compensated for in the reconstruction.

If the coupling matrix, **M**, is non-singular, the inverse procedure in Equation [3.7] can be applied to the coupled data described by Equations [3.8] and [3.10],

$$\begin{aligned} \boldsymbol{\rho} &= \left(\tilde{\mathbf{B}}^{\dagger} \tilde{\hat{\mathbf{\Psi}}}^{-1} \tilde{\mathbf{B}} \right)^{-1} \tilde{\mathbf{B}}^{\dagger} \tilde{\hat{\mathbf{\Psi}}}^{-1} \tilde{\mathbf{S}} \\ &= \left(\mathbf{B}^{\dagger} \hat{\mathbf{M}}^{\dagger} \hat{\mathbf{M}}^{\dagger^{-1}} \hat{\mathbf{\Psi}}^{-1} \hat{\mathbf{M}}^{-1} \hat{\mathbf{M}} \mathbf{B} \right)^{-1} \mathbf{B}^{\dagger} \hat{\mathbf{M}}^{\dagger} \hat{\mathbf{M}}^{\dagger^{-1}} \hat{\mathbf{\Psi}}^{-1} \hat{\mathbf{M}}^{-1} \hat{\mathbf{M}} \mathbf{S}. \\ &= \left(\mathbf{B}^{\dagger} \hat{\mathbf{\Psi}}^{-1} \mathbf{B} \right)^{-1} \mathbf{B}^{\dagger} \hat{\mathbf{\Psi}}^{-1} \mathbf{S} \end{aligned} \qquad [3.11]$$

Equation [3.11] implies that the theoretically optimal image reconstruction in the presence of inductive coupling is identical to the optimal reconstruction of the same data in the absence of coupling. The disappearance of the coupling matrix from Equation [3.11] relies on the fact that the noise correlation statistics contain enough information about the degree of coupling to compensate for the effects of coupling on the coil sensitivities. The ability to make this compensation is a direct consequence of Equation [3.9], which asserts that the noise in the various channels will be coupled in the same ratios as the signals. This assertion does not explicitly depend on the nature or the strength of the coupling, but it does rely on two other basic assumptions. First, it is assumed that the simple circuit model described above, in which sample noise is represented as a set of correlated voltage sources, is sufficient to describe the noise in

our array. The second assumption is that the sample remains the dominant source of noise in both the coupled and the uncoupled coil array. The next section addresses the effects of having additional noise sources that disturb the noise statistics enough to make the compensation in Equation [3.11] impossible.

3.2.c Noise Effects of Preamplifiers

The transformation of noise described by Equation [3.9] explicitly assumes that noise originating from the sample is the dominant source of noise in the measured data, even under the influence of inductive coupling. The preamplifiers that connect the detectors to the RF receiver chain have the potential to profoundly affect the final noise properties of the coil array. Preamplifiers are designed to have minimum noise figures when presented with optimal impedance values at their inputs (typically 50 ohms). In the presence of significant inductive coupling, it may be difficult to maintain this optimal impedance match. As a consequence, additional noise will be generated in the process of amplifying the signal. It has also been suggested that noise sources arising from the preamplifier input circuitry (e.g. preamplifier input resistance) may be transferred among the coils if the isolation is not perfect (84), although the quantitative importance of this effect is unclear (85,86).

Formally, the preamplifier noise sources can be combined into a single variable, $\mathbf{n}_p$, that adds in an uncorrelated fashion to the sample noise, $\mathbf{n}_s$:

$$\mathbf{S} = \mathbf{B}\boldsymbol{\rho} + \mathbf{n}_s + \mathbf{n}_p . \qquad [3.12]$$

The preamplifier noise $\mathbf{n}_p$ is described by its own noise correlation matrix, $\hat{\mathbf{K}}$. For clarity of notation, we consider the case where the preamplifier noise is only significant in the coupled case. The coupled noise correlation matrix becomes

$$\tilde{\hat{\boldsymbol{\Psi}}} = \left\langle \tilde{\mathbf{n}}\tilde{\mathbf{n}}^{\dagger} \right\rangle_{time} = \hat{\mathbf{M}} \left\langle \mathbf{n}_s \mathbf{n}_s^{\dagger} \right\rangle_{time} \hat{\mathbf{M}}^{\dagger} + \left\langle \mathbf{n}_p \mathbf{n}_p^{\dagger} \right\rangle_{time} = \hat{\mathbf{M}}\hat{\boldsymbol{\Psi}}\hat{\mathbf{M}}^{\dagger} + \hat{\mathbf{K}} , \qquad [3.13]$$

and the reconstruction in Equation [3.11] becomes

$$\begin{aligned}\boldsymbol{\rho} &= \left[\mathbf{B}^{\dagger}\hat{\mathbf{M}}^{\dagger}\left[\hat{\mathbf{M}}\hat{\boldsymbol{\Psi}}\hat{\mathbf{M}}^{\dagger}+\hat{\mathbf{K}}\right]^{-1}\hat{\mathbf{M}}\mathbf{B}\right]^{-1}\mathbf{B}^{\dagger}\hat{\mathbf{M}}^{\dagger}\left[\hat{\mathbf{M}}\hat{\boldsymbol{\Psi}}\hat{\mathbf{M}}^{\dagger}+\hat{\mathbf{K}}\right]^{-1}\hat{\mathbf{M}}\mathbf{S} \\ &= \left[\mathbf{B}^{\dagger}\left[\hat{\boldsymbol{\Psi}}+\hat{\mathbf{M}}^{-1}\hat{\mathbf{K}}\hat{\mathbf{M}}^{\dagger-1}\right]^{-1}\mathbf{B}\right]^{-1}\mathbf{B}^{\dagger}\left[\hat{\boldsymbol{\Psi}}+\hat{\mathbf{M}}^{-1}\hat{\mathbf{K}}\hat{\mathbf{M}}^{\dagger-1}\right]^{-1}\mathbf{S}\end{aligned} \quad . \qquad [3.14]$$

Thus, in the presence of preamplifier noise effects, the parallel MRI reconstruction can still be formally recast in terms of the uncoupled acquired signal vector and encoding matrix. However, the reconstruction of coupled data is no longer equivalent to the uncoupled case. The alterations to the reconstruction can be expressed in terms of an altered noise correlation matrix $\hat{\boldsymbol{\Psi}}_{effective} = \hat{\boldsymbol{\Psi}} + \hat{\mathbf{M}}^{-1}\hat{\mathbf{K}}\hat{\mathbf{M}}^{\dagger-1}$. Because $\hat{\mathbf{K}}$, $\hat{\mathbf{M}}$, and $\hat{\boldsymbol{\Psi}}$ are not independent parameters, it is difficult to predict whether the perturbation they make in the noise statistics will cause an increase or a decrease in the net SNR. The experiments described in the next section are intended as a preliminary evaluation of these effects.

3.3 Methods

3.3.a Experimental Design

Figure 3.2a illustrates schematically the system used to evaluate the effects of coupling. A two-coil system is shown in two configurations. In configuration A, the two identical coils are connected to low input impedance preamplifiers. The cable lengths that connect the preamplifiers to the coils are chosen so that the minimum possible impedance Z^{preamp} is present at the input of each coil matching network. It is convenient to represent the electrical effects of the cables that connect the preamplifiers to the coils in terms of the preamplifiers' reflection coefficients. If preamplifier 1 has reflection coefficient with magnitude Γ_1^0, then the minimum possible impedance is $Z_1^{preamp} = 50(1-\Gamma_1^0)/(1+\Gamma_1^0)$. After being transformed by the matching network, the impedance at the input of that coil becomes (from Equation [3.20]) $Z_1^{in} = R_1(1+\Gamma_1^0)/(1-\Gamma_1^0)$. If Γ_1^0 is close to 1, then Z_1^{in} can become very large and only a small amount of current is allowed to flow in coil 1. Little signal is transferred from one coil to the other, even in the presence of a large mutual inductance.

When the system is modified (configuration B) by inserting a segment of cable that introduces an electrical phase delay α (measured at the Larmor frequency) between coil 1 and its preamplifier, the impedance of the preamplifier seen by the coil becomes

$$Z_1^{in} = \frac{50R_1}{Z_1^{preamp}} = R_1\left(\frac{1+\Gamma_1^0 e^{-i2\alpha}}{1-\Gamma_1^0 e^{-i2\alpha}}\right). \qquad [3.15]$$

The factor of two in the exponential occurs because the phase of the reflection coefficient is twice the phase delay α. As α increases, the impedance at the input of coil 1 decreases, allowing more current to flow in response to a given induced voltage. Thus, more signal is transferred from coil 1 to coil 2 as a result of the mutual inductance between them. The input impedance of coil 2 (the unmodified coil) remains large, and there is no signal transferred from coil 2 to coil 1.

a.

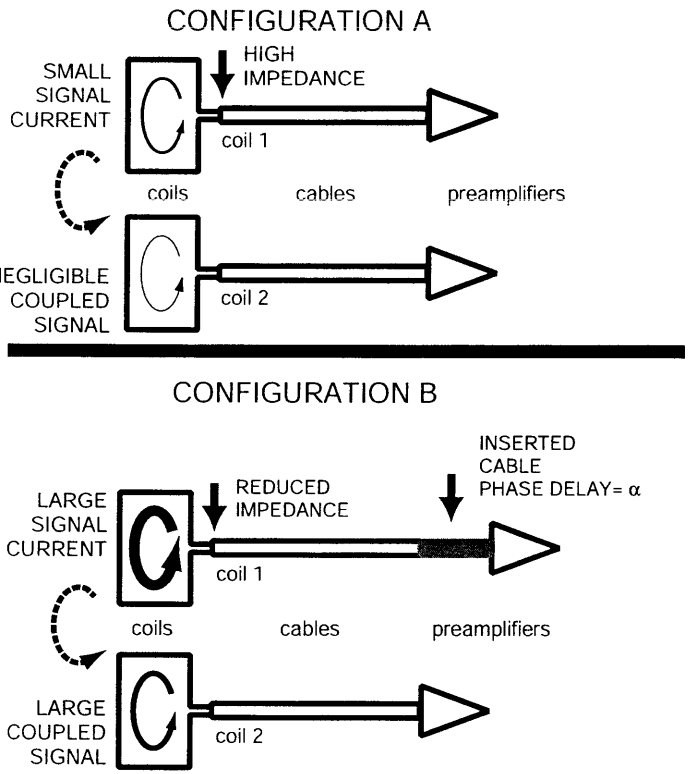

Figure 3.2 (a) Illustration of the experimental apparatus used to introduce a controlled amount of coupling. The apparatus is shown in two configurations: the base configuration, A, and a coupled configuration, B. In configuration B, an extra segment of BNC cable between coil 1 and its preamplifier introduces a phase delay α, which allows more current to flow in coil 1, which in turn couples more strongly to coil 2. The input impedance of coil 2, by contrast, is unaffected, and little of coil 2's signal is transferred to coil 1.

b.

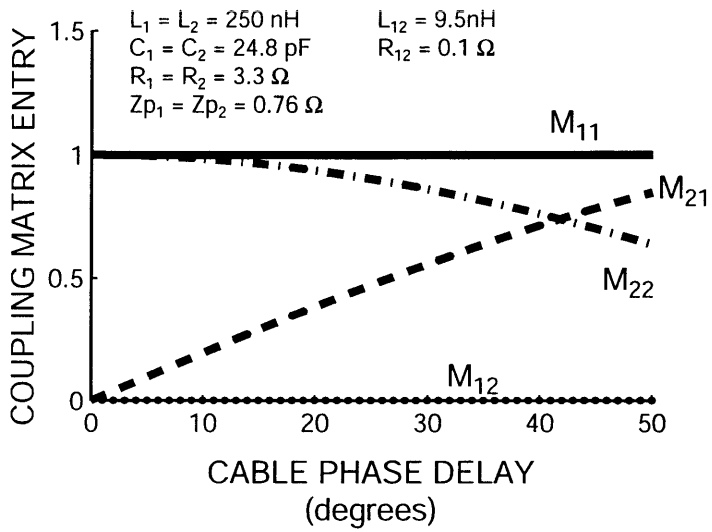

Figure 3.2 (b) Plot of the predicted signal coupling measured as a function of the induced cable phase delay α. The electrical parameters used are shown. Note that while there is considerable predicted coupling from coil 1 to coil 2 (M_{21}), there is no predicted coupling from coil 2 to coil 1 (M_{12}).

The elements of the coupling matrix $\mathbf{M_{AB}}$, calculated according to Equation [3.2], are shown as a function of α in Figure 3.2b for two coupled coils with typical coil parameters described in the figure. This example illustrates that the phase adjustments achieved through the modification of coil-preamplifier cable lengths provides a convenient way of adjusting the coupling of a multicoil system without changing the positions of any of the individual elements.

3.3.b Imaging apparatus[3.2]

For the experiments described here, a coil array with eight independently-positionable elements (*Model NMSC-010B-1.5TGE, Nova Medical, Inc., Wakefield, MA*) was positioned surrounding a 14.8 x 15 x 37.2 cm phantom as shown in Figure 3.3. The phantom was placed at the isocenter of a 1.5 T General Electric TwinSpeed Scanner equipped with eight receiver channels (*GE Medical Systems, Waukesha Wisconsin*).

A schematic diagram of an individual coil element is shown in Figure 3.1b. Each coil element was formed by an 8 x 18 cm rectangular copper trace on a flexible polyimide PC board and had an inductance of 250 nH. Each coil was tuned to 63.8 MHz with multiple distributed capacitors. The unloaded coil Q was greater than 400 and the loaded coil Q was approximately 30, giving an unloaded to loaded ratio of greater than 12:1. A lumped element bridge balun was used for matching each coil element to 50 ohms and a PIN diode across this balun detuned the coil during body coil transmit. Additional passive detuning traps provided isolation from the body coil transmitter in case of failure or disconnection of the active PIN diode bias. The output of the bridge balun was connected to an ultra-low impedance preamplifier (NMP-001, Nova Medical, Wakefield MA USA) through a half-wave cable with two triaxial baluns. A phase matching circuit on the input of the preamplifer was used to precisely adjust the reactive portion of the preamplifier input impedance in order to maximize the preamplifier isolation of the receive coil. Preamplifer isolation of each coil element was greater than 35 dB and no additional inductive or capacitive isolation was used between the elements of the coil array.

[3.2] Electronic measurements of coil array and preamplifiers made by P. Ledden, Nova Medical, Wakefield Massachusetts.

In the baseline state, each coil was directly connected to its corresponding low impedance preamplifer. The exact input impedance of each preamplifier along with its input reflection coefficient is listed in Table 3.1. In order to progressively introduce more coupling, four different sets of BNC extension cables were inserted between the preamplifiers and the coils. Using a vector network analyzer (Agilent Technologies model 8712ES), the phase delay for each inserted cable was evaluated by measuring the phase of its transmission coefficient S_{21} at 63.86 MHz. The complete set of phase delays for each coupling configuration (cpl1, cpl2, cpl3, and cpl4) are listed in Table 3.1.

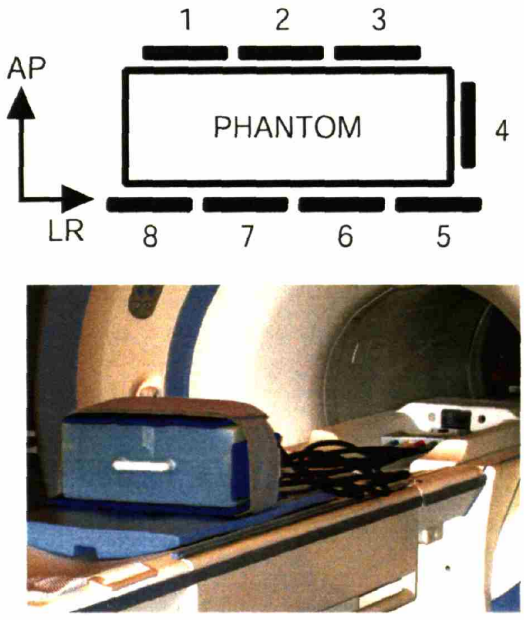

Figure 3.3 Schematic diagram and photograph illustrating the arrangement of the eight-coil array.

3.3.c Image Acquisition

For each level of coupling, 128 identical gradient echo images were acquired (TE 3.3 ms, TR 6.7 ms, flip angle 2°, BW 15.63 kHz, slice thickness 5 mm, matrix size 128 x 96). These images were each acquired in an axial plane through the center of the phantom. The fields of view in the left-right (LR) and the anterior-posterior (AP) directions were 42 cm and 31.5 cm, respectively. The readout was in the LR direction. Sensitivity calibration data were acquired using the same pulse sequence that was used to acquire the image data, but with 128 averages in order to increase SNR. No body-coil data were acquired.

The central 2/3 of the AP FOV – the minimum necessary to completely contain the phantom – was extracted from each image and used in the parallel imaging reconstructions (see Figure 3.4). The first and last image points in the readout direction (which contained no signal) were excluded to make the data compatible with both 2-fold and 3-fold undersampling. This yielded a net data matrix size of 126 x 60, with a 41.34 x 19.69 cm FOV. The 36 remaining signal-free AP lines in each of the 128 acquired images were used to generate a noise record. In order to avoid the effects of the scanner's frequency-domain filter, we included the central 119 points from each 128-point readout line, giving a final noise record with 36x119x128 = 548,352 samples. The covariance of this noise record was used to determine the correlation matrix Ψ in accordance with Equation [3.6]. Note that while Equation [3.6] is specified for noise in k-space, the orthogonality of the discrete Fourier transform guarantees that the image domain noise statistics will be the same up to an overall constant. Noise is simpler to measure in the image domain because it is easier to identify a signal-free region in the image domain than it is in k-space.

Undersampled data sets were generated from the fully-sampled images by extracting those lines of the raw k-space data that would correspond to an undersampled acquisition. The four levels of undersampling that were used are shown in Table 3.2. As described in the experiments from Chapter 2, each undersampled image was reconstructed using a Cartesian SENSE reconstruction, summarized by Equation [3.7]. Once again, no extra sensitivity processing or numerical conditioning such as that used in (11) or (16) was employed.

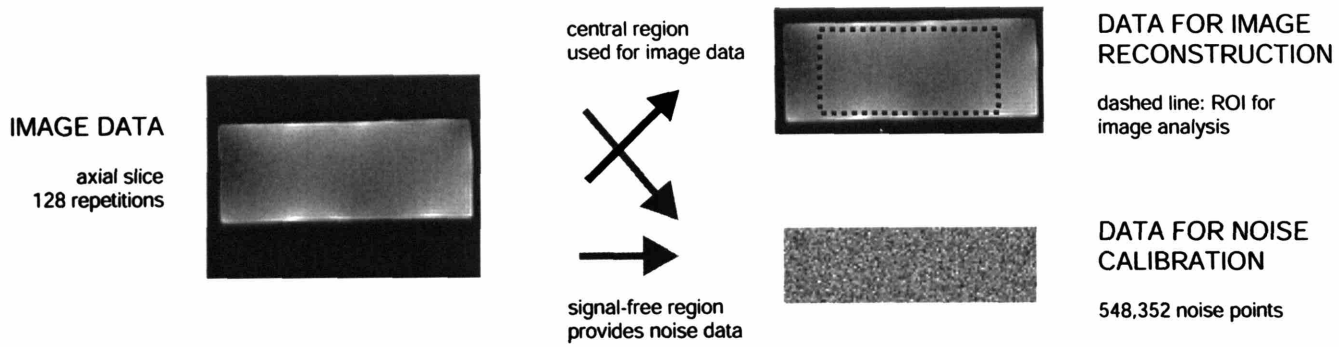

Figure 3.4 (a) Summary of the procedure used for data acquisition; 128 identical axial images were acquired. The outer one-third of each image (which contained no signal) was used to generate a noise record for calculation of the noise correlation matrix. The dotted line shows the location of the ROI used for all SNR measurements.

3.3.d Coupling Measurements

The image coupling matrices were calculated using the coil sensitivity reference images by finding a linear least-squares fit (via a matrix pseudoniverse) between the coupled and uncoupled component coil sensitivities. The overall amount of coupling for each coupling configuration was evaluated by determining the amount of coupled power in each coil channel, using the expression

$$\kappa_l = \frac{\sqrt{\sum_{l' \neq l} |M_{ll'}|^2}}{\sqrt{\sum_{l'} |M_{ll'}|^2}}, \qquad [3.16]$$

Note that the "AB" designation, which was used for the coupling matrix **M** in the Theory section, has been omitted for clarity.

3.3.e SNR Measurements

SNR was quantified by performing parallel imaging reconstructions on all 128 identical acquisitions. The pixel-by-pixel mean taken over all acquisitions was used as an estimate of the signal and the pixel-by-pixel standard deviation was used as a measure of the noise. Thus, a pixel-by-pixel SNR map was created. The mean percentage change in SNR in selected regions of interest (ROIs) for various coupling levels was determined by first computing the percentage SNR changes on a pixel-by-pixel basis and then computing the average value of these changes in a given ROI. We also computed the geometry factor, or "g-factor," which is defined for pixel j as (87)

$$g_j = \frac{SNR_{full}(j)}{\sqrt{R} \cdot SNR_R(j)}, \qquad [3.17]$$

where R is the acceleration factor or amount of undersampling; $SNR_{full}(j)$ and $SNR_R(j)$ refer to the SNR of the fully gradient-encoded image and the R-fold accelerated parallel MR image, respectively. The g-factor is always greater than 1, and reflects SNR losses due to the non-unitary transformations involved in the parallel imaging reconstruction. The g-factor values

reported in this chapter were computed on a pixel-by-pixel basis and then averaged over an appropriate ROI. All results in this chapter used the ROI shown with a dashed rectangle in Figure 3.4.

3.4 Results

3.4.a Component Coil Images

Component coil images for the array used in this study are shown in Figure 3.5. The first row of images was acquired when the coil array was in its baseline, or "base," configuration, and no coupling had been introduced. Below the baseline images are the component coil images that were acquired once the coil-preamplifier cable lengths had been adjusted in order to introduce coupling (see Table 3.1). The four successive levels of coupling shown in Figure 3.5 are labeled "cpl1," "cpl2", "cpl3" and "cpl4," respectively. The amount of coupled power κ in each component coil image at each level of coupling is also shown in Figure 3.5. The quantitative and qualitative degree of coupling increases steadily for each successive configuration. In addition, while only a subset of the coils had their phases adjusted, the perturbation was sufficient to introduce coupled signal into almost all of the channels. Note that any substantial differences in amplifier gain between various receivers will affect the measured values of coupling power, and thus the values shown are meant only to give an overall sense of the relative amount of coupling at each level.

3.4.b Changes in Noise Correlation

The noise data are illustrated graphically in Figure 3.6. Each plot in Figure 3.6 is a scatter plot that shows the real part of the noise measured in one channel as a function of the real part of the noise in one of the other channels. The noise for each channel that is plotted has been normalized by that channel's noise standard deviation. In this type of plot, completely uncorrelated Gaussian noise will form a circle, while correlated noise will become stretched along a 45 degree line. The plots on the left side of Figure 3.6, which are in the base configuration, show mostly uncorrelated noise. The right side of the figure shows noise from the cpl3 configuration. In this case, several distributions are much more oblong and tilted, indicating increased noise correlation. The plots that are shaded show particularly large differences between the base and cpl3 configurations.

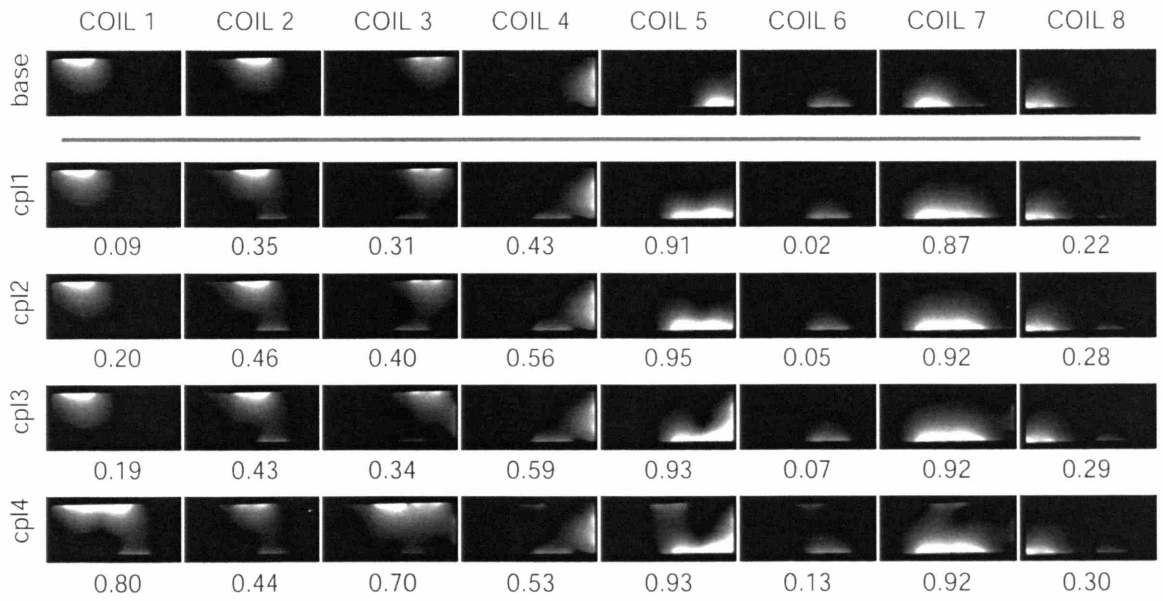

Figure 3.5 Component coil images for the base configuration and four coupling levels (cpl1, cpl2, cpl3, and cpl4). Below each image is the amount of coupling power in that image, calculated using Eq. [3.16]. The coupling power specifies what fraction of the image power in each component coil is the result of coupling from other coils.

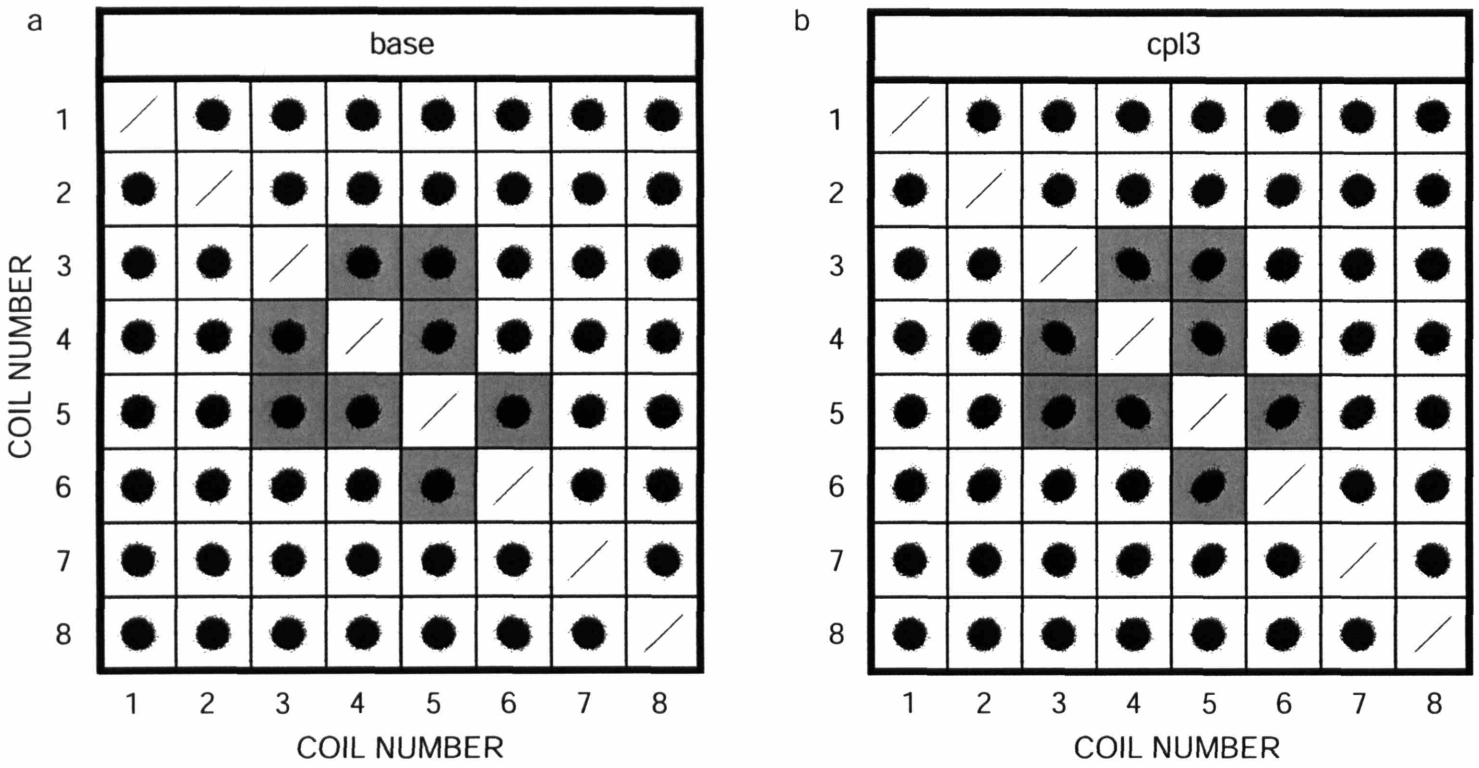

Figure 3.6 Scatterplots of the real part of the noise record for each channel plotted as a function of the real part of the noise record for all other channels. In each case, the noise record is normalized by first dividing by its standard deviation. Circular distributions imply uncorrelated Gaussian noise, while elongated distributions indicate noise correlation. a) Noise in the base configuration. b) Noise in the cpl3 configuration. Shading is included to highlight a subset of plots that show dramatic changes.

Table 3.3 shows the entries of the measured noise correlation matrix Ψ for the base array configuration as well as the cpl3 coupling level. The entries of Ψ are, in general, complex. For clarity, only the absolute values are listed in the table. As expected, there is an overall increase in component-coil noise power (diagonal elements) as well as noise correlations (off-diagonal elements) for the coil array under the influence of inductive coupling. In order to evaluate the effect of noise sources that do not arise from the sample, Table 3.3 shows the entries of Ψ for the cpl3 coupling configuration that would be expected given the predictions of Equation [3.10]. Recall that Equation [3.10] describes the ideal case in which preamplifier noise effects are unimportant. Table 3.3 also shows the percentage changes between the predicted and the measured entries of Ψ. The diagonal parts of the noise correlation matrix are predicted by Equation [3.10] within an average accuracy of 5%, but the off-diagonal are not predicted nearly as well.

3.4.c Effects of Coupling on SNR

The effect of coupling on the SNR of the reconstructed images is shown in Figure 3.7. In all cases, the SNR was measured on a pixel-by-pixel basis and then averaged over the ROI shown in Figure 3.4. Figure 3.7a describes the average SNR obtained when no noise correlation information was used in the reconstruction (i.e. Ψ was set equal to the identity matrix). Figure 3.7b shows the results of an average over the same region for the images that were reconstructed using the measured value of Ψ. The reconstructions that explicitly included Ψ show uniformly increased SNR when compared with the reconstructions that were performed without any noise calibration. Because the SNR for each pixel was computed using 128 independent samples, it can be shown using standard principles of error propagation that the expected variance for the measurement at each pixel is 4-7%. Because the ROI that we used contained 3,360 pixels, the standard error for the mean SNR values shown in Figure 3.7 was about 0.12 %. It should be noted, however, that the actual pixel-by-pixel SNR values that were averaged to produce Figure 3.7 varied dramatically throughout the ROI. This is expected due to the fact that some pixels were much closer to the coil array than others.

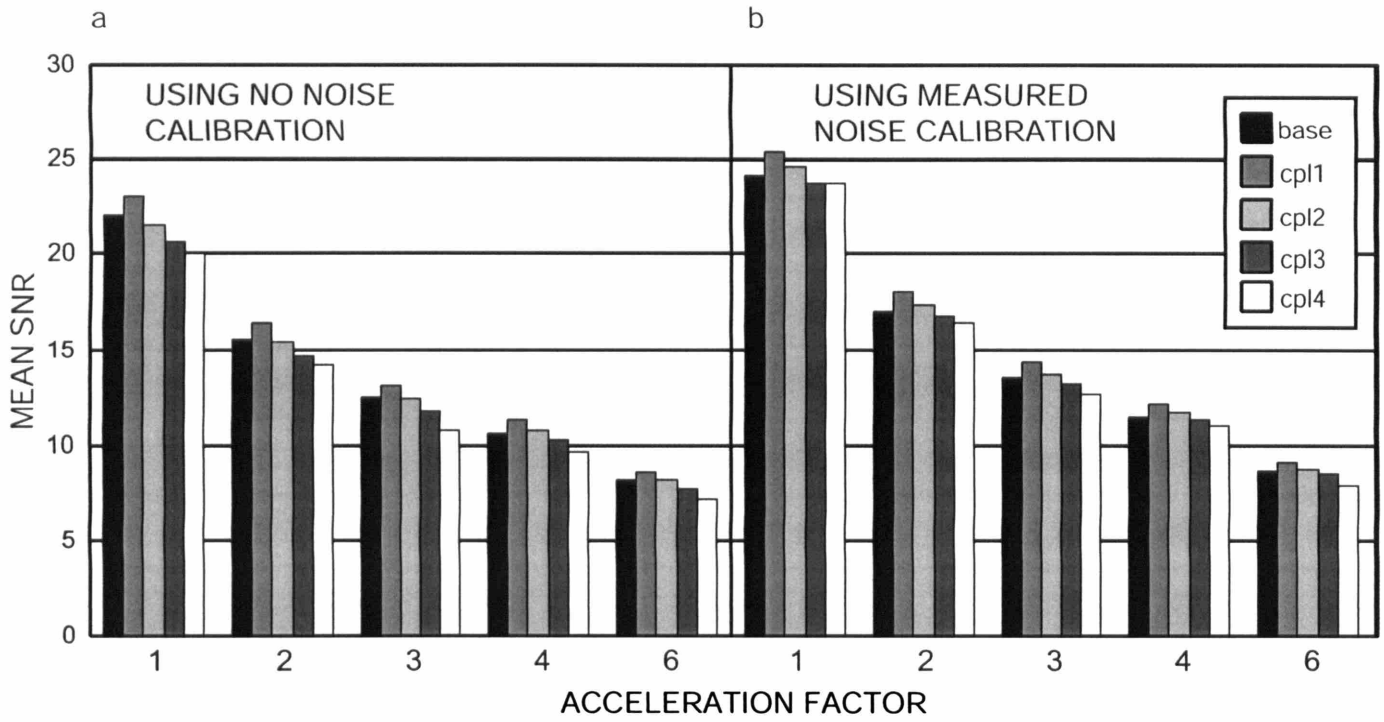

Figure 3.7 Average pixel-by-pixel SNR measured over the central region of the phantom for various coupling levels and acceleration factors. Each cluster of vertical bars represents a different acceleration factor, and each shaded bar represents a different coupling level. The results in the left-hand panel (a) correspond to reconstructions that did not include the noise correlation matrix (it was assumed to be the identity matrix). The results on the right (b) correspond to reconstructions that explicitly included the noise correlation matrix.

Because of the wide range of SNR values found in different regions of the ROI that we used, it is useful to compare the various coupling levels by computing the average pixel-by-pixel percentage changes in SNR from the baseline configuration. The results of this computation are shown in Figure 3.8. As in Figure 3.7, the ROI shown in Figure 3.4 was used. The percentage changes in SNR were, for most levels of coupling, more evenly distributed throughout the ROI than were the overall SNR values (data not shown). In order to illustrate the widths of these distributions, we have included error bars in Figure 3.8 that correspond to the standard error of the mean percentage SNR change. The standard error is defined as the standard deviation of the distribution divided by the square root of the number of pixels in the ROI. For images reconstructed using no noise correlation statistics (Figure 3.8a), the changes in SNR due to coupling are almost uniformly negative and much larger in magnitude than for the images reconstructed using the measured noise correlation (Figure 3.8b). For the images that were reconstructed using the measured noise correlations, each coupling level shows a different magnitude SNR change. For the cpl1 configuration, the SNR increases by 5-7.5% for all acceleration factors. There is little change in SNR for the second and third coupling levels, and there is a 1-7.6% average decrease in SNR at the fourth coupling level.

3.4.d Effects of Coupling on g-Factor

Figure 3.9a shows the average pixel-by-pixel g-factor for each coupling level as a function of acceleration. These g-factor maps were determined using the SNR maps computed above together with Equation [3.17]. As described above, the g-factor is a measure of the amplifications in noise that occur due to the non-unitary transformations used in parallel image reconstructions. This quantity gives a picture of the overall linear independence of the coil sensitivities. A g-factor of 1 suggests nearly complete orthogonality, while a high g-factor reflects strong linear dependence. As expected, all average g-factor values are greater than 1. For each acceleration factor, there is almost no change in g-factor with the introduction of coupling, except for a small increase seen in the g-factor of the cpl4 configuration.

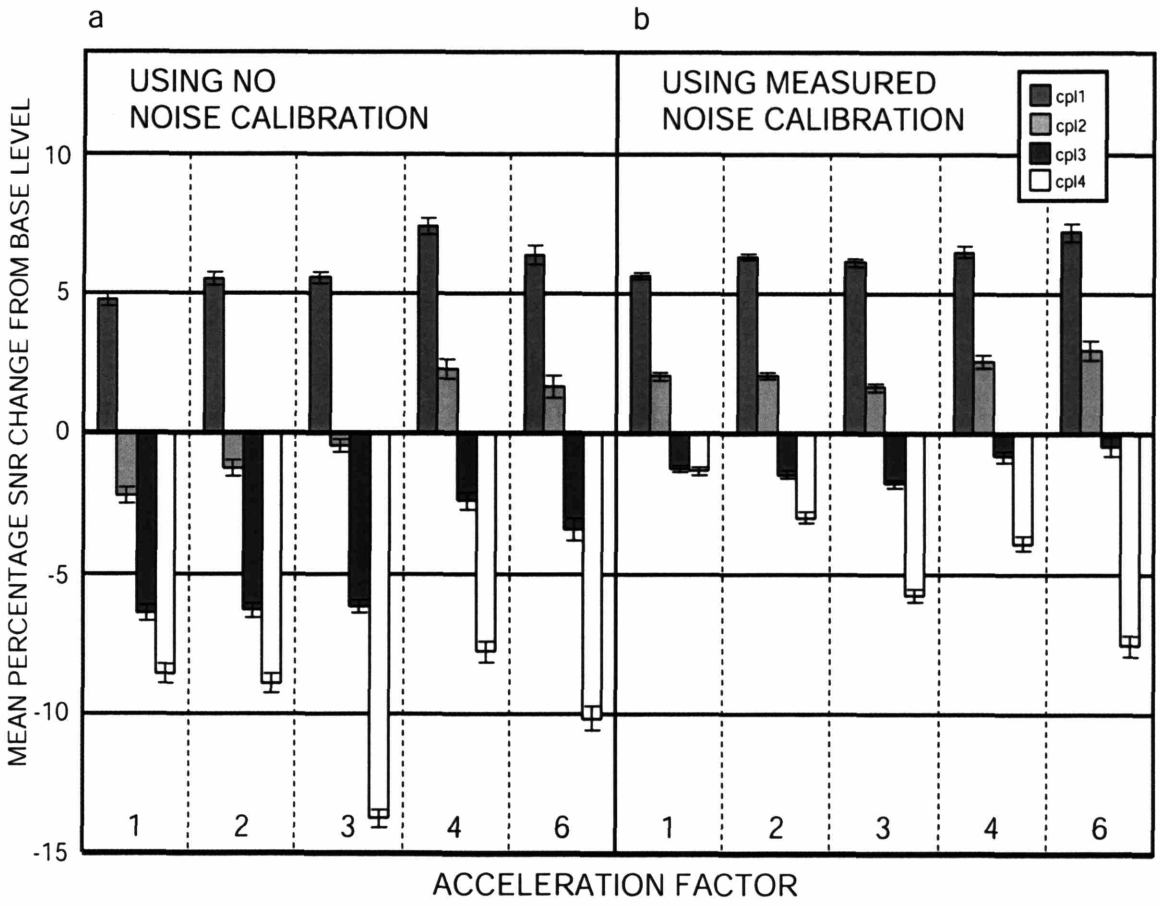

Figure 3.8 Average percentage change in SNR relative to the base level, measured over the central region of the phantom for various coupling levels and acceleration factors. Each cluster of vertical bars represents a different acceleration factor, and each shaded bar represents a different coupling level. Error bars correspond to the estimated standard error of each measurement. The results in the left-hand panel (a) correspond to reconstructions that did not include the noise correlation matrix (it was assumed to be the identity matrix). The results on the right (b) correspond to reconstructions that explicitly included the noise correlation matrix.

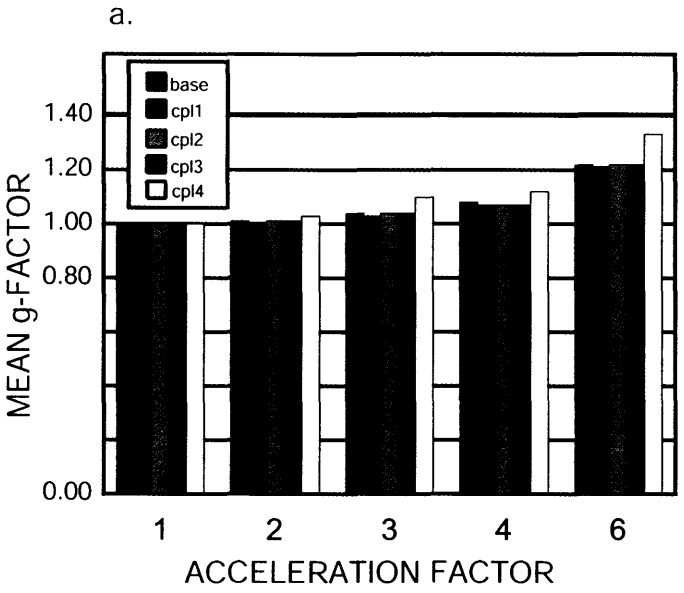

Figure 3.9 (a) Average g-factor in the central region of the phantom for various coupling levels and acceleration factors. Each cluster of vertical bars represents a different acceleration factor, and each shaded bar represents a different coupling level. All results shown correspond to reconstructions that explicitly included the noise correlation matrix.

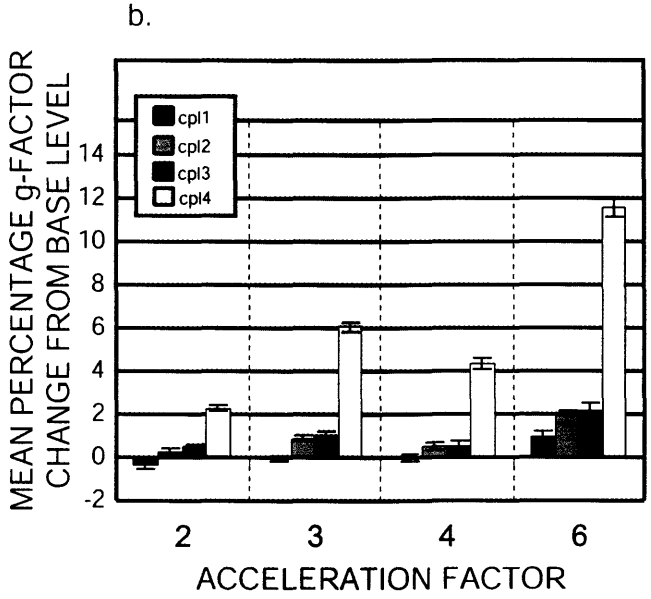

Figure 3.9 (b) Average percentage change in g-factor relative to the base level, measured over the central region of the phantom for various coupling levels and acceleration factors. Error bars correspond to the estimated standard error of the mean for each measurement.

Figure 3.9b shows the average percentage change in g-factor caused by coupling computed on a pixel-by-pixel basis. As in Figure 3.7, we have included error bars that correspond to the standard error of the mean percentage change in g-factor. The changes in g-factor are mostly smaller in magnitude than the overall SNR changes, reflecting the fact that despite the drastic levels of coupling visible in Figure 3.5, the spatial encoding properties of the array remain relatively intact.

3.5 Discussion

The goal of this study was to investigate the effects of inductive coupling between coil array elements on parallel image reconstructions. Specifically, we were interested in evaluating the ways in which coupling affects the ability of coil arrays to encode spatial information. Inductive coupling may affect other aspects of the parallel imaging reconstruction, such as sensitivity processing (87) and numerical conditioning (16), but such effects (though worthy of study in their own right) are beyond the scope of this work.

When coupling is described as a simple linear transformation of coil signals and noise, theoretical arguments demonstrate that coupling does not change the ultimate achievable SNR for a parallel imaging reconstruction. This result is a direct consequence of the fact that, in the linear transformation model, mutual inductance couples noise between array elements in the same ratios that it couples signals. Thus, any loss of distinctness in the measured coil sensitivities is compensated by information stored in the measured noise correlations. This is consistent with the results of Duensing *et al* (84) for non-parallel reconstructions, in which appropriate combinations of signals from two inductively coupled coil elements were shown to achieve the same SNR as the uncoupled array. Our description is distinct from (84), however, in that (84) assumes that the coupling matrix $\mathbf{M_{AB}}$ has previously been measured. In a computational study (66), investigators have suggested that the coil array impedance matrix might be used to derive an expression for $\mathbf{M_{AB}}$. By contrast, our compensation for coupling requires only a measurement of the noise correlation matrix $\tilde{\hat{\Psi}}$. Knowledge of $\tilde{\hat{\Psi}}$ is required to achieve the best possible SNR for both parallel (87) and conventional (1) imaging, even in the absence of inductive coupling.

Our theoretical predictions were tested using an experimental system in which coupling was introduced into a coil array in a controlled fashion by deliberately misadjusting the phases of the preamplifier input impedances at individual coil terminals. Of course, such dramatic misadjustments are unlikely to occur in practice, as most designers will choose to use the correct phase match as part of a well-constructed coil array. Inductive coupling is more likely to occur when changes in coil position or shape (e.g. in flexible arrays) cause changes in the mutual inductance between array elements. We chose not to introduce coupling by varying the coil positions because then we would be unable to distinguish the SNR changes that occurred due to increased coupling from the SNR changes that were due to the spatial displacement of the coil sensitivities.

Parallel image reconstructions of data accelerated by up to a factor of six and with four different degrees of coupling showed average SNR changes of -7.6% to +7.5%. These modest changes in overall SNR were accompanied by similarly small changes in g-factor. Conference proceedings (88-90) have described experiments with different phantoms, coil arrangements, and imaging systems that have yielded similar results.

The majority of our theoretical model, which considers noise sources that arise solely from the sample, does not place any conditions on the amount of coupling that the array elements experience, except that the coupling matrix is non-degenerate and hence invertible. This is not meant to suggest that coupling considerations can be completely eliminated from the design of coil arrays for MRI. For example, matching the impedance of every element within a coil array to a 50-ohm receiver chain can be difficult in the presence of arbitrary amounts of coupling. Thus, some amount of decoupling effort is generally necessary. Our experiments were designed to examine the effects of small amounts of residual coupling arising within an otherwise well-decoupled array.

The changes in SNR that are observed experimentally with the introduction of inductive coupling indicate the presence of noise sources that do not couple in the same way as the MR signals (Table 3.3). These additional sources of noise change the noise correlation statistics such that they no longer precisely offset the changes in the coil sensitivities (Equations [3.11] and

[3.14]). We have shown schematically that changes in the preamplifier noise properties may be sufficient to cause this effect, but the present experimental data are insufficient to either confirm or disqualify this explanation. Further studies are necessary to fully evaluate the effects of the preamplifiers as well as other potential noise sources on the behavior of coupled coil arrays. It is also possible that there are complexities in the noise behavior of our system that are not completely accounted for by the set of correlated random voltage sources that we have assumed in our model. What is clear from this study, however, is that any additional effects are not necessarily deleterious. The results presented here suggest that modest amounts of coupling between coil array elements does not need to have a prohibitive impact on the ability to use a given array effectively for parallel imaging.

In studying the impact of inductive coupling on parallel MRI reconstructions, this chapter has been focused on a practical aspect of building coil arrays that is expected to be important as the density of array elements used for imaging continues to grow. Chapter 2 presented an alternative method of arranging coil elements that is helpful for some aspects of parallel MRI performance. From these two studies, a set of important questions arises: In the process of designing coil arrays for parallel MRI, are the practical issues such as inductive coupling, combined with the need for more imaginative coil designs, the only limiting factors in the potential performance of coil arrays? Is there some more fundamental physical principle that sets boundaries on the use of detectors for spatial encoding? The answers to these questions will be explored in the next chapter.

3.6 Acknowledgements

In addition to the people mentioned in the beginning of this thesis, Randy Duensing, Ray Lee, and Klaas Pruessmann, provided many helpful discussions regarding this work.

3.7 Table 3.1: Preamplifier input impedances and cable phase shifts

Preamplifier input impedances, along with the phase delay (in degrees, measured at 63.86 MHz) introduced by the inserted BNC cables for each coupling level.

	coil number							
	1	**2**	**3**	**4**	**5**	**6**	**7**	**8**
preamplifier input impedance (ohms)	0.7-3.8i	0.8-3.9i	0.7-4.5i	0.6-3.8i	0.8-4.4i	0.7-4.8i	0.7-2.3i	0.6-5i
phase angle cpl1 (degrees)	0	0	0	0	0	17.5	0	0
phase angle cpl2	0	0	0	0	0	24	0	0
phase angle cpl3	0	0	0	23	0	24	0	0
phase angle cpl4	0	40	0	17.5	0	23	0	0

3.8 Table 3.2: Undersampling patterns

Specific 1D undersampling patterns chosen for each amount of net undersampling.

	total acceleration				
	1	**2**	**3**	**4**	**6**
LR acceleration	1	2	3	2	3
AP acceleration	1	1	1	2	2

3.9 Table 3.3 Noise covariance matrix measurements

Absolute value of the measured noise correlation matrix for the BASE and CPL3 coupling levels. The measured CPL3 noise correlation matrix is also compared to that which would have been predicted based on the measured coupling and Equation [3.10].

base noise correlation matrix (x1,000)							
126	8	3	1	6	2	4	7
8	128	2	4	12	5	14	3
3	2	87	4	4	5	1	3
1	4	4	112	14	6	3	2
6	12	4	14	162	3	14	3
2	5	5	6	3	24	2	4
4	14	1	3	14	2	160	4
7	3	3	2	3	4	4	71

cpl3 noise correlation matrix (x1,000)							
126	8	4	5	12	3	7	8
8	131	6	3	38	11	11	5
4	6	98	27	47	8	15	4
5	3	27	107	62	13	28	3
12	38	47	62	348	46	119	9
3	11	8	13	46	24	47	4
7	11	15	28	119	47	263	9
8	5	4	3	9	4	9	71

expected cpl3 noise correlation matrix (x1,000)							
122	6	7	6	8	2	8	10
6	131	10	6	39	13	15	6
7	10	96	24	49	9	19	4
6	6	24	98	54	16	36	3
8	39	49	54	391	60	148	7
2	13	9	16	60	25	58	3
8	15	19	36	148	58	290	7
10	6	4	3	7	3	7	71

percentage change cpl3, expected vs measured							
-4	-17	52	17	-36	-34	17	28
-17	-0	65	91	4.2	21	41	17
52	65	-3	-8	2.9	9.6	25	6.8
17	91	-8	-9	-12	23	28	4.8
-36	4.2	2.9	-12	13	31	25	-17
-34	21	9.6	23	31	1.8	22	-14
17	41	25	28	25	22	10	-21
28	17	6.8	4.8	-17	-14	-21	0

3.10 Appendix A: Electronic Model of Coil Coupling

Each coil l in Figure 3.1a has self-inductance L_l, capacitance C_l, and resistance R_l. In addition, each coil is connected to a preamplifier with low input impedance. The input impedance of each preamplifier as seen by the coil is denoted Z_l^{in}. The signal S_l that is measured in a given channel is proportional to I_l^{preamp}, the current that flows through that channel's preamplifier. If the coils are isolated, then by definition the signal output from any preamplifier is proportional to the voltage induced around that coil element alone ($I_l^{preamp} \propto V_l$). In reality, each pair of coils experiences both inductive and resistive coupling, denoted by $L_{ll'}$ and $R_{ll'}$, respectively. In this situation, the relationship between the induced voltages and preamplifier currents is more complicated.

We define two impedance matrices, $\mathbf{Z}^{coil}$ and $\mathbf{Z}^{input}$, to describe the electrical properties of the coil array:

$$Z_{ll}^{coil} = i\omega L_l - \frac{i}{\omega C_l} + R_l \qquad Z_{ll'}^{coil} = i\omega L_{ll'} + R_{ll'} \qquad [3.18]$$

$$Z_{ll}^{input} = Z_l^{in} \qquad Z_{ll'}^{input} = 0. \qquad [3.19]$$

The value of Z_l^{in} for each coil depends on the preamplifier input impedance, Z_l^{preamp}, as well that coil's particular matching circuitry. The matching components for the coils used in this work (*Nova Medical, Inc., Wakefield MA*) are shown in Figure 3.1b (for a detailed description of circuit designs for similar coils, see (34)). In order to transform the sample resistance R_l to 50Ω, the matching inductors and capacitors are adjusted to have equal and opposite reactances with magnitude $X_l = \sqrt{50R_l}$. In this case, it can be easily shown that the coil input impedance becomes

$$Z_l^{in} = 50\Omega \cdot \frac{R_l}{Z_l^{preamp}}. \qquad [3.20]$$

In vector notation, the set of loop currents $\mathbf{I}^{loop}$ flowing around each coil in response to the induced voltages $\mathbf{V}$ is

$$\mathbf{I}^{loop} = [\mathbf{Z}^{coil} + \mathbf{Z}^{input}]^{-1}\mathbf{V}. \qquad [3.21]$$

The currents measured through the *preamplifiers* – in other words the recorded MR signals – are simply determined from the loop currents that flow around each coil by solving algebraically for the currents along the various paths within each matching network. When these calculations are done, it is found that the current through the preamplifier of coil l is

$$I_l^{preamp} = -i\frac{\sqrt{50R_l}}{Z_l^{preamp}} I_l^{loop}. \qquad [3.22]$$

Thus, the net expression for the MR signal is given by

$$\mathbf{S} \propto \mathbf{I}^{preamp} = \mathbf{\Lambda}\mathbf{I}^{loop} = \mathbf{\Lambda}[\mathbf{Z}^{coil} + \mathbf{Z}^{input}]^{-1}\mathbf{V}, \qquad [3.23]$$

where Λ is a diagonal matrix with $\Lambda_{ll} = -i\sqrt{50R_l} / Z_l^{preamp}$.

Chapter 4.
The Ultimate Intrinsic Signal-to-Noise Ratio for Parallel MRI: Electromagnetic Field Considerations[4.1]

4.1 Introduction

The preceding chapters were devoted to discussing the practical details of coil array construction, together with an exploration of a specific coil array design. While these issues are important, they leave open the question of whether there are more fundamental limits on coil array performance. This chapter seeks to answer that question. The properties of electromagnetic fields within biological tissues are investigated as a way to provide an upper bound on the signal-to-noise ratio that can be derived from a parallel MR imaging experiment. This upper bound will be based only on electromagnetic constraints, and thus will be independent of any specific coil design approach.

[4.1] The work presented in this chapter is very similar to that published as: "Ohliger MA, Grant AK, Sodickson DK. Ultimate intrinsic signal-to-noise ratio for parallel MRI: Electromagnetic field considerations. Magnetic Resonance in Medicine 2003;50(5):1018-1030." Section 4.3 on the planewave basis set has been significantly revised to include a set of modes that were not included in the original calculation. Figure 2 has been added in order to characterize these new modes. All of the figures have been re-generated using the expanded basis set. However, the results from the calculations that incorporate these new modes have prompted no changes in the overall analysis. Therefore, almost all of the text that does not explicitly mention the expanded basis set is unchanged from the original article.

As has been mentioned several times in the course of this dissertation, the reductions in scan time enabled by parallel MRI incur a cost in both the complexity of the scan and the SNR of the final image. The added complexity stems from the fact that all parallel MRI techniques rely on knowledge of the coil sensitivities, which necessitates some form of calibration. The issues involved with coil sensitivity calibration have been thoroughly discussed elsewhere (7,8,11,15,51,52). In addition, every image reconstructed using parallel imaging suffers a SNR loss when compared to the fully gradient-encoded version acquired using the same coil array. There are two reasons for this. First, there is a reduction in the temporal averaging of noise associated with the fact that fewer k-space points are used in the reconstruction. This leads to a SNR loss proportional to the square root of the reduction in scan time. There is little that can be done from the perspective of reconstruction strategy or coil design to prevent this loss. In addition, there can also be amplification of noise because, unlike in conventional Fourier imaging, the transformations used in coil-encoded image reconstructions are not unitary. This leads to an additional spatially-dependent source of SNR loss that is quantified by the so-called geometry factor (11), g, and it is this geometry-associated loss that can be ameliorated through good coil array design.

Roughly speaking, the geometry factor g is minimized when the coil sensitivities are as nearly orthogonal as possible. A procedure has been described in which sensitivity patterns are calculated and used to generate maps of g for a given coil and sample configuration (63). Free parameters such as the coil spacing are systematically adjusted until an acceptable level of SNR performance is reached. While this approach represents a valuable tool for RF coil design, there is still no way to judge how close a given design is to the optimum that can possibly be achieved. Furthermore, such a method provides little direct insight into the design of novel conductor arrangements for parallel imaging.

This chapter offers a method for establishing an upper bound on the SNR performance of coil arrays for parallel imaging. This is accomplished by directly optimizing the spatial encoding properties of the coil sensitivities rather than parametrically varying the arrangement of conductors. Coil sensitivities are constrained by the principle of reciprocity to be the left-hand circularly polarized component of a solution to Maxwell's equations. This confers some degree

of intrinsic smoothness on their spatial sensitivity patterns, which restricts their possible spatial variations. This constraint was formalized by Ocali and Atalar in their calculations of the ultimate intrinsic SNR for conventional gradient-encoded imaging (91). In that work, the coil sensitivities were written in terms of a complete set of basis functions that each individually satisfied Maxwell's Equations. A linear combination was found that minimized the total noise power for a unit signal at a point of interest.

In this study, we extend the algorithm of Ocali and Atalar and apply it to parallel imaging by adding new constraints that are imposed by the sensitivity-encoded reconstruction. These constraints are used to derive a physically intuitive explanation of the limitations of parallel imaging that occur at high levels of acceleration. In addition, we show how coils at higher field strengths offer advantages for parallel imaging above and beyond those already brought about by the larger available spin polarization. We investigate how the electrical conductivity of the sample impacts the use of surface coils for spatial encoding, and we demonstrate how our methodology can guide the choice of different k-space acquisition strategies. Finally, we describe an algorithm for generating a concrete optimal coil sensitivity pattern that can be used to guide future coil designs. Preliminary results from this work were presented previously at the 2002 Meeting of the International Society for Magnetic Resonance in Medicine in Honolulu, Hawaii (92). Other independent investigations using different methodologies were presented in the same forum, reporting some results consistent with those presented here (93-95).

4.2 Theory

We begin by reviewing the general formalism of parallel imaging reconstructions as well as the procedure for determining the optimal SNR combination of any finite number of surface coils. We then discuss how a complete basis set of coil sensitivities can be used in conjunction with the parallel image reconstruction in order to generate a linear combination whose SNR is greater than or equal to any linear combination of physically realizable receiver coils. Finally, we describe a procedure for generating the sensitivity pattern of an idealized receiver coil that would yield the computed optimal SNR.

4.2.a Parallel Imaging Formalism

For the purposes of image reconstruction, the expression for the total MR signal received by the *l*th component coil in an array at k-space point $\mathbf{k}_m$ due to a distribution of transverse magnetization $\rho(\mathbf{r})$ is discretized and written in the form:

$$S_l(\mathbf{k}_m) \approx \sum_{\text{pixels j}} e^{i\mathbf{k}_m \cdot \mathbf{r}_j} C_l(\mathbf{r}_j)\rho(\mathbf{r}_j) + n_l . \qquad [4.1]$$

$C_l(\mathbf{r})$ is the sensitivity function for coil l, which describes the spatial modulation of the image that is induced by inhomogeneities in that coil's reception pattern. n_l is a time-dependent Gaussian random variable representing white noise. The noise received by several detectors simultaneously can be (and usually is) correlated, but the noise accompanying each point in k-space is independent. For an array of L detectors, Equation [4.1] is conveniently written in matrix notation by placing all of the acquired k-space points for coil l into a signal vector $\mathbf{S}_l$. Stacking all of the coil signal vectors $\mathbf{S}_l$ into one column vector **S**, and rearranging the right hand side of Equation [4.1] accordingly, all of the coil information is then joined into a single equation:

$$\mathbf{S} = \begin{pmatrix} \mathbf{S}_1 \\ \mathbf{S}_2 \\ \vdots \\ \mathbf{S}_L \end{pmatrix} = \begin{pmatrix} \mathbf{B}_1 \\ \mathbf{B}_2 \\ \vdots \\ \mathbf{B}_L \end{pmatrix} \boldsymbol{\rho} + \begin{pmatrix} \mathbf{n}_1(t) \\ \mathbf{n}_2(t) \\ \vdots \\ \mathbf{n}_L(t) \end{pmatrix} \equiv \mathbf{B}\boldsymbol{\rho} + \mathbf{n}(t), \qquad [4.2]$$

where **B** is the so-called encoding matrix, which has entries

$$B_{(lm),j} \equiv e^{i\mathbf{k}_m \cdot \mathbf{r}_j} C_l(\mathbf{r}_j) . \qquad [4.3]$$

Grouping the gradient-induced complex exponential phase variation together with the coil sensitivities places the magnetic field gradients and coil sensitivities on equal footing as methods of spatial encoding.

In general, the encoding matrix **B** is rectangular, and the system of linear equations defined by Equation [4.2] will have a well-defined least-squares solution as long as the number of rows in **B** is greater than or equal to the number of columns. This is equivalent to the requirement that the number of coils times the number of acquired k-space points is greater than or equal to the

number of image points to be reconstructed. Because this system of linear equations is consistent, there is typically more than one inverse matrix $\mathbf{B}^{inverse}$ such that $\mathbf{B}^{inverse}\mathbf{B}$ is equal to the identity. It has been shown through the use of Lagrange multipliers (11) and considerations of linear algebra (16) that the minimum net multiplication of noise – and thus the maximum signal-to-noise ratio of the final image – is achieved by using the modified Moore-Penrose pseudoinverse

$$\mathbf{B}^{inverse}_{\text{minimum norm}} = \left(\mathbf{B}^{\dagger}\boldsymbol{\Psi}^{-1}\mathbf{B}\right)^{-1}\mathbf{B}^{\dagger}\boldsymbol{\Psi}^{-1}. \qquad [4.4]$$

For a fully-sampled reconstruction on a Cartesian grid, this expression reduces to the familiar discrete Fourier transform and matched-filter combination used for conventional gradient-encoded imaging with arrays (1). The total noise power P_j at pixel position j is proportional to

$$P_j \sim \left[\left(\mathbf{B}^{\dagger}\boldsymbol{\Psi}^{-1}\mathbf{B}\right)^{-1}\right]_{jj}. \qquad [4.5]$$

Here, $\boldsymbol{\Psi} = \left\langle \mathbf{n}(t)\mathbf{n}^{\dagger}(t)\right\rangle_t$ is the noise covariance matrix, which describes the time-averaged statistical properties of the noise received by the coils, including the amplitude of the noise received by individual coils as well as the amount of correlated noise that exists between each pair of coils. This noise power is incorporated into the expression for the signal-to-noise ratio of an MR experiment (47):

$$SNR(\mathbf{r}_j) \sim \frac{\omega B_0}{\sqrt{4k_B T \cdot P_j}} \qquad [4.6]$$

In this expression, B_0 is the main magnetic field strength, ω is the Larmor frequency, T is the temperature of the system, and k_B is Boltzmann's constant.

4.2.b Optimal SNR

It is important to note that within the theoretical framework outlined in Equations [4.1]-[4.6], adding a new coil sensitivity to the reconstruction can never *decrease* the resulting SNR. In the worst case, the sensitivity will enter the reconstruction with zero weight and thus have no effect. In order to find an upper bound on the possible SNR, it suffices to continually incorporate new

coil sensitivities into the reconstruction until no further SNR improvement is seen, which occurs when no linearly independent coil sensitivities remain to be added. In other words, we seek a basis set of coil sensitivities $C_l(\mathbf{r})$ such that any arbitrary sensitivity $C(\mathbf{r})$ can be represented as a linear combination:

$$C(\mathbf{r}) = \sum_l \alpha_l C_l(\mathbf{r}) . \qquad [4.7]$$

This is accomplished by resorting to the principle of reciprocity, which states that the electromotive force generated around a closed loop due to magnetization **M(r)** some distance away from a detector is proportional to $\mathcal{B}^{\text{coil}}(\mathbf{r})$, the magnetic field that would be generated at the position **r** by a unit current flowing around the loop. In other words (96),

$$V = -\frac{d}{dt}\int \mathbf{M}(\mathbf{r}) \cdot \mathcal{B}^{\text{coil}}(\mathbf{r}) d^3\mathbf{r} . \qquad [4.8]$$

Magnetization precessing in the x-y plane has the form

$$\mathbf{M}(\mathbf{r}) = \text{Re}\left[\rho(\mathbf{r}) e^{-i\omega t} \hat{\mathbf{e}}_-\right], \qquad [4.9]$$

where $\hat{\mathbf{e}}_- \equiv (\hat{\mathbf{x}} - \hat{\mathbf{y}} i)$. The net sensitivity is (80)

$$C(\mathbf{r}) = \mathcal{B}^{\text{coil}} \bullet \hat{\mathbf{e}}_- . \qquad [4.10]$$

The coil sensitivities are not arbitrary spatial functions, but have a specific relationship to a physical magnetic field arising within the sample, and this field must satisfy Maxwell's Equations in a source-free region. Namely,

$$\begin{aligned} \nabla \cdot \mathcal{E} = 0 \qquad & \nabla \times \mathcal{E} = -\frac{\partial \mathcal{B}}{\partial t} \\ \nabla \cdot \mathcal{B} = 0 \quad & \nabla \times \mathcal{B} = \mu \mathbf{J} + \epsilon\mu \frac{\partial \mathcal{E}}{\partial t} \end{aligned} , \qquad [4.11]$$

where μ and ϵ are the permeability and the permittivity of the medium, respectively. For the range of samples and frequencies used in typical MRI experiments, the permeability is equal to that of free space, μ_0. In a linear medium with conductivity σ, the current density, **J**, is equal

to $\sigma\mathcal{E}$. If there is harmonic time dependence such that $\mathcal{B}(\mathbf{r},t) = \mathcal{B}(\mathbf{r})e^{i\omega t}$, Equations [4.11] can be rearranged to give the wave equation:

$$\nabla^2\mathcal{B} = -\left(\mu\epsilon\omega^2 - i\mu\sigma\omega\right)\mathcal{B} \equiv -k^2\mathcal{B}. \qquad [4.12]$$

The magnetic field that satisfies this differential equation can be expanded in any number of complete basis sets

$$\mathcal{B}(\mathbf{r}) = \sum_l \alpha_l \mathcal{B}_l(\mathbf{r}), \qquad [4.13]$$

which will be chosen chiefly to suit the geometry of the system being considered. There are also a set of electric field basis functions,

$$\mathcal{E}(\mathbf{r}) = \sum_l \alpha_l \mathcal{E}_l(\mathbf{r}) \qquad [4.14]$$

that are connected through Maxwell's Equations to the magnetic fields in Equation [4.13]. Inserting the magnetic field from Equation [4.13] into the relation for the sensitivity in Equation [4.10], we generate the complete basis of coil sensitivities that we seek:

$$C(\mathbf{r}) = \sum_l \alpha_l C_l(\mathbf{r}) = \sum_l \alpha_l \mathcal{B}_l(\mathbf{r}) \cdot \hat{\mathbf{e}}_-, \qquad [4.15]$$

The electric fields from Equation [4.14] determine the total noise power P associated with any linear combination of sensitivities

$$\begin{aligned} P = \int \sigma \left|\mathcal{E}\right|^2(\mathbf{r}) d^3\mathbf{r} &= \sum_{l,l'} \alpha_l \alpha_{l'}^* \int \sigma \mathcal{E}_l(\mathbf{r}) \bullet \mathcal{E}_{l'}^*(\mathbf{r}) d^3\mathbf{r} \\ \Psi_{ll'} &\equiv \int \sigma \mathcal{E}_l(\mathbf{r}) \bullet \mathcal{E}_{l'}^*(\mathbf{r}) d^3\mathbf{r} \end{aligned}, \qquad [4.16]$$

where here we have used the field definition of the noise covariance matrix, $\boldsymbol{\Psi}$.

Procedurally, the algorithm for computing the ultimate intrinsic SNR for a parallel imaging reconstruction begins with establishing a basis set for the electromagnetic fields within the sample. That basis set is then used to derive a complete basis set of coil sensitivities. An

encoding matrix is constructed according to Equation [4.3], and Equation [4.16] is used to compute the noise power and noise correlations associated with the basis set:

$$\begin{aligned} \mathbf{B}^{basis}_{(lm),j} &= e^{i\mathbf{k}_m \cdot \mathbf{r}_j} \mathcal{B}_l(\mathbf{r}) \cdot \hat{\mathbf{e}}_- \\ \Psi^{basis}_{l,l'} &\equiv \int \sigma \mathcal{E}_l(\mathbf{r}) \cdot \mathcal{E}^*_{l'}(\mathbf{r}) d^3\mathbf{r} \end{aligned} \quad . \qquad [4.17]$$

These expressions are utilized in a reconstruction that produces the linear combination with the greatest possible SNR, which is proportional to (from Equation [4.6]):

$$SNR^{optimum}(\mathbf{r}_j) \sim \frac{\omega B_0}{\sqrt{4k_B T \cdot \left[\left(\mathbf{B}^{basis\dagger} \Psi^{basis^{-1}} \mathbf{B}^{basis} \right)^{-1} \right]_{j,j}}} . \qquad [4.18]$$

Because the sensitivity profile of any physically realizable RF coil can be expanded as a linear combination of this basis set, the optimization performed above must yield a SNR greater than or equal to that of any set of actual coils.

4.2.c Optimal Coil Sensitivity

In the previous section, we utilized a complete basis set of coil sensitivities to derive an expression for the highest SNR that can be achieved at pixel position $\mathbf{r}_j$. Now, we seek to employ the same basis set to determine a net sensitivity $C^{opt}(\mathbf{r})$ that can be used to acquire an image with that optimal SNR. We will see that, in the most general case, this can be quite complicated because a different optimal sensitivity is specified for *each acquired k-space point.* However, for the special case of uniform Fourier sampling, a single optimal sensitivity can be determined that is independent of the k-space point being acquired.

The optimal sensitivity is determined by taking advantage of the weighting factors determined by the inversion procedure in Equation [4.4]. For a voxel at position $\mathbf{r}_j$, the highest-SNR representation of the transverse magnetization density is given by

$$\begin{aligned}\boldsymbol{\rho}(\mathbf{r}_j)^{opt} &= \left[\left(\mathbf{B}^{inverse}\right)\mathbf{S}\right]_j \\ &= \left[\left(\mathbf{B}^{inverse}\right)\mathbf{B}\boldsymbol{\rho}\right]_j \\ &= \sum_{l,m} B^{inverse}_{j,(lm)} \sum_i e^{i\mathbf{k}_m\cdot\mathbf{r}_i} C_l(\mathbf{r}_i)\rho(\mathbf{r}_i)\end{aligned} \quad . \qquad [4.19]$$

The summation over i in this equation is distinct from the summations over m and l; the sum over i represents a physical integration made possible by the superposition of the fields produced by all of the magnetization in the sample, whereas the summations over l and m can be performed as software post-processing. Nevertheless, for the purposes of this derivation, we can perform the summation over l before the summation over i:

$$\boldsymbol{\rho}(\mathbf{r}_j)^{opt} = \sum_m \sum_i e^{i\mathbf{k}_m\cdot\mathbf{r}_i}\left[\sum_l B^{inverse}_{j,(lm)} C_l(\mathbf{r}_i)\right]\rho(\mathbf{r}_i)\,. \qquad [4.20]$$

Summing over the coil variable l before the physical process of data acquisition is equivalent to using a single coil whose net sensitivity is given by

$$\begin{aligned}C^{opt}_{m,j}(\mathbf{r}) &= \sum_l B^{inverse}_{j,(lm)} C_l(\mathbf{r}) \\ &= \sum_l B^{inverse}_{j,(lm)} \mathcal{B}_l(\mathbf{r})\cdot\hat{\mathbf{e}}_-\end{aligned} \quad . \qquad [4.21]$$

In other words, if a coil with this sensitivity profile is used to acquire k-space point $\mathbf{k}_m$, the image that is produced will have the largest possible SNR at position $\mathbf{r}_j$. As mentioned earlier, this most general situation requires the creation of a different coil sensitivity profile before acquiring each k-space point.

The procedure for deriving the optimum coil sensitivity is greatly simplified in the special case where the k-space sample and target pixels lie on a Cartesian grid. This simplification arises because uniform undersampling in the spatial-frequency domain corresponds to simple aliasing in the image domain. Pixels throughout the FOV "fold" onto each other, and each pixel in the reduced-FOV image is linearly related to exactly R pixels in the full-FOV image. In this case, the encoding matrix can be transformed into a block-diagonal form, and the reconstruction of any pixel may be accomplished by inverting a small matrix containing the values of each sensitivity function evaluated at that pixel's aliasing positions (5,11,16). This smaller matrix inverse yields

only one weighting coefficient $\beta_{(jl)}$ for each component coil l for an optimal reconstruction at pixel position $\mathbf{r}_j$. The dependence on k-space position in Equation [4.21] is removed and the optimal sensitivity may be written as

$$C_j^{opt}(\mathbf{r}) = \sum_l \beta_{(jl)} C_l(\mathbf{r}) \text{ (Cartesian sampling).} \qquad [4.22]$$

The precise relationship between the general expression for the coil sensitivities in Equations [4.20] and [4.21] and the special case of Equation [4.22] is discussed in Appendix A. In view of the computational simplifications that result from the block-diagonal form of the encoding matrix together with the physical insight afforded by the generation of a single optimal coil sensitivity, we employ a uniform sampling of k-space for all of the examples in this work.

It is important to observe that, regardless of the sampling pattern, the weighting coefficients specified by both Equations [4.21] and [4.22] are always a function of the pixel $\mathbf{r}_j$ that is to be reconstructed. Thus, every point will have a different net sensitivity pattern associated with it that corresponds to maximum achievable SNR at that point. Furthermore, because encoding functions that are used to construct the inverse in Equation [4.4] are functions of the undersampled set of k-space points, the optimum SNR will generally depend on the details of the k-space acquisition pattern. At the simplest level, this implies that we should expect a separate optimum for each acceleration factor. Finally, the shape and composition of the sample will impact our reconstruction through both the basis functions that are used and the value of the overlap integrals used to construct the noise covariance matrix in Equation [4.16]. Thus, when we ask about the best possible performance that can be achieved using parallel imaging, we must specify 1) the point where we want to optimize the SNR; 2) the specific pattern of k-space sampling; and 3) the shape and electrical characteristics of the sample.

4.3 Computational Methods

4.3.a Plane wave Basis Set

Any procedure for computing the optimal SNR of a parallel imaging reconstruction must give a result identical to the optimal gradient-encoded reconstruction in the limit of no acceleration. For this reason, our initial implementation employs an identical simulated sample and a similar set of

basis functions to those used in (91). The electric and magnetic fields in the sample are expanded in terms of a complete set of plane waves,

$$\begin{aligned} \mathcal{B}(\mathbf{r}) &= \sum_l \mathcal{B}_l^{+,-} e^{i\mathbf{k}_l\cdot\mathbf{r}-i\omega t} \\ \mathcal{E}(\mathbf{r}) &= \sum_l \mathcal{E}_l^{+,-} e^{i\mathbf{k}_l\cdot\mathbf{r}-i\omega t} \end{aligned} \quad \textit{where} \quad \begin{aligned} \mathcal{B}_l^{+,-} &= \frac{\mathbf{k}_l \times \mathcal{E}_l^{+,-}}{\omega} \\ \mathcal{E}_l^{+,-} \cdot \mathbf{k}_l &= 0 \end{aligned} . \qquad [4.23]$$

The superscript (+,-) accounts for the fact that two orthogonal polarizations of each field are possible for a given choice of $\mathbf{k}_l$.

At a given frequency ω, the values of $\mathbf{k}_l$ are constrained by the dispersion relation in Eq. [4.12]. A complete set of modes that satisfy Maxwell's Equations is obtained by choosing two sets of unit vectors, $\hat{\mathbf{k}}_l^r$ and $\hat{\mathbf{k}}_l^i$. It is easy to show that if

$$\mathbf{k}_l = \eta\hat{\mathbf{k}}_l^r + i\upsilon\hat{\mathbf{k}}_l^i, \qquad [4.24]$$

then the constants, η and υ, are given by,

$$\begin{aligned} \eta^2 &= \frac{\mu\epsilon\omega^2}{2}\left[1+\sqrt{1+\frac{\sigma^2}{\epsilon^2\omega^2\left(\hat{\mathbf{k}}_l^r\cdot\hat{\mathbf{k}}_l^i\right)^2}}\right] \\ \upsilon^2 &= \frac{\mu\epsilon\omega^2}{2}\left[-1+\sqrt{1+\frac{\sigma^2}{\epsilon^2\omega^2\left(\hat{\mathbf{k}}_l^r\cdot\hat{\mathbf{k}}_l^i\right)^2}}\right] \end{aligned} . \qquad [4.25]$$

Each plane wave propagates in the direction $\hat{\mathbf{k}}_l^r$ with wavelength

$$\lambda = \frac{2\pi}{|\eta|}. \qquad [4.26]$$

Simultaneously, each plane wave also falls off exponentially as it penetrates the sample in the direction $\hat{\mathbf{k}}_l^i$, with a skin depth given by

$$\tau = \frac{1}{|\upsilon|}. \qquad [4.27]$$

4.3.b Selection of Plane wave Modes

Each basis function, $\mathcal{B}_l^{+/-}(\mathbf{r})$, is defined by 1) the unit vectors, $\hat{\mathbf{k}}_l^r$ and $\hat{\mathbf{k}}_l^i$, and 2) the polarization of the electromagnetic field. If all propagation and damping vectors are included, and if both polarizations are used, then all possible solutions to Maxwell's Equations will have been considered. In practice, we approximate the full set of unit vectors by choosing finite samples that are uniformly distributed on a unit sphere. Each pair of unit vectors defines one plane wave mode. If there are *n* modes, then after taking the polarization into account, there will be 2*n* total basis functions.

Note that the original presentation by Ocali and Atalar (91) as well as the initial publication of the current work (97) considered the special case where $\hat{\mathbf{k}}_l^r \cdot \hat{\mathbf{k}}_l^i = 1$, and therefore only one set of unit vectors was necessary to specify those basis functions.

Uniform distributions of unit vectors were obtained by choosing points randomly from the surface of a unit sphere. There are several methods of choosing points randomly from a sphere (98). We used the following simple approach. For each unit vector, two random numbers, ϕ and z, were chosen from the independent uniform distributions,

$$\begin{aligned} 0 < \phi < 2\pi \\ -1 < z < 1 \end{aligned}. \qquad [4.28]$$

A uniformly distributed set of unit vectors was obtained by setting,

$$\begin{aligned} \theta &= \cos^{-1}(z) \\ \hat{k}_x &= \cos(\phi)\sin(\theta) \\ \hat{k}_y &= \sin(\phi)\sin(\theta) \\ \hat{k}_z &= \cos(\theta) \end{aligned}. \qquad [4.29]$$

The coefficients in Eq. [4.25] are singular when $\hat{\mathbf{k}}_l^r \cdot \hat{\mathbf{k}}_l^i = 0$. Indeed, modes with small values of $\hat{\mathbf{k}}_l^r \cdot \hat{\mathbf{k}}_l^i$ are rapidly oscillating and are also rapidly exponentially damped. This rapid damping

leads to modes that contribute a large amount of noise and receive only a small amount of signal. Eventually, the inclusion of small values of $\hat{\mathbf{k}}_l^r \cdot \hat{\mathbf{k}}_l^i$ will degrade the numerical stability of the computation. For our calculations, we required all of our planewave modes to have a value of $\hat{\mathbf{k}}_l^r \cdot \hat{\mathbf{k}}_l^i > 0.05$. When modes were included with $\hat{\mathbf{k}}_l^r \cdot \hat{\mathbf{k}}_l^i$ below 0.05, the calculations became unstable. The implications of this choice of cutoff will be addressed in a later section.

4.3.c Model Sample

A schematic diagram of the sample geometry used in this work (as well as in Ref. (91)) is shown in Figure 4.1. This model was chosen to closely approximate a human torso. It consisted of an elliptic cylinder with length 61.2 cm with its longitudinal axis aligned with the main magnetic field. The semi-major and semi-minor axes were 17.05 cm and 12.4 cm long and were oriented along the x- and y-axes, respectively. The cylindrical sample was assumed to have uniform conductivity σ, permittivity ϵ, and permeability μ. For the majority of these calculations, the permittivity and conductivity were chosen to match the bulk electrical properties of liver (Table 4.1).

For a sample composed of a finite elliptic cylinder, the entries of the noise covariance matrix $\mathbf{\Psi}$ can be computed analytically in terms of the plane wave basis functions in Equation [4.23]. If the cylinder has longitudinal length *l*, horizontal axis length 2*a*, and vertical axis length 2*b*, ((91) Eq. B14):

$$\Psi_{ll'} = \sigma \int \boldsymbol{\mathcal{E}}_l(\mathbf{r}) \cdot \boldsymbol{\mathcal{E}}_{l'}^*(\mathbf{r}) d^3\mathbf{r} = \boldsymbol{\mathcal{E}}_l \cdot \boldsymbol{\mathcal{E}}_{l'}^* 4\pi\sigma abl \frac{\sin(\kappa_z)}{\kappa_z} \frac{J_1(\kappa_r)}{\kappa_r} \qquad [4.30]$$

where J_1 is the first-order Bessel function, and we have made the following definitions:

$$\begin{aligned} \tilde{k}_\gamma &\equiv k_{l\gamma} - k_{l'\gamma}^*, \quad (\gamma = x, y, z) \\ \kappa_r &\equiv \sqrt{a^2\tilde{k}_x^2 + b^2\tilde{k}_y^2} \\ \kappa_z &\equiv \tilde{k}_z l \end{aligned} \qquad [4.31]$$

Note that the magnitude of the wave vectors are, in general, complex, and we have accounted for a small typographical error in the original form of the expression presented in (91).

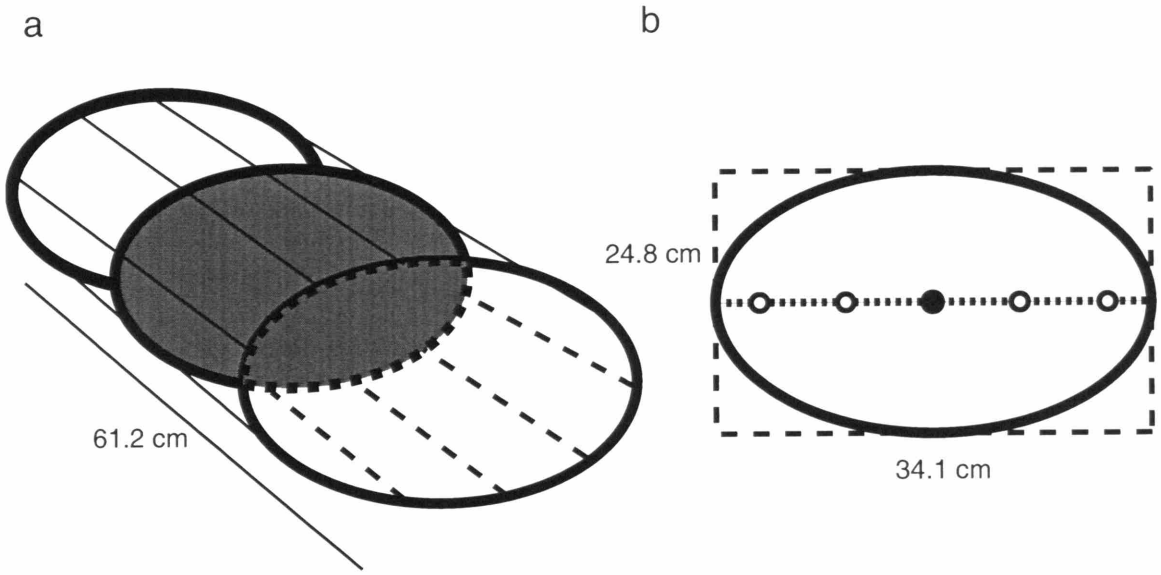

Figure 4.1 a) Schematic diagram of the simulated sample. It consists of an elliptical cylinder with uniform conductivity, permittivity, and permeability. The cylinder is 61.2 cm long and has semi-major and semi-minor axes of 12.4 cm and 17.05 cm, respectively. b) FOV used in all calculations, which is a rectangle just large enough to contain the entire sample. Shown schematically are the central point-of-interest (filled circle) and four aliasing points (empty circles) that would result from a 5-fold uniform undersampling in the x-direction.

4.3.d Computational Details

The calculations presented here used an axial plane through the center of the cylinder together with a rectangular field-of-view that circumscribed the sample (Figure 4.1b). Uniform k-space sampling patterns were chosen, taking advantage of the simplifications described in Section 4.2.c. The chief remaining practical difficulty in implementing this calculation was the inversion of the noise covariance matrix $\boldsymbol{\Psi}$, which can be numerically unstable. One source of numerical instability is the singularity in the coefficients defining the wave vector that occurs when $\hat{\mathbf{k}}_l^r \cdot \hat{\mathbf{k}}_l^i$ approaches zero. This problem, along with our proposed solution, has been discussed in Section 4.3.b.

Another source of numerical instability is related to the fact that the plane wave basis set varies very slowly at MR wavelengths and exhibits only small variations over the sample's short length scales. While the inverse of the noise covariance matrix can be poorly conditioned, this ill-conditioning is traded for the ability to analytically compute the noise power and noise correlations as indicated in Equation [4.30]. Other basis sets may yield more numerically stable inversions, but those advantages may eventually be obviated by corresponding difficulties that result from the need to use numerical integration to calculate the noise covariance matrix elements. In our calculations, we compensated for the numerically unstable inversion of $\boldsymbol{\Psi}$ by using Mathematica *(Wolfram Research, Champaign IL)* with extended numerical precision. The majority of computations were performed using 60 digits of precision. Computations at 9T were performed using 100 digits of software precision. The results from the matrix inverse were then exported to Matlab (*The MathWorks, Natick MA)*, which was used to display and analyze all of the results. Because of further numerical instabilities that might occur near the edge of the sample, the most distant aliasing point was placed .05 cm interior to the sample edge, which was consistent with a finite-resolution reconstruction.

4.4 Results

4.4.a Characterization of Basis Functions

Figure 4.2 describes basic properties of the planewave basis functions as a function of the parameter $\hat{\mathbf{k}}_l^r \cdot \hat{\mathbf{k}}_l^i$. Plot 4.2a shows the value of $\hat{\mathbf{k}}_l^r \cdot \hat{\mathbf{k}}_l^i$ for 1,400 randomly chosen basis functions (700 modes). The distribution of values for $\hat{\mathbf{k}}_l^r \cdot \hat{\mathbf{k}}_l^i$ is uniform above the cutoff value of 0.05.

Plot 4.2b is a graph of the wavelength λ and skin depth τ as a function of $\hat{\mathbf{k}}_l^r \cdot \hat{\mathbf{k}}_l^i$. As $\hat{\mathbf{k}}_l^r \cdot \hat{\mathbf{k}}_l^i$ approaches zero, the wavelength decreases, implying faster oscillations, but the skin depth decreases as well.

The remaining plots in Figure 4.2 examine the contribution of each mode to the final reconstruction of various sample points. Recall from Section 4.2.c and appendix A, that for Cartesian k-space sampling, the encoding matrix inversion for reconstruction of a point, $\mathbf{r}_j$, yields a single coefficient, $\beta_{(jl)}$, for each component sensitivity. Multiplication by the coil sensitivity, $C_l(\mathbf{r}_j)$, gives a normalized sensitivity weighting that is independent of any overall scaling of the sensitivities

$$w_{(jl)} = \left|\beta_{(jl)}\right|\left|C_l(\mathbf{r}_j)\right|. \qquad [4.32]$$

Plots (c, e, g) in Figure 4.2 show $w_{(jl)}$ as a function of $\hat{\mathbf{k}}_l^r \cdot \hat{\mathbf{k}}_l^i$ for each mode in the reconstruction of points (c) at the center of the ellipse at 1.5 T; (e) 15 cm along the x-axis of the ellipse at 1.5 T; and (g) at the center of the ellipse at 9 T. Plots (d, f, h) show the behavior of $w_{(jl)}$ using the same parameters in a reconstruction accelerated by a factor of 8. In all cases, the reconstruction weights decrease by several orders of magnitude as the values of $\hat{\mathbf{k}}_l^r \cdot \hat{\mathbf{k}}_l^i$ become smaller. The differences in weighting are more pronounced at the center of the ellipse than at the 15 cm position. In addition, the differences are more pronounced at 1.5 T than they are at 9 T. The smaller weighting coefficients associated with basis functions that have small values of $\hat{\mathbf{k}}_l^r \cdot \hat{\mathbf{k}}_l^i$ suggest that these basis functions make a smaller contribution to the final linear combination, and thus a smaller contribution to the final SNR.

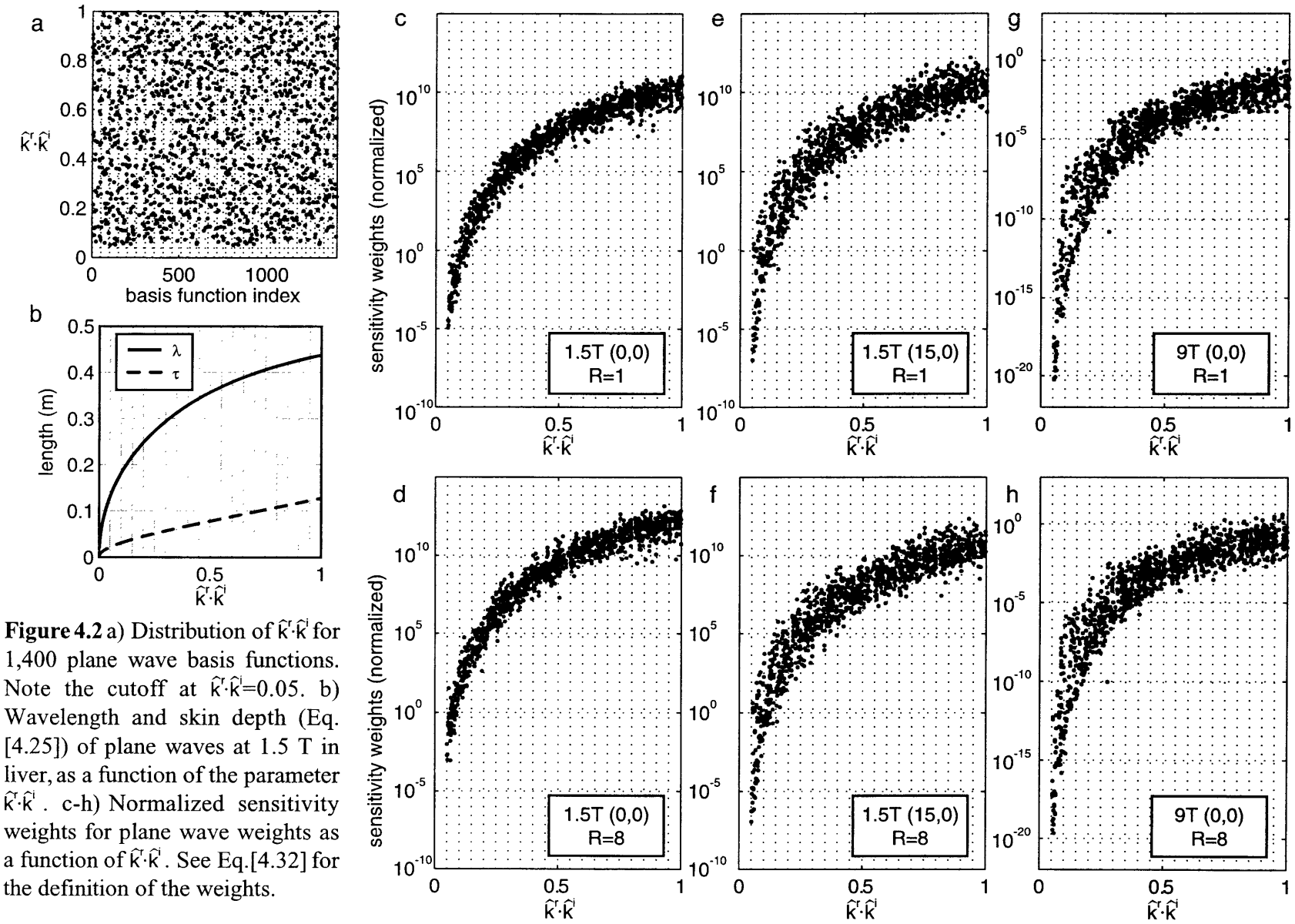

Figure 4.2 a) Distribution of $\hat{k}^r \cdot \hat{k}^i$ for 1,400 plane wave basis functions. Note the cutoff at $\hat{k}^r \cdot \hat{k}^i = 0.05$. b) Wavelength and skin depth (Eq. [4.25]) of plane waves at 1.5 T in liver, as a function of the parameter $\hat{k}^r \cdot \hat{k}^i$. c-h) Normalized sensitivity weights for plane wave weights as a function of $\hat{k}^r \cdot \hat{k}^i$. See Eq.[4.32] for the definition of the weights.

4.4.b Numerical Convergence

Figure 4.3 illustrates the convergence of our calculations as the number of plane wave modes is increased. As mentioned earlier, the permittivity and conductivity were chosen to match the bulk electrical properties of liver (Table 4.1). Each column demonstrates the convergence of the optimal SNR for a different imaging situation. Plot (a) shows the SNR optimized at the center of the cylinder, for imaging performed at a main magnetic field strength of 1.5 T. The top line of the plot is the result computed for a fully gradient-encoded reconstruction, while each line below that is the result after applying successively greater amounts of undersampling along the x-axis. Plot (b) shows, on a logarithmic scale, the fractional change in computed SNR for every 100 new modes that are added to the computation. Plots (c) and (d) describe the same computations for imaging performed at a main magnetic field strength of 5 T. Plots (e) and (f) are computed with a 1.5 T main magnetic field, but with undersampling along the y-axis. Finally, (g) and (h) illustrate the behavior of the optimal SNR for 1.5 T at a point 7.5 cm from the center of the ellipse along the x-axis. Because there are two polarizations associated with each mode, the total number of basis functions is twice the number of modes.

In all cases, the SNR appears to be approaching a limiting value as the number of modes is increased. Because the sensitivity of any physically realizable coil array may be represented as a linear combination of plane waves, each optimum represents the best SNR that may be achieved with any possible coil array for that imaging situation. All plots shown in this chapter describe only the geometry-related change in SNR that occurs due to the reconstruction. The square root effect of reduced noise averaging has been removed for clarity. The SNR at higher levels of acceleration converges more slowly than at lower levels. Convergence is also slower for points of interest closer to the edge of the sample. The final data point in each of these plots, which was computed by including 700 modes and required the inversion of a 1,400 by 1,400 square matrix, represents the limit of our computing resources using the 60-digit software precision arithmetic described above. Unless otherwise noted, the results described in this study represent the outcome of a 700-mode computation that has changed less than 1% from the 600-mode computation. Some data included in this study are the result of a 700-mode computation that has changed between 1% and 10% from the 600-mode computation. These points are marked with a "*".

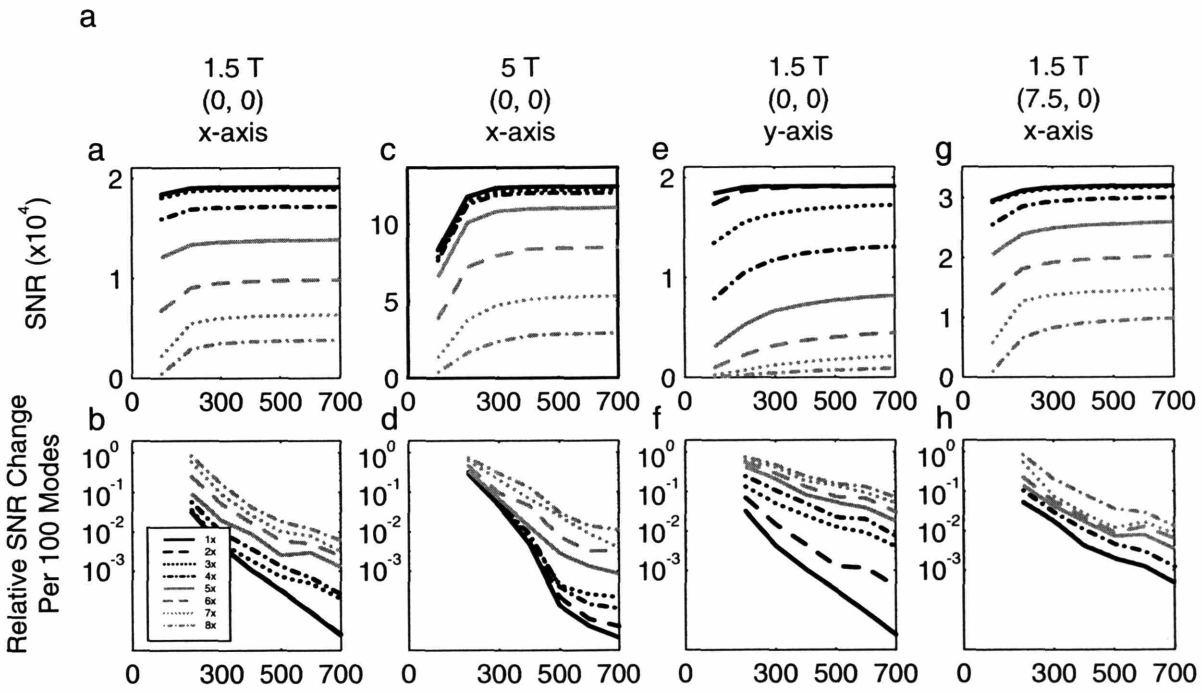

Figure 4.3 Convergence of the plane wave SNR optimization. a) Optimal intrinsic SNR calculated at the center of the uniform elliptical cylinder (Fig. 4.1) as a function of the number of plane wave modes used in the calculation. The field strength is 1.5 T and undersampling is along the x-axis. Each curve represents a different amount of acceleration. b) Log plot of the relative change in SNR per 100 modes as a function of the number of modes used in the reconstruction. Once again, each curve represents a different acceleration level in the x-direction. The remaining graphs show results from the same calculations as (a,b) with the following parameters: c,d) main field strength 5 T, point of interest (0,0), undersampling along the x-axis. e,f) main field strength 1.5 T, point of interest (0,0), undersampling along the y-axis. g,h) main field strength 1.5 T, point of interest (7.5,0), undersampling along the x-axis.

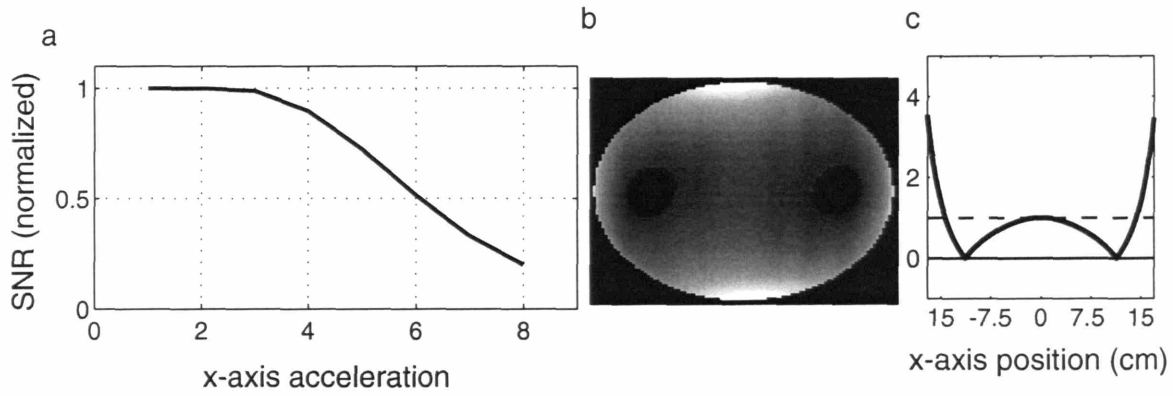

Figure 4.4 a) Optimal SNR at the center of the uniform elliptical cylinder (Fig. 4.1) at 1.5 T as a function of the degree of undersampling along the x-axis. b) Absolute value of the optimal left-hand circularly polarized magnetic field for 3-fold undersampling along the x-axis. This corresponds to the sensitivity of a coil designed to maximize the SNR at the center of the ellipse. The net field is unity at the center of the ellipse and zero at all of the potential aliasing positions. c) Profile along a horizontal line through the center of the sensitivity plot shown in (b).

4.4.c Overall SNR Behavior

The optimal SNR for a point at the center of the elliptic sample as a function of acceleration is shown in Figure 4.4a. There is very little penalty paid for acceleration until a reduction factor of five, at which point the maximum attainable SNR drops precipitously. For the purposes of this discussion, we describe the SNR "cutoff" as the point where the SNR (excluding the effects of temporal averaging) drops to 50% of the maximum. This dramatic drop in the SNR upper bound represents a fundamental limit on receiver-coil spatial encoding. In Figure 4.4b, the weighting

factors obtained from the 700-mode reconstruction are used with Equation [4.22] to calculate the net coil sensitivity that corresponds to the optimal solution for an acceleration factor of 3. Figure 4.4c shows a single profile along the x-axis. For the sensitivity plots and the sensitivity profiles shown in Figures 4.4 and 4.6, the convergence of the particular sensitivity values is typically slightly slower than the convergence of the overall SNR. The sensitivity for points in the central part of the sample generally changed by less than 10% between the 600- and 700-mode calculation, while it changed from 10-20% for some points close to the sample edge.

The optimum coil sensitivity has value one at the center and goes to zero at all of the aliasing points. This is consistent with the idea of using parallel imaging to "unfold" pixels that were overlapped due to aliasing. In principle, a single radiofrequency coil could be constructed with the sensitivity shown in Figure 4.4 in order to specifically reconstruct the central point. However, a practical coil array would most likely consist of multiple coils that are combined during the image reconstruction to match this sensitivity as closely as possible (see Discussion).

4.4.d SNR Dependence on Spatial Position

Figure 4.5 examines the parallel imaging reconstruction as the point of interest moves closer to the edge of the sample. Plots (a) and (b) show the behavior of the optimal achievable SNR as a function of position along the x-axis of our sample at 1.5 T and 5 T, respectively. Because of the symmetries in our simulated sample, only results for the positive x-axis are shown. For all acceleration factors and both field strengths, the optimal SNR increases monotonically as the distance from the center is increased. Plots (c) and (d) show results from the same calculation, but normalized such that at every position, the SNR for the unaccelerated reconstruction is set to one. At both field strengths, the geometry-related loss in SNR due to parallel imaging is reduced for points closer to the edge of the sample.

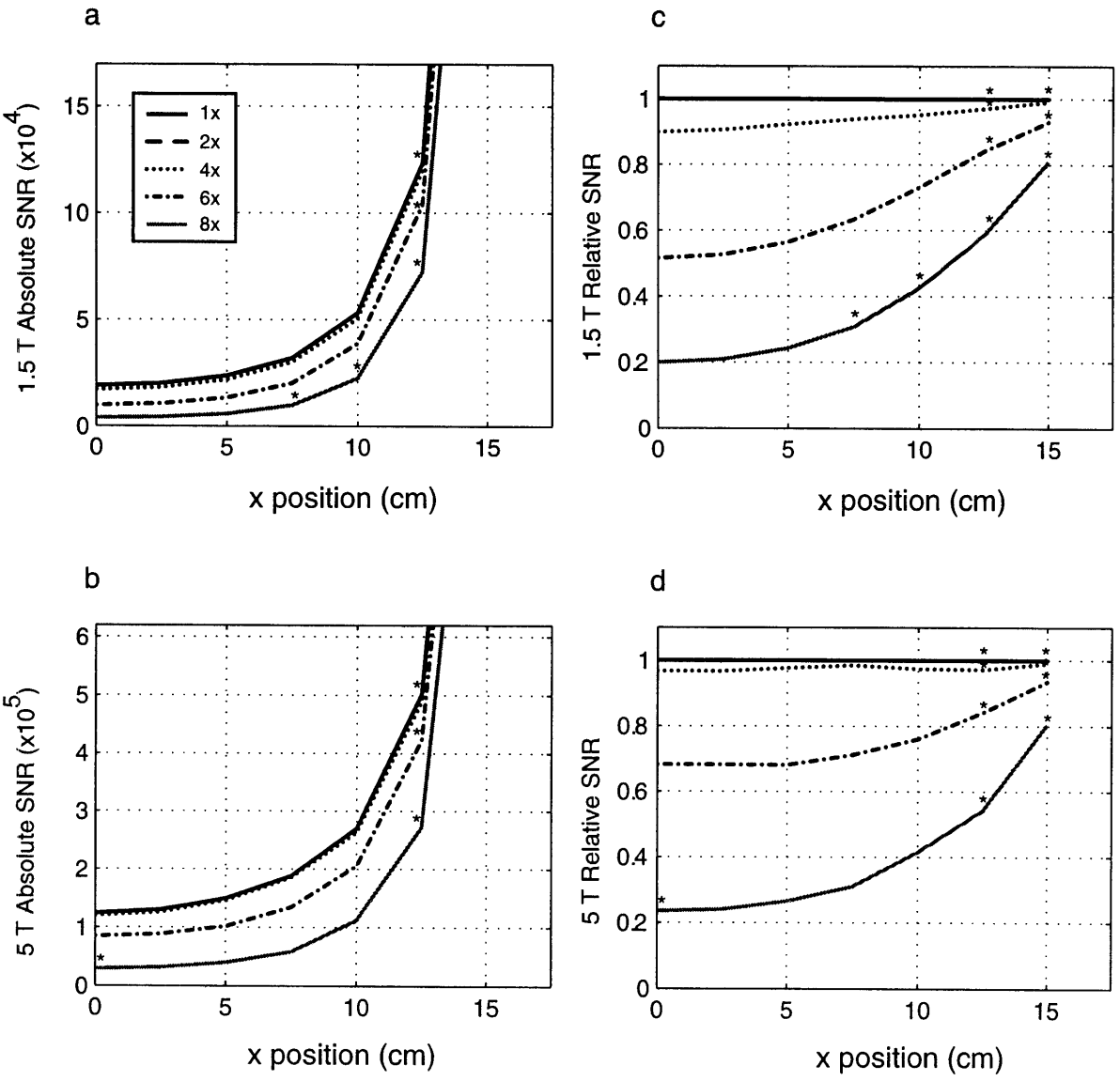

Figure 4.5 a,b) Optimal SNR for points along the x-axis of the central axial plane from the uniform elliptical cylinder (Fig. 4.1) at 1.5 T (a) and 5 T (b). (c,d) Optimal SNR for points along the x-axis, normalized such that the unaccelerated reconstruction has SNR equal to one for 1.5 T (c) and 5 T (d).

4.4.e SNR Dependence on Field Strength

In Figure 4.6, the optimal performance of parallel imaging reconstructions is plotted as a function of acceleration at different field strengths. The conductivity and permittivity at each Larmor frequency are adjusted to match the electrical properties of liver (Table 4.1, (99)). In Figure 4.6a, the five curves are all plotted on the same scale, while in Figure 4.6b, the SNR is independently normalized at each field strength so that the SNR of the unaccelerated reconstruction is always equal to 1. This removes from consideration an overall increase in SNR due mostly to increased spin polarization at higher field strengths that is independent of acceleration. As the field strength increases, the point at which the relative SNR drops off is pushed towards higher accelerations. These effects are more pronounced for higher field strengths. For the 1.8-fold increase in field from 5 T to 9 T, there is a dramatic increase in the spatial-encoding capabilities of the coil sensitivities, while for the 2-fold increase in field from 1.5 T to 3 T, there is almost no change in performance. Figure 4.6c shows SNR values for a reconstruction that is optimized at a point on the x-axis 10 cm from the center of the sample. As in Figure 4.6b, the SNR values have been normalized individually for each field strength. In this case, the field strength dependence of the SNR cutoff is markedly reduced.

The optimal sensitivity plots corresponding to reconstructions at various field strengths and levels of acceleration are shown in Figure 4.7. At higher fields, the optimal sensitivities have many more ripples than they do at low fields. For large amounts of acceleration at smaller field strengths, the sensitivity rises dramatically at the edge of the sample. The heightened sensitivity to noise sources in this region accounts for the dramatic decreases in SNR seen in Figure 4.7. Also note that the "twisting" effect of selecting the left-hand rotating component of the magnetic field is more pronounced at the higher field strengths.

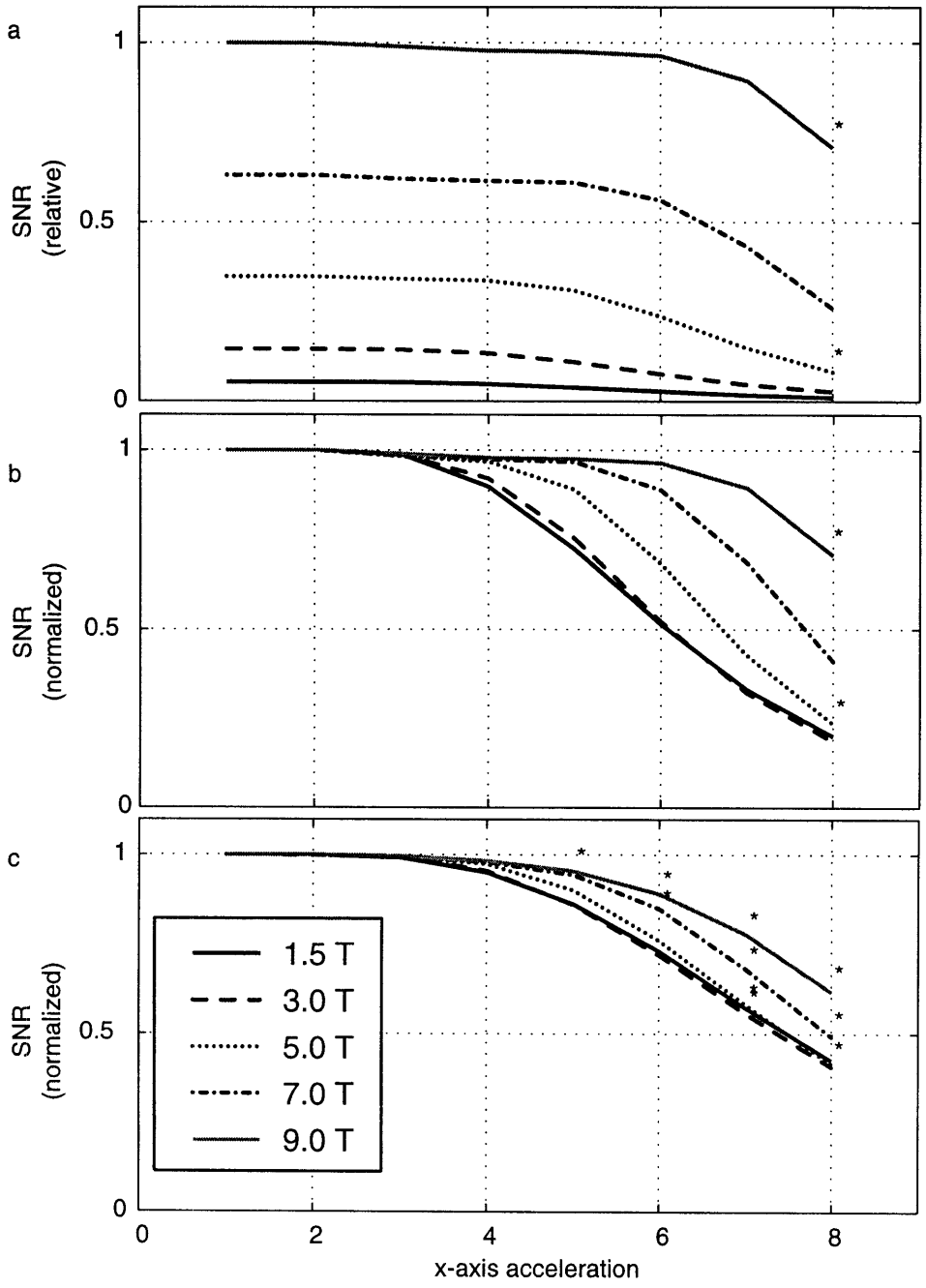

Figure 4.6 a) Optimal SNR at the center of the uniform elliptical cylinder (Fig. 4.1) as a function acceleration and field strength. Conductivity and permittivity match those of liver at each field strength, and undersampling is in the x-direction. b) The plots from (a) are independently normalized so that the SNR for the unaccelerated reconstruction is 1 at each field strength. c) Normalized SNR as in (b), but for a point 10 cm displaced from the center along the x-axis. Points marked with an asterisk indicate slower convergence (see text).

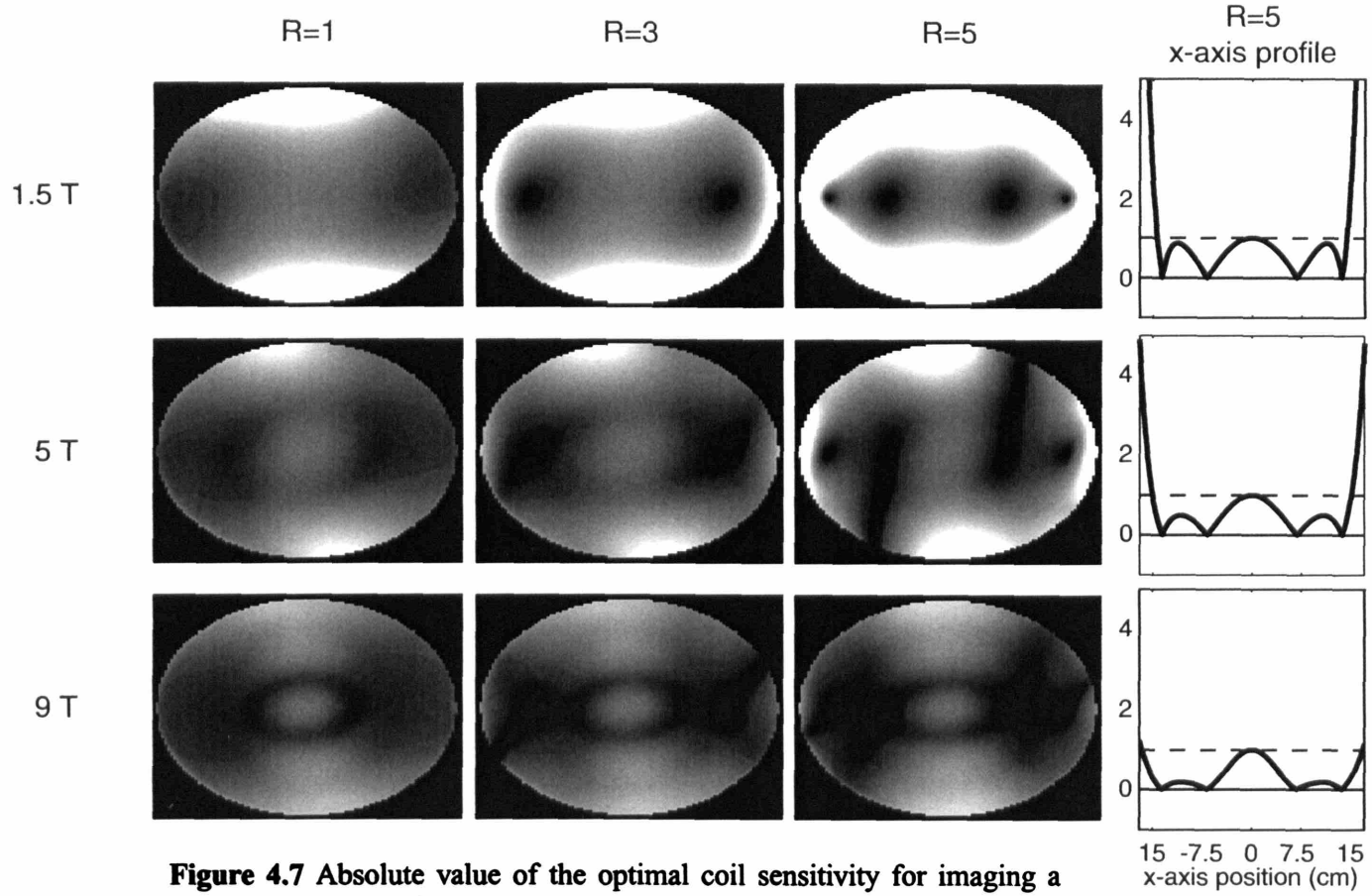

Figure 4.7 Absolute value of the optimal coil sensitivity for imaging a point at the center of the uniform elliptical cylinder (Fig. 4.1) for a variety of field strengths (1.5 T, 5 T, 9 T) and a variety of acceleration factors along the x-axis (R=1, R=3, R=5). Field plots are for the central axial plane. Profiles on the right are for 5-fold accelerations.

4.4.f SNR Dependence on Sample Conductivity

The role of conductivity is summarized in Figure 4.8, which plots the SNR at the center of the sample versus acceleration for three values of conductivity. An increase in conductivity decreases the absolute SNR at each level of undersampling (Figure 4.8a). Interestingly, the relative change in SNR brought about by acceleration is actually smaller for the more conductive samples (Figure 4.8b). Thus, while increased conductivity decreases the overall SNR, it has a slightly beneficial effect on spatial encoding.

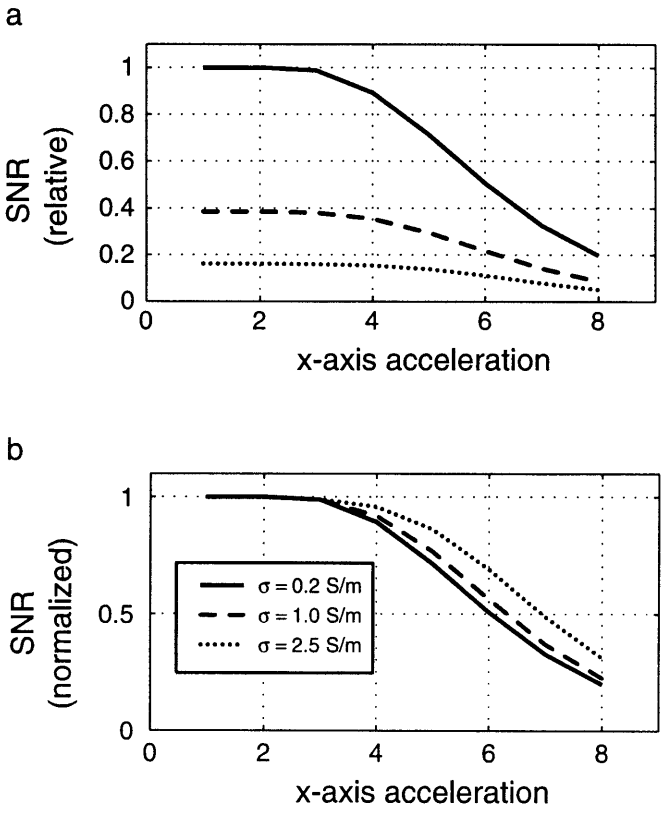

Figure 4.8 Dependence of the optimal SNR at the center of the uniform elliptical cylinder (Fig. 4.1) on the conductivity of the sample. a) SNR relative to the optimal unaccelerated reconstruction at a conductivity of 0.2 S/m. b) SNR values from (a), independently normalized so that the unaccelerated reconstruction has an SNR equal to 1 for each conductivity. A dielectric constant of 70 and field strength of 1.5T are used for each compuation.

4.4.g 1D vs. 2D acceleration

As noted earlier, the absolute value of the ultimate intrinsic SNR in parallel imaging depends very sensitively on the pattern of k-space sampling. As a simple example, we compare three Cartesian sampling approaches. In each case, the target FOV is the same, but we change the way that k-space is undersampled. In the first case, phase-encode points are omitted along the long axis of the ellipse, and in the second case they are omitted along the short axis. Finally, in the third case, we leave out phase-encoding steps along both axes and perform a two-dimensional parallel reconstruction. The results for the center of the elliptic sample are shown in Figure 4.9.

Figure 4.9a makes a broad comparison between the different undersampling patterns by restricting the plot to SNR values from two-dimensional reconstructions in which the x- and y-accelerations are equal. This curve is shown alongside the results obtained for one-dimensional accelerations along each of the two axes. As expected, there is a slower drop in SNR along the longer axis of the ellipse than along the shorter one. In addition, simultaneous undersampling along two dimensions achieves much greater SNR levels for the same amount of acceleration than either of the one-dimensional schemes. A net 15-fold increase in speed is possible before 50% of the maximum attainable SNR is lost. Note once again that, as compared with the relative SNR values shown, the actual total SNR loss will include an additional factor proportional to the square root of the amount of undersampling in k-space.

Two-dimensional undersampling patterns are complicated by the fact that there are several ways of choosing the x- and y- undersampling levels in order to achieve the same net acceleration. Figure 4.9b shows the results for the combination of integral x- and y- undersampling patterns that leads to the highest SNR for each net acceleration. The actual amount of undersampling along each dimension is shown above each point. Potentially aliased points that lie outside the sample are set to zero automatically, which decreases the number of points that must be "unfolded" in order to achieve a given net reduction in scan time. The best results are achieved when the undersampling along the longer axis is slightly larger than that along the shorter axis. The results show occasional sharp variations due to the fact that we have restricted ourselves to integer accelerations along each dimension. For example, in order to achieve a net acceleration of 6, we can make a 3-fold acceleration along the x-axis and a 2-fold acceleration along the y-

axis. For a net acceleration of 7, we are forced to have a full 7-fold acceleration along the x-axis, leading to a sharp drop in the maximum attainable SNR. The restriction to integral accelerations has been made only to simplify our calculations, and is not required in practice.

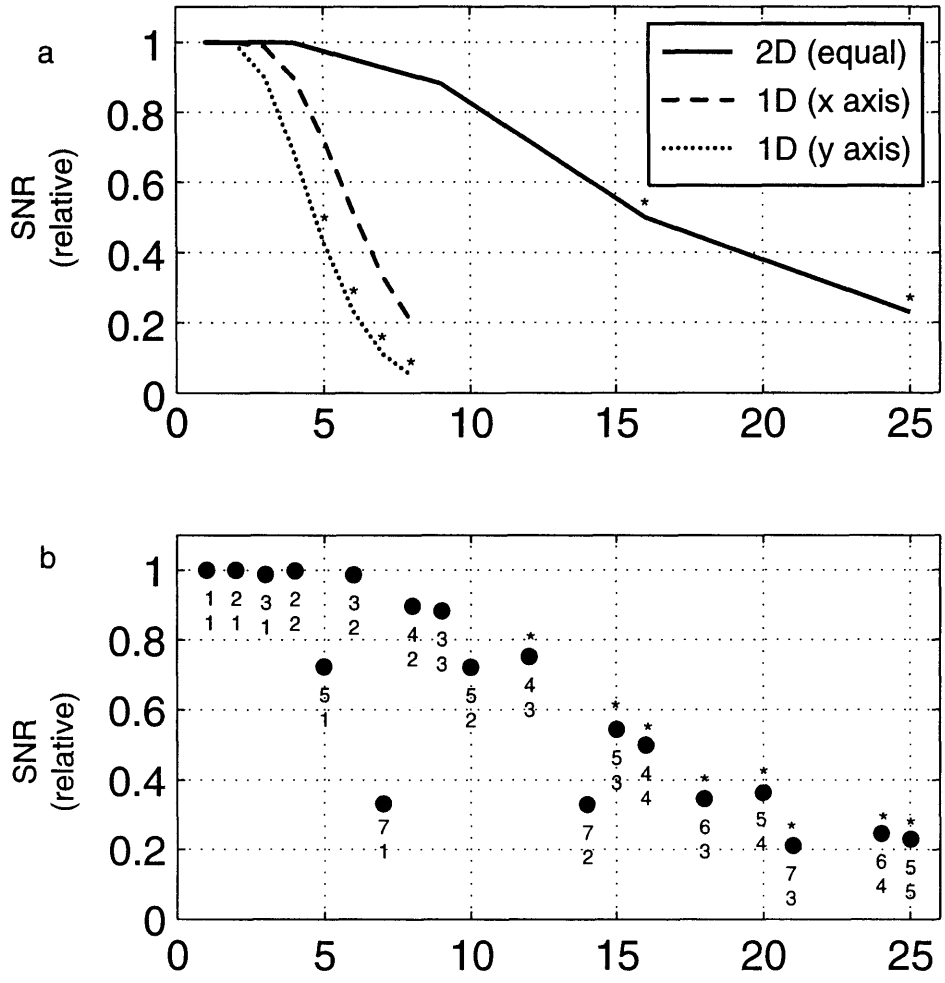

Figure 4.9 Optimal SNR at the center of the uniform elliptical cylinder (Fig. 4.1) for different patterns of undersampling. a) The dashed and dotted lines show the result of undersampling in a 1D pattern along the x-axis and y-axis, respectively. The solid line represents the result for 2D acceleration with equal amounts of acceleration along the x- and y-axes. b) Filled circles show the results of 2D undersampling patterns for various net amounts of acceleration. Above each point are the levels of x- and y-undersampling that were used to achieve each net acceleration. Points marked with an asterisk indicate slower convergence (see text).

4.4.h SNR Dependence on Sample Shape

The computational approach presented here is highly flexible in terms of the sample shapes that can be considered. In Figure 4.10, we compare the elliptic cylinder with a circular cylinder whose diameter is equal in length to the semi-major axis of the ellipse. Once again, the conductivity and permittivity are chosen to match that of liver. Each curve is independently normalized such that the unaccelerated SNR level is set to one. Parallel imaging performance for the circular cylinder is better than that along the short axis of the ellipse while it is not as good as that along the long axis of the ellipse.

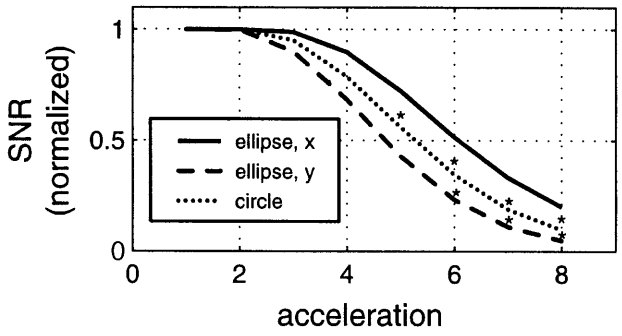

Figure 4.10 Behavior of the optimal SNR as a function of sample shape. The results from undersampling along the x- and y-axes of the central axial plane of the uniform elliptical cylinder in Fig. 4.1 are shown. Results are also shown for acceleration along the x-axis of the central axial plane from a circular cylinder with diameter 34.1 cm. Dielectric properties are those of liver at 1.5 T. All plots are individually normalized so that the unaccelerated reconstruction has SNR of 1 for each sample shape. Points marked with an asterisk indicate slower convergence (see

4.5 Discussion

We have presented a procedure for establishing a physical upper bound on the SNR that is attainable by any real coil array for a given level of acceleration in parallel MRI. Our approach utilizes a complete basis set of coil sensitivities proposed in an earlier work and subjects them to the constraints of the parallel imaging reconstruction. In the simple case of uniform undersampling, which leads to aliasing from a finite number of pixels across the field-of-view, the sensitivity optimization corresponds to creating an electromagnetic field with minimum total noise power, subject to the condition that the left-hand circularly polarized component of the

magnetic field is unity at the point of interest and goes to zero at all of the aliasing points. As the amount of undersampling increases, the aliased points move closer together and the resulting field must sustain more and more rapid oscillations in order to produce the required spatial nulls. The ability of a particular basis function to sustain such rapid oscillations is determined by its spatial wavelength (Eq. [4.26]). Note that for a given field strength, the wavelength can be made arbitrarily short by choosing basis functions with small values of $\hat{\mathbf{k}}_l^r \cdot \hat{\mathbf{k}}_l^i$. However, achievement of these rapid oscillations comes at the cost of stronger exponential damping (Eq. [4.27]). Basis functions that experience larger amounts of damping bring with them more exposure to noise for a given amount of signal. Alternatively, the creation of rapid oscillations with basis functions that are less damped (and therefore more slowly-varying) leads to large amplifications of small differences between those functions, similarly increasing the detectors' sensitivity to noise.

This physical description of the parallel imaging SNR cutoff is highlighted by the comparisons of SNR performance at different field strengths (Figure 4.6) as well as by the plots of the resulting sensitivity patterns for various accelerations (Figure 4.7). As noted above, for our general choice of plane-wave modes, there is no single characteristic spatial frequency for a given magnetic field strength. For the purposes of straightforward comparison as a function of field strength, however, we can consider those modes at each field strength that have the maximum skin depth, i.e. those for which $\hat{\mathbf{k}}_l^r \cdot \hat{\mathbf{k}}_l^i = 1$. Properties of these modes are listed as a function of field strength for liver in Table 4.1. The shortened wavelengths of these modes at higher field strengths yields sensitivity functions that are more amenable to alternating constructive and destructive interference. This potential for interference offers two SNR advantages. First, it permits the construction of focused fields, which maintain sensitivity to the signal at the center (or other point of interest) while decreasing sensitivity to noise in other parts of the sample. This effect has been predicted (91) and observed (61) even for conventional gradient-encoded imaging. Second, parallel imaging techniques are able to further exploit constructive and destructive interference in order to more easily create magnetic fields that go to zero at all of the aliasing positions.

One caution about such a simple explanation of field strength behavior is that, even for the selected subset of plane-wave modes for which $\hat{\mathbf{k}}_l^r \cdot \hat{\mathbf{k}}_l^i = 1$, the reduction in wavelength with increasing field strength/frequency also leads to a shortening of the skin depth (see Table 4.1). In principle, it might be possible for this skin depth change to outweigh the effects of the shortened wavelength. However, the results of the calculations described in this chapter suggest that for tissues with the electrical properties considered here, the improved spatial encoding properties resulting from a reduction in the electromagnetic wavelength are the dominant effects.

The bottom line, then, is that increasing field strengths promise benefits for parallel MRI that exceed those expected for conventional gradient-encoded MRI. This is a powerful synergy, as the increased SAR at high field will likely make parallel MRI even more crucial than it is at low fields. It is important to note that in this study, the optimal coil design at one field strength has been compared with the optimal coil design at a higher field strength. For any fixed array design, it may not be possible to realize these gains by simply using the same design at higher fields. Despite these concerns, a finite difference time domain model of a four-coil head array has been shown to offer significant decreases in g-factor at higher fields, even without any change in array layout (75).

It should be noted that, following publication of our results on ultimate intrinsic SNR, another study exploring the ultimate intrinsic SNR for parallel MRI in the brain has been presented (100). That study used a very similar overall approach to the one presented here, except that the authors used spherical harmonic basis functions (more appropriate for their sample) rather than planewaves. The results of that study, particularly the field strength dependence, are entirely consistent with those presented here.

At both 1.5 T and 5 T – the two field strengths for which results are displayed in Figure 4.5 – the optimum achievable SNR is lowest at the center of the sample and increases monotonically towards the edge. Points near the edge of the sample also exhibit smaller differences between accelerated and unaccelerated acquisitions. The damping of the fields by the resistive sample permits coil sensitivities concentrated near one side of the sample to fall off naturally towards the

other side. Thus, the coil sensitivities are able to reach zero at several aliasing points without the rapid variations that are characteristic of reconstructions at the center. The comparatively smooth spatial dependence seen for the optimum SNR stands in contrast to the "hot spots" of noise amplification seen in regions of particularly high sensitivity degeneracy in studies aimed at optimizing arrays with fixed conductor arrangements (63).

The electrical properties of the sample have a powerful influence on parallel imaging performance. Our results (Figure 4.8) demonstrate that while increased conductivity decreases the overall SNR of our reconstructions, it enhances spatial encoding by moving the critical drop in SNR towards higher acceleration factors.

The algorithm described in this chapter may also be used as an analytical tool for investigating the relative advantages of different k-space sampling patterns. In parallel imaging, it can be difficult to make direct comparisons between the effectiveness of different acquisition schemes because a coil that is optimized for one acquisition scheme may not be optimized for the other. The technique presented here compares the best possible configuration of coil sensitivities for each pattern of sampling. The specific coil design is removed from consideration. As an example, when the k-space sampling pattern is regular and the undersampling is in a single direction, a steep cutoff in achievable performance is seen at an acceleration factor of 5. For any given amount of undersampling, potential aliasing points are further apart along the long axis of the ellipse than they are along the short axis. This geometrical difference makes the overall spatial variations required along the long axis slower than those along the short axis. Thus, the SNR cutoff occurs at a slightly higher acceleration when undersampling is chosen along the long axis than it does when undersampling is chosen along the short axis (Figure 4.9). If phase-encode lines are skipped in two directions simultaneously, k-space may be undersampled by a net factor of 15 before the SNR cutoff is reached. Including the factor proportional to the square root of the reduction in scan time, the net SNR reduction at an acceleration factor of 15 approaches 86%. While this loss is prohibitively great for many routine applications, there are likely several applications with intrinsically high SNR where an order of magnitude reduction in scan time will allow access to phenomena that make the sacrifice worthwhile.

The reconstruction used in this study (Equation [4]) requires that coil sensitivities be pinned rigorously to zero at the aliasing points in order to achieve a theoretically "perfect" reconstruction. However, numerical conditioning methods are often used to achieve an increase in SNR in exchange for a small amount of residual aliasing that often cannot be seen above the noise floor (16). The inclusion of such numerical conditioning may permit the otherwise strict SNR limits presented here to be exceeded.

The calculations presented here introduce several simplifications. Most prominently, we have assumed the existence of a uniform excitation field. This may not always be possible, especially at high field strengths (101). However, a modified excitation produces a modulation that applies equally to *all* of the coils within the array, leaving their relative amplitudes unchanged. Thus, while a non-uniform excitation will almost certainly impact the absolute value of the overall SNR, it may not have as significant an effect on the relative changes that occur with increasing acceleration. Our calculations also assume that RF coils can be placed anywhere outside of the sample. In practical construction, however, surface coils are maintained at some minimum distance from the patient's body, and this may limit the SNR that can be achieved. Other electrical effects such as inductive coupling have also not been considered here. Inductive coupling may affect practical implementations, though its net effect on array performance has still not been definitively established (89,90,102).

The planewave basis functions used in this study have a great deal of flexibility and may be applied to several different types of samples. As a simple demonstration, we show significant differences in the potential parallel MRI performance for an elliptical cylinder versus a circular cylinder. Still, all of our calculations are based on a homogeneous sample that is filled with materials with uniform electrical properties. In reality, conductivity and permittivity vary dramatically from tissue to tissue. Boundaries between regions that differ electrically may create discontinuities that affect the potential sharpness of the coil sensitivities. With minor modifications, our approach can eventually be applied to heterogeneous samples.

One of the major difficulties with using plane wave basis functions in this study is that they were not spatially orthogonal throughout the volume of the sample being considered. This lack of

orthogonality led to potential numerical instabilities, which were mitigated by using a software package with extended numerical precision. As mentioned earlier, plane waves are still convenient because they allow the noise covariance matrix to be computed analytically. The singularity in the plane wave coefficients described in Section 4.3.a requires a cutoff in the allowed values of $\hat{\mathbf{k}}_l^r \cdot \hat{\mathbf{k}}_l^i$. However, the decreasing magnitudes of the sensitivity weighting functions for small $\hat{\mathbf{k}}_l^r \cdot \hat{\mathbf{k}}_l^i$ (Figure 4.2) suggests that modes with $\hat{\mathbf{k}}_l^r \cdot \hat{\mathbf{k}}_l^i$ values smaller than 0.05 will be unlikely to have a significant impact on the overall optimum SNR.

Finally, the approach that we have described has the potential to guide future coil designs for parallel imaging. The weighting factors generated by the optimization yield an electromagnetic field that corresponds to the optimal sensitivity for performing a parallel reconstruction of a given pixel. At the simplest level, coil design would amount to a target-field solution in which conductor patterns were found to produce that particular field. This simple approach is limited, however, because achieving the optimal performance in the context of a general (non-uniform) sampling of k-space requires a different field configuration for every point in the sample and may even require a different field configuration for each acquired point in k-space (Equation [4.19]). Thus, the most general and robust solution will likely be to construct a large array whose coil sensitivities themselves correspond to a suitable set of electromagnetic basis functions. This approach may require more RF coil elements and receivers than a specific fixed design, but will have the advantage of producing the optimal SNR for a range of applications.

4.6 Acknowledgments

In addition to those mentioned in the beginning of this thesis, I would like to thank Professor Alan Edelman for very helpful discussions regarding the numerical aspects of this work.

4.7 Table 4.1 Dielectric properties of liver at various magnetic field strengths

Dielectric information obtained from Reference (99). As noted in the text, the wavelengths and skin depths listed are for those planewave modes with $\hat{\mathbf{k}}_l^r \cdot \hat{\mathbf{k}}_l^i = 1$ (for each frequency, the maximum wavelength and the maximum skin depth).

B_0 (T)	1.5	3	5	7	9
Larmor frequency (MHz)	63.9	128	213	298	383
Liver dielectric constant (99)	80.6	64.3	57.0	53.6	51.5
Liver permitivity ($x10^{-10}$ $coul^2/N\ m^2$) (99)	7.13	5.69	5.04	4.74	4.56
Liver conductivity (S/m) (99)	0.445	0.511	0.566	0.609	0.647
Wavelength in liver (m)	0.437	0.262	0.174	0.131	0.105
Wavelength in vacuum (m)	4.70	2.35	1.41	1.010	0.783
Skin depth in liver (m)	0.127	0.0932	0.0760	0.0671	0.0612

4.8 Appendix A. Weighting Coefficients for Uniform k-Space Sampling

When the k-space sampling pattern is uniform, Equation [4.22] can be used to specify a single optimal coil sensitivity for the reconstruction of a given pixel. Because this relation is central to many of the results presented in this paper, we offer a detailed description of the relationship between Equation [4.22] and the more general case described by Equation [4.20]. The simplifications of the parallel imaging reconstruction in the case of uniform sampling have been described in detail in references (16,87). We adapt some arguments from references (16,87) here in order to derive the particular values of the weighting coefficients, $\beta_{(j,l)}$, in Equation [4.22], and to emphasize the implications of uniform sampling for the determination of the optimal sensitivity pattern.

Equations [4.20] and [4.21] specify an optimal coil sensitivity that depends on both the reconstructed pixel j and the acquired k-space line m:

$$\begin{aligned}\boldsymbol{\rho}(\mathbf{r}_j)^{opt} &= \sum_m \sum_i e^{i\mathbf{k}_m\cdot\mathbf{r}_i}\left[\sum_l B^{inverse}_{j,(lm)}\boldsymbol{\mathcal{B}}_l(\mathbf{r})\cdot\hat{\mathbf{e}}_-\right]\rho(\mathbf{r}_i) \\ &\equiv \sum_m \sum_i e^{i\mathbf{k}_m\cdot\mathbf{r}_i} C^{opt}_{m,j}(\mathbf{r}_i)\rho(\mathbf{r}_i)\end{aligned} \quad . \qquad [4.33]$$

If, however, the entries of the inverse encoding matrix are separable such that

$$B^{inverse}_{j,(lm)} = \beta_{(jl)}\gamma_{(jm)}, \qquad [4.34]$$

then Equation [4.20] can be rewritten

$$\begin{aligned}\boldsymbol{\rho}(\mathbf{r}_j)^{opt} &= \sum_m \gamma_{(jm)} \sum_i e^{i\mathbf{k}_m\cdot\mathbf{r}_i}\left[\sum_l \beta_{(jl)}\boldsymbol{\mathcal{B}}_l(\mathbf{r})\cdot\hat{\mathbf{e}}_-\right]\rho(\mathbf{r}_i) \\ &\equiv \sum_m \gamma_{(jm)} \sum_i e^{i\mathbf{k}_m\cdot\mathbf{r}_i} C^{opt}_j(\mathbf{r}_i)\rho(\mathbf{r}_i)\end{aligned} \quad , \qquad [4.35]$$

and a single optimal coil sensitivity $C^{opt}_j(\mathbf{r}) = \sum_l \beta_{(jl)}\boldsymbol{\mathcal{B}}_l(\mathbf{r})\cdot\hat{\mathbf{e}}_-$ can be used for the acquisition of every k-space point $\mathbf{k}_m$. The object of this appendix, then, is to show that if the sampling of k-space is uniform, the separation shown in Equation [4.34] is possible.

For clarity, we restrict our discussion to reconstructions along a single axis. The derivation is trivially extended to higher dimensions. If n_p pixels are to be reconstructed from $n_k = n_p / R$ k-space points, then the signal equation becomes

$$S_l(m\Delta k) \approx \sum_j e^{i\frac{2\pi mj}{n_x}} C_l(j\Delta x)\rho(j\Delta x) + n_l(t),\ m = -\frac{n_k}{2}+1\ldots\frac{n_k}{2}, \qquad [4.36]$$

where the pixel resolution Δx is related to the target field-of-view (FOV) by $\Delta x = FOV / n_x$ and the undersampled k-space resolution is $\Delta k = 2\pi R / FOV$. The encoding matrix becomes

$$B_{(lm),j} = e^{i\frac{2\pi mj}{n_x}} C_l(j\Delta x). \qquad [4.37]$$

We also define the coil-by-coil Fourier matrix and its inverse as follows:

$$W^N_{(il),(jl')} = e^{i\frac{2\pi ij}{N}}\delta_{l,l'} \quad \tilde{W}^N_{(il),(jl')} = \frac{1}{N}e^{-i\frac{2\pi ij}{N}}\delta_{l,l'}. \qquad [4.38]$$

With these definitions, the encoding matrix [4.37] can be written in block-diagonal form:

$$\begin{aligned}\mathbf{B} &= \tilde{\mathbf{W}}^{n_k}\left(\mathbf{W}^{n_k}\mathbf{B}\right),\\ &= \tilde{\mathbf{W}}^{n_k}\hat{\mathbf{B}}\end{aligned} \qquad [4.39]$$

where we have made the definition

$$\hat{B}_{(li),j} = C_l(j\Delta x)\delta_{i+sn_k,j} \qquad s = 0,1,2\ldots(R-1). \qquad [4.40]$$

The block-diagonal form of the transformed encoding matrix $\hat{\mathbf{B}}$ represents the aliasing of pixels across the field-of-view. The inverse of $\hat{\mathbf{B}}$ will also be block-diagonal, of the form $\hat{B}^{inverse}_{j,(li)} = \beta_{(jl)}\delta_{j,i+sn_k}$, where the entries $\beta_{(jl)}$ depend only on the component coil l and the target pixel j. The total inverse encoding matrix is now:

$$\left[\mathbf{B}^{inverse}\right]_{(j,lm)} = \left[\hat{\mathbf{B}}^{inverse}\tilde{\mathbf{W}}^{n_k}\right]_{(j,lm)}$$
$$= \beta_{(jl)}\sum_{s=0}^{R-1} e^{2\pi im(j-sn_k)/n_k} . \qquad [4.41]$$
$$= \beta_{(jl)}\gamma_{(jm)}$$

This satisfies the condition specified by Equation [4.34], and we are thus justified in writing a single set of coefficients $\beta_{(jl)}$ that determine a single optimal coil sensitivity $C_j^{opt}(\mathbf{r})$, which can be used to acquire an image with optimal SNR at pixel $\mathbf{r}_j$. In this case, these coefficients are determined by inverting the block-diagonalized encoding matrix $\hat{\mathbf{B}}$.

Chapter 5.
General Discussion and Future Directions

Parallel imaging techniques are powerful tools for accelerating data acquisition in MRI. These strategies have been embraced clinically and exploited in order to increase patient comfort, enhance spatial resolution, expand anatomical coverage, and reduce image artifacts. This dissertation has been devoted to an exploration of three general aspects of using coil arrays for spatial encoding in MRI, which can impact the ultimate flexibility and capabilities of parallel imaging techniques.

This chapter begins with a summary of the major results, proceeds to explore potential future work in each area of this disseration, and concludes with a brief speculation about future directions for coil array design in parallel MRI more generally.

5.1 Summary of Major Results

The concentric coil array described in Chapter 2 is a novel coil array design strategy that allows for spatial encoding in multiple directions at once. This type of directional flexibility is important for several reasons. First, the theoretical calculations in Chapter 4 demonstrate that while image acceleration in a single direction is strictly limited, much higher acceleration factors are possible by simultaneously undersampling in two dimensions. Two-dimensional undersampling is generally achieved in the context of three-dimensional Cartesian k-space trajectories. Three-dimensional trajectories possess larger baseline SNR levels than their two-dimensional counterparts, which help to offset the SNR losses that occur due to parallel imaging. Multidirectional spatial encoding is also important for applications such as cardiac imaging, which employ multiple oblique image planes, whose orientations are typically not precisely known before the image acquisition.

Further work will involve expanding the directional flexibility of concentric arrays even further. While the four-element concentric array described in this work does show directional invariance when acceleration is parallel to the plane of the coil array, it has more difficulty accelerating acquisitions perpendicular to the plane of the array. This difficulty is common to any planar coil array design. A second set of elements on the posterior side of the patient can be added to provide true 3-dimensional spatial encoding capabilities. The use of radial and spiral k-space trajectories can take further advantage of the circular symmetries that are inherent in a concentric array.

As coil arrays are constructed with larger numbers of elements, and these elements need to be packed into a fixed area of the patient's surface, it will be increasingly important to consider the electrical interactions between array elements. The most problematic of these interactions is inductive coupling. Strong inductive coupling between array elements can cause the coil system to resonate in a series of collective modes, each of which has its own resonance frequency. When coupling is weaker, however, the effects of inductive coupling are mostly manifest as a sharing of signal and noise between coil elements. There has been some concern that broadened coil sensitivities might make a given coil array less effective at reconstructing data using parallel MRI. In Chapter 3, it was shown that, to the extent that coupling can be represented as a linear

combination of signal and noise voltages, it should be possible to compensate for the coupling in the course of the parallel MR reconstruction. In a series of experiments that systematically added coupling interactions to an eight-element coil array, the reconstructed image SNR changed by only a small amount. The residual changes in SNR that were observed were attributed to changes in the preamplifier noise figure, although more experiments will be necessary to prove this definitively.

The results presented from the studies of coupling in Chapter 3 do not remove the need for decoupling strategies altogether, but they do widen the tolerance for residual inductive coupling that may be present in coil array designs. In order to make this expanded tolerance more quantitative, however, it will be important to determine at exactly what point the changes in coil tuning and preamplifier noise figure are enough to seriously degrade the coil array performance.

In the efforts to use coil arrays to achieve high acceleration factors, it is important to consider fundamental limitations on image acceleration using parallel MRI. In Chapter 4, an optimization strategy was presented that used a complete set of coil sensitivity basis functions to determine the ultimate intrinsic SNR available in a parallel MRI reconstruction. In this study, it was demonstrated that the behavior of electromagnetic fields within the sample places strict constraints on the performance of any physically realizable coil array in parallel MRI. One important consequence of these electromagnetic constraints is that parallel imaging strategies are expected to become more effective at higher field strengths, where the electromagnetic wavelengths are shorter. Fields with shorter wavelengths are advantageous because they are more suited to producing the rapid spatial oscillations that are required by the parallel image reconstruction. As mentioned in Chapter 4, this field strength dependence is consistent with another recent study that used a similar field-optimization approach to examine the behavior of parallel MRI in the head (100).

The predicted field strength behavior from Chapter 4 and reference (100) has been additionally supported by a set of experiments that sought to emulate the behavior of sensitivity patterns at different field strengths by changing the conductivity and perimittivity of a phantom (76). When

the effective field strength was increased, it was found that coil arrays with identical geometries were able to reconstruct parallel MRI data with lower g-factors.

5.2 Future Directions: Towards High Performance Parallel MRI

The theoretical optimizations described in Chapter 4 provide tools for predicting the level of image acceleration that may be eventually possible using coil arrays, and the other chapters have addressed more practical issues that may be encountered when designing coil arrays capable of high levels of acceleration in flexible situations. Several important problems remain, however, in efforts to extend parallel MRI to more "high performance" applications, which require the reconstruction of data that has been undersampled by an order of magnitude or more. This section briefly discusses these problems, and provides a general overview of some potential solutions.

5.2.a Choice of Application

One of the most powerful attributes of parallel MRI techniques is generality. Parallel MRI methods are compatible with almost any acquisition strategy and – for small acceleration factors – they generally incur no greater loss in SNR than that which would be expected from reduced noise averaging. This property is evident from the field optimization calculations described in Chapter 4: 2-fold accelerations can be performed in both the x- and y-dimensions with almost no SNR penalty beyond the standard square root of 2 loss.

As the amount of acceleration is increased, however, a large drop in SNR due to the amplification of noise is to be expected. Because of this unavoidable SNR loss, the applications for highly-accelerated parallel MRI must be chosen carefully. Parallel MRI with large amounts of undersampling is best applied in those situations where 1) there is a large baseline SNR and 2) the information that is obtained makes the sacrifice in SNR worthwhile. Scans that involve the analysis of dynamic contrast enhancement – in the form of gadolinium or hyperpolarized agents – are straightforward examples of this type of application.

It should be noted, however, that although prospective applications for highly-accelerated parallel MRI are likely to be limited to those applications that offer high intrinsic SNR, coil

arrays that have been designed for those applications can still improve the robustness of image reconstructions for applications that require only a small amount of image acceleration.

5.2.b Electromagnetic Optimization of Coil Arrays

The electromagnetic field optimization presented in Chapter 4 can be used to generate optimal sensitivity patterns for the reconstruction of specific points in an elliptical sample. The calculations do not provide any prescriptions, however, for how to actually construct the coil arrays that will generate the optimum sensitivity patterns. One approach to building such coil arrays would be to use the sensitivity patterns as templates in a target-field approach similar to that used in gradient design. Sources of current on the outside of the sample can be varied iteratively until a field that is close to the optimum is found.

While this procedure is straightforward, it presents two practical difficulties. First, it has been pointed out in reference (100) that the inverse source problem for the fields in a source-free region is non-unique (103). This non-uniqueness is likely to introduce computational complexities into any algorithm for choosing conductor patterns. Second, and more significantly, the sensitivity patterns that are determined by the field optimization in Chapter 4 are only required to satisfy boundary conditions inside of the sample. Nothing is specified about the behavior of the fields outside of the sample. The behavior of the fields on the outside of the sample is important because these exterior fields affect the practicality of any potential coil array. The optimum sensitivity pattern may require current sources that are either infinitely far or impractically close to the surface of the sample. The size of the electric and magnetic fields that are generated on the outside of the sample may lead to inductive and capacitive interactions with surrounding structures. Incidentally, the lack of constraints on the field outside of the sample probably contributes to the numerical instabilities that are encountered in the calculations.

Practical constraints can be placed on the optimized coil array by enforcing additional boundary conditions on the fields outside of the sample. Some straightforward possibilities would be to require the fields to be zero at the position of the MR shield and establish a minimum distance between the sample surface and any current sources. The process of choosing specific conductor geometries can be further simplified by restricting all current sources to the surface of a cylinder

or plane, which is similar to the coil-optimization approach described for non-parallel MRI in reference (104). These constraints on the exterior field will lead to a new set of basis functions that will be a more physically realizable subset of the general set of functions that were used in the unconstrained calculation. The optimization procedure outlined in Chapter 4 can be performed on this more restricted basis set, leading to a more practical set of coil sensitivities than that described by the unconstrained optimum.

The restricted basis set of field sensitivities described above can, of course, be used without any reference to the more general sensitivity functions computed in this work. The global upper bound on SNR will still be relevant, however, for quantifying exactly how much potential performance has been lost by choosing more restricted basis sets. If the SNR results from the two basis sets are similar, then the restricted basis set can be used as a reliable way to approach the optimum. If the proposed practical restrictions on the electromagnetic field behavior require too much SNR to be sacrificed, then efforts can be directed towards overcoming the practical restrictions.

One common feature of the optimization strategies that have been discussed so far is that, in principle, different coil sensitivities are required for reconstructing a given point for each acceleration factor. However, it has been noted (100,105) that for Cartesian k-space trajectories, the optimum sensitivity for the reconstruction of a particular sample point using parallel MRI can be written as a linear combination of the optimum sensitivities for unaccelerated imaging of all of the potential aliasing points. This result implies that separate coil arrays do not necessarily need to be built for conventional and parallel MRI. However, it is unclear whether this principle is stable for small variations from the optimum. Specifically, if a set of coils are constructed that have SNR values within 10% of the optima for fully gradient-encoded images, there is no guarantee that the SNR values for the images reconstructed using parallel MRI will also be within 10% of the optimum.

5.2.c Consideration of Simple Grid-Based Designs

When contemplating restricted basis sets for producing optimal coil arrays, it will be important to consider the particularly simple design of a dense grid of simple loop coils that are tiled on a

two-dimensional surface. The superposition principle for electromagnetic fields implies that suitable linear combinations of small loop coils will always be able to mimic the sensitivity that is due to a larger, more complex, current pattern. As the component loops are made smaller, this type of array becomes equivalent to an infinite number of point magnetic dipoles arranged perpendicular to a surface. It has been pointed out, however, that even an infinite number of these magnetic dipoles are not sufficient to completely optimize the detected SNR; electric dipoles are required as well (104). Nevertheless, even if the simple grid does not lead to the highest possible SNR, its simplicity and generality makes it attractive.

5.2.d Practical Issues of New Coil Designs

The development of coil arrays with increasing numbers of independent elements will require several practical issues to be addressed. For example, while a linear combination of small coils can theoretically produce the same sensitivity pattern as a single larger coil, the smaller coils will require more conductor than the single larger one does. These extra conductor paths bring added noise. For example, a (simple, non-optimal) linear combination of the 16 elements in a 4x4 grid was shown to have 5% lower SNR than the equivalent single large loop (106). Furthermore, as the coils become smaller, the noise derived from the sample will no longer be larger than the noise derived from the array itself. While detector elements that are coil-noise dominated can certainly still be used for spatial encoding in parallel MRI, they will not be able to provide the same SNR performance as sample-noise dominated coils. If smaller coils are desired, then it is possible to use cooled copper or even superconducting surface coils (107). Additionally, coils that are used at higher field strengths experience a larger amount of sample resistance. This added resistance allows surface coils to be made much smaller at high field strengths before they become coil-noise dominated.

Another important practical consideration when designing coil arrays for high levels of acceleration is the added weight and bulk that accompanies the electronic circuitry and cables that are needed to retrieve the signal from each coil. Smaller, lighter, and more efficient signal detection circuitry will clearly be a very important component of these large-scale arrays.

5.3 General Conclusions

The ability of parallel MRI techniques to accelerate image acquisitions is fundamentally limited by the spatial information content of the sensitivity patterns of MR detectors. An intuitive framework has been provided for understanding the way that receiver coils are able to encode spatial information, and the results of several original research studies have been presented that address many of the fundamental and practical limits of coil array encoding. This work provides a tool for evaluating coil arrays that are used today and gives insight into the design of arrays for future applications of parallel MRI.

References

1. Roemer PB, Edelstein WA, Hayes CE, Souza SP, Mueller OM. The NMR phased array. Magn Reson Med 1990;16(2):192-225.

2. Hutchinson M, Raff U. Fast Mri Data Acquisition Using Multiple Detectors. Magnetic Resonance in Medicine 1988;6(1):87-91.

3. Kwiat D, Einav S, Navon G. A Decoupled Coil Detector Array for Fast Image Acquisition in Magnetic-Resonance-Imaging. Medical Physics 1991;18(2):251-265.

4. Carlson JW, Minemura T. Imaging Time Reduction through Multiple Receiver Coil Data Acquisition and Image-Reconstruction. Magnetic Resonance in Medicine 1993;29(5):681-688.

5. Ra JB, Rim CY. Fast Imaging Using Subencoding Data Sets from Multiple Detectors. Magnetic Resonance in Medicine 1993;30(1):142-145.

6. Kwiat D, Einav S. Preliminary Experimental Evaluation of an Inverse Aging Procedure Using a Decoupled Coil Detector Array in Magnetic-Resonance-Imaging. Medical Engineering & Physics 1995;17(4):257-263.

7. Sodickson DK, Manning WJ. Simultaneous acquisition of spatial harmonics (SMASH): Fast imaging with radiofrequency coil arrays. Magn Reson Med 1997;38(4):591-603.

8. Sodickson DK. Tailored SMASH image reconstructions for robust in vivo parallel MR imaging. Magn Reson Med 2000;44(2):243-251.

9. McKenzie CA, Ohliger MA, Yeh EN, Price MD, Sodickson DK. Coil-by-coil image reconstruction with SMASH. Magnetic Resonance in Medicine 2001;46(3):619-623.

10. McKenzie CA, Yeh EN, Sodickson DK. Improved spatial harmonic selection for SMASH image reconstructions. Magnetic Resonance in Medicine 2001;46(4):831-836.

11. Pruessmann KP, Weiger M, Scheidegger MB, Boesiger P. SENSE: Sensitivity encoding for fast MRI. Magnetic Resonance in Medicine 1999;42(5):952-962.

12. Kyriakos WE, Panych LP, Kacher DF, Westin CF, Bao SM, Mulkern RV, Jolesz FA. Sensitivity profiles from an array of coils for encoding and reconstruction in parallel (SPACE RIP). Magnetic Resonance in Medicine 2000;44(2):301-308.

13. Lee RF, Westgate CR, Weiss RG, Bottomley PA. An analytical SMASH procedure (ASP) for sensitivity-encoded MRI. Magn Reson Med 2000;43(5):716-725.

14. Griswold MA, Jakob PM, Nittka M, Goldfarb JW, Haase A. Partially parallel imaging with localized sensitivities (PILS). Magnetic Resonance in Medicine 2000;44(4):602-609.

15. Heidemann RM, Griswold MA, Haase A, Jakob PM. VD-AUTO-SMASH imaging. Magn Reson Med 2001;45(6):1066-74.

16. Sodickson DK, McKenzie CA. A generalized approach to parallel magnetic resonance imaging. Med Phys 2001;28(8):1629-1643.

17. Griswold MA, Jakob PM, Heidemann RM, Nittka M, Jellus V, Wang JM, Kiefer B, Haase A. Generalized Autocalibrating Partially Parallel Acquisitions (GRAPPA). Magnetic Resonance in Medicine 2002;47(6):1202-1210.

18. Bydder M, Larkman DJ, Hajnal JV. Generalized SMASH imaging. Magnetic Resonance in Medicine 2002;47(1):160-170.

19. Yeh EN, McKenzie CA, Lim D, Ohliger MA, Grant AK, Willig J, Rofsky N, Sodickson DK. Parallel Imaging with Augmented Radius in k-Space (PARS). In: Proceedings of the Tenth Annual Meeting of the International Society for Magnetic Resonance in Medicine, Honolulu, HI, USA, 2002. p 2399.

20. Zhang BD, Wang WD, Song XY, Zu DL, Chen GF, Bao SL. Parallel imaging methods for phased array MRI. Progress in Natural Science 2003;13(4):307-310.

21. McKenzie CA, Lim D, Ransil BJ, Morrin M, Pedrosa I, Yeh EN, Sodickson DK, Rofsky NM. Shortening MR image acquisition time for volumetric interpolated breath-hold examination with a recently developed parallel imaging reconstruction technique: Clinical feasibility. Radiology 2004;230(2):589-594.

22. Weiger M, Pruessmann KP, Boesiger P. Cardiac real-time imaging using SENSE. SENSitivity Encoding scheme. Magn Reson Med 2000;43(2):177-84.

23. Sodickson DK, McKenzie CA, Li W, Wolff S, Manning WJ, Edelman RR. Contrast-enhanced 3D MR angiography with simultaneous acquisition of spatial harmonics: A pilot study. Radiology 2000;217(1):284-289.

24. Larkman DJ, deSouza NM, Bydder M, Hajnal JV. An investigation into the use of sensitivity-encoded techniques to increase temporal resolution in dynamic contrast-enhanced breast imaging. Journal of Magnetic Resonance Imaging 2001;14(3):329-335.

25. Ohno Y, Kawamitsu H, Higashino T, Takenaka D, Watanabe H, van Cauteren M, Fujii M, Hatabu H, Sugimura K. Time-resolved contrast-enhanced pulmonary MR angiography using sensitivity encoding (SENSE). Journal of Magnetic Resonance Imaging 2003;17(3):330-336.

26. Griswold MA, Sodickson DK, Jakob PM, Chen Q, Goldfarb JW, Edelman RR. Resolution enhancement and artifact reduction in single shot MR imaging using SiMultaneous Acquisition of Spatial Harmonics (SMASH). Radiology 1997;205:1040-1040.

27. Bammer R, Keeling SL, Augustin M, Pruessmann KP, Wolf R, Stollberger R, Hartung HP, Fazekas F. Improved diffusion-weighted single-shot echo-planar imaging (EPI) in stroke using Sensitivity Encoding (SENSE). Magn Reson Med 2001;46(3):548-554.

28. de Zwart JA, van Gelderen P, Kellman P, Duyn JH. Application of sensitivity-encoded echo-planar imaging for blood oxygen level-dependent functional brain imaging. Magnetic Resonance in Medicine 2002;48(6):1011-1020.

29. Zhang W, Cory DG. Measurement of flow velocities by NMR using a spatially modulated RF field. Measurement Science and Technology 1998;9:670-675.

30. Bydder M, Larkman DJ, Hajnal JV. Detection and elimination of motion artifacts by regeneration of k-space. Magnetic Resonance in Medicine 2002;47(4):677-686.

31. Bydder M, Atkinson D, Larkman DJ, Hill DLG, Hajnal JV. SMASH navigators. Magnetic Resonance in Medicine 2003;49(3):493-500.

32. Kellman P, McVeigh ER. Ghost artifact cancellation using phased array processing. Magnetic Resonance in Medicine 2001;46(2):335-343.

33. Wright SW, Porter JR. Parallel Acquisition of MR Images Using Time Multiplexed Coils. Electronics Letters 1992;28(1):71-72.

34. de Zwart JA, Ledden PJ, Kellman P, van Gelderen P, Duyn JH. Design of a SENSE-optimized high-sensitivity MRI receive coil for brain imaging. Magn Reson Med 2002;47(6):1218-1227.

35. Bodurka J, Ledden PJ, van Gelderen P, Chu RX, de Zwart JA, Morris D, Duyn JH. Scalable multichannel MRI data acquisition system. Magnetic Resonance in Medicine 2004;51(1):165-171.

36. Zhu Y, Hardy CJ, Sodickson DK, Giaquinto R, Dumoulin CL, Kenwood G, Niendorf T, Lejay H, McKenzie C, Ohliger MA and others. Highly Parallel Volumetric Imaging with a 32-Element RF Coil Array. Magnetic Resonance in Medicine 2004;In Press.

37. McDougall MP, Wright SM, Brown DG. A 64 Channel RF Coil Array for Parallel Imaging at 4.7 Tesla. In: Eleventh Annual Meeting of the International Society for Magentic Resonance in Medicine, Toronto, Ontario, Canada, 2003.

38. Lee RF, Westgate CR, Weiss RG, Newman DC, Bottomley PA. Planar strip array (PSA) for MRI. Magnetic Resonance in Medicine 2001;45(4):673-683.

39. Lee RF, Hardy CJ, Sodickson DK, Bottomley PA. Lumped-element planar strip array (LPSA) for parallel MRI. Magnetic Resonance in Medicine 2004;51(1):172-183.

40. Hajnal JV, Larkman DJ, Herlihy DJ. An Array That Exploits Phase for SENSE Imaging. Denver, Colorado, USA, 2000. p 1719.

41. Tropp J, Sodickson DK, Ohliger MA. Feasibility of a TEM Surface Array for Parallel Imaging. In: Proceedings of the Tenth Annual Meeting of the International Society for Magnetic Resonance in Medicine, Honolulu, HI, USA, 2002. p 856.

42. Willig J, Brown R, Eagan T, Shvartsman S. SMASH RF Coil Arrays: Specialized Design Considerations. Denver, Colorado, USA, 2000. p 559.

43. Willig J, Brown R, Eagan T, Shvartsman S. Perfectly Sinusoidal SMASH Field Shapes from Birdcage Sectors. Glasgow, Scotland, 2001. p 696.

44. Duensing GR, Gotshal U, King S, Huang F. N-Dimensional Orthogonality of Volume Coils. In: Proceedings of the Tenth Annual Meeting of the International Society of Magnetic Resonance in Medicine, Honolulu, HI, 2002. p 771.

45. Lin FH, Kwong KK, Huang IJ, Belliveau JW, Wald LL. Degenerate mode birdcage volume coil for sensitivity-encoded imaging. Magnetic Resonance in Medicine 2003;50(5):1107-1111.

46. Eagan TP, Willig-Onwuachi JD, Shvartsman SM, Cheng YCN, Brown DG. The SENSE-Cage: A Half-Birdcage Volume Coil. In: Proceedings of the Twelfth Annual Meeting of the International Society for Magnetic Resonance in Medicine, Kyoto, Japan, 2004. p 1606.

47. Haake EM, Brown RW, Thompson MR, Venkatesan R. Magentic Resonance Imaging: Physical Principles and Sequence Design. New York: Wiley-Liss; 1999. 914 p.

48. Lin FH, Chen YJ, Belliveau JW, Wald LL. A wavelet-based approximation of surface coil sensitivity profiles for correction of image intensity inhomogeneity and parallel imaging reconstruction. Human Brain Mapping 2003;19(2):96-111.

49. Huang F, Chen Y, Saylor C, Rubin A, Akao J, Duensing GR. Inpainting for Sensitivity Maps. In: Proceedings of the Twelfth Annual Meeting of the International Society for Magnetic Resonance in Medicine, Kyoto, Japan, 2004. p 2407.

50. Bydder M, Larkman DJ, Hajnal JV. Combination of signals from array coils using image-based estimation of coil sensitivity profiles. Magnetic Resonance in Medicine 2002;47(3):539-548.

51. Jakob PM, Griswold MA, Edelman RR, Sodickson DK. AUTO-SMASH: a self-calibrating technique for SMASH imaging. MAGMA 1998;7:42-54.

52. McKenzie CA, Yeh EN, Ohliger MA, Price MD, Sodickson DK. Self-calibrating parallel imaging with automatic coil sensitivity extraction. Magn Reson Med 2002;47(3):529-538.

53. Yeh EN, Stuber M, McKenzie CA, Ohliger MA, Grant AK, Willig J, Sodickson DK. Self-Calibrated Spiral Parallel Imaging. Hawaii, 2002. p 2390.

54. Wang Y. Description of parallel imaging in MRI using multiple coils. Magnetic Resonance in Medicine 2000;44(3):495-499.

55. Hoult DI, Chen CN, Sank VJ. The field dependence of NMR imaging. II. Arguments concerning an optimal field strength. Magnetic Resonance in Medicine 1986;3(5):730-46.

56. Nyquist. Thermal Agitation of Electric Charge in Conductors. Physical Review 1928;32:110-113.

57. Jackson JD. Classical Electrodyamics. New York: John Wiley & Sons, Inc.; 1999.

58. Roemer PB, Edelstein WA. Ultimate sensitivity limits of surface coils. In: Proceedings of the Sixth Annual Meeting of the Society for Magnetic Resonance in Medicine, New York, 1987. p 410.

59. Wang J, Reykowski A, Dickas J. Calculation of the Signal-to-Noise Ratio for Simple Surface Coils and Arrays of Coils. IEEE Transactions on Biomedical Engineering 1995;42(9):908-917.

60. Kunz KS, Luebbers JL. The Finite Difference Time Domain for Electromagnetics. Boca Raton: CRC Press; 1993. 448 p.

61. Yang QX, Wang JH, Zhang XL, Collins CM, Smith MB, Liu HY, Zhu XH, Vaughan JT, Ugurbil K, Chen W. Analysis of wave behavior in lossy dielectric samples at high field. Magn Reson Med 2002;47(5):982-989.

62. Wright SM. Full-wave analysis of planar radiofrequency coils and coil arrays with assumed current distribution. Concepts in Magnetic Resonance 2002;15(1):2-14.

63. Weiger M, Pruessmann KP, Leussler C, Roschmann P, Boesiger P. Specific coil design for SENSE: A six-element cardiac array. Magn Reson Med 2001;45(3):495-504.

64. Jevtic J. Ladder Networks for Capacitive Decoupling in Phased-Array Coils. Glasgow, Scotland, 2001. p 17.

65. Lee RF, Giaquinto RO, Hardy CJ. Coupling and decoupling theory and its application to the MRI phased array. Magn Reson Med 2002;48(1):203-213.

66. Song XY, Wang WD, Zhang BD, Lei M, Bao SL. Digitalization decoupling method and its application to the phased array in MRI. Progress in Natural Science 2003;13(9):683-689.

67. Ledden P, Inati S. Four Channel Preamplifier Decoupled Phased Array for Brain Imaging at 1.5 T. In: Proceedings of the 9th Annual Meeting of the International Society for Magnetic Resonance in Medicine, Glasgow, 2001. p 1117.

68. Sodickson DK, Hardy CJ, Zhu Y, Giaquinto R, Kenwood G, Rofsky NM. Highly Accelerated Parallel MRI on an MR Scanner with 32 Receiver Channels. In: Proceedings of the 89th Scientific Assembly and Annual Meeting of the Radiological Society of North America, Chicago, IL, 2003. p 172.

69. Weiger M, Pruessmann KP, Boesiger P. 2D SENSE for faster 3D MRI. Magn Reson Mat Phys Biol Med 2002;14(1):10-19.

70. Ohliger MA, Greenman R, McKenzie CA, Sodickson DK. Concentric Coil Arrays for Spatial Encoding in Parallel MRI. Glasgow, Scotland, 2001.

71. Ohliger MA, Greenman R, McKenzie CA, Wiggins G, Giaquinto RO, Sodickson DK. Concentric Coil Arrays for Multidemnsional Spatial Encoding in Cardiac Parallel MRI. Kyoto, Japan, 2004.

72. Seeber DA, Pikelja V, Jevtic I. New RF Coil Topology for High Performance SENSE in 3D. In: Proceedings of the Eleventh Annual Meeting of the International Society for Magnetic Resonance in Medicine, Toronto, 2003. p 465.

73. Chan PH, Michael K, Anderson B. Diagonal-Arranged Quadrature Coil Arrays for 3D SENSE Imaging. In: Proceedings of the Twelfth Annual Meeting of the International Society for Magnetic Resonance in Medicine, Kyoto, Japan, 2004. p 2382.

74. Avdievich NI, Peshovsky A, Kennan RO, Hetherington HP. SENSE Imaging with Quadrature Half-Volume TEM Coil at 4T. In: Proceedings of the Twelfth Annual Meeting of the International Society for Magnetic Resonance in Medicine, Kyoto, Japan, 2004. p 1590.

75. Ledden P, Duyn JH. Ultra-high Frequency Array Performance: Predicted Effects of Dielectric Resonance. In: Proceedings of the ISMRM 10th Annual Meeting, Honolulu, 2002. p 324.

76. Wiesinger F, Moortele Vd, Adriany G, De Zanche N, Ugurbil K, Pruessmann KP. Parallel Imagin Performance as a Function of Field Strength -- An Experimental Investigation using Electrodynamic Scaling. In: Proceedings of the 12th Annual Meeting of the International Society for Magnetic Resonance in Medicine, Kyoto, Japan, 2004. p 323.

77. Constantinides CD, Atalar E, McVeigh ER. Signal-to-noise measurements in magnitude images from NMR phased arrays. Magnetic Resonance in Medicine 1997;38(5):852-857.

78. Yeh EN, McKenzie C, Grant AK, Ohliger MA, Willig-Onwuachi JD, Sodickson DK. Generalized Noise Analysis for Magnitude Image Combinations in Parallel MRI. In: Proceedings of the Eleventh Annual Meeting of the International Society for Magnetic Resonance in Medicine, Toronto, Ontario, Canada, 2003. p 21.

79. Sodickson DK, Griswold MA, Jakob PM, Edelman RR, Manning WJ. Signal-to-noise ratio and signal-to-noise efficiency in SMASH imaging. Sydney, Australia, 1998. p 1957.

80. Hoult DI. The principle of reciprocity in signal strength calculations -- a mathematical guide. Concepts in Magnetic Resonance 2000;12(4):173-187.

81. Ballon D, Meyer KL. Two-Dimensional Ladder Network Resonators. Journal of Magnetic Resonance, Series A 1994;111:23-28.

82. Reykowski A, Wright SM, Porter JR. Design of Matching Networks for Low Noise Preamplifiers. Magnetic Resonance in Medicine 1995;33:848-852.

83. Hoult DI, Richards RE. Signal-to-Noise Ratio of Nuclear Magnetic-Resonance Experiment. Journal of Magnetic Resonance 1976;24(1):71-85.

84. Duensing GR, Brooker HR, Fitzsimmons JR. Maximizing signal-to-noise ratio in the presence of coil coupling. J Magn Reson Ser B 1996;111(3):230-235.

85. Scott G. Preamplifier Noise Input Coupling for Phased Arrays. Honolulu, 2002. p 894.

86. King SB, Varosi S, Molyneaux DA, Duensing GR. The Effects of Ultra Low Input Impedance Preamplifiers on Phased Array Coil Design. Honolulu, 2002. p 330.

87. Pruessmann KP, Weiger M, Scheidegger MB, Boesiger P. SENSE: Sensitivity encoding for fast MRI. Magn Reson Med 1999;42(5):952-962.

88. Ohliger MA, Yeh EN, McKenzie CA, Sodickson DK. The Effect of Inductive Coupling on Parallel Image Reconstructions. In: Proc. ISMRM Workshop on Minimum Data Acquisition, Marco Island, FL, 2001. p 129-132.

89. Pruessmann K, Weiger M, Wiesinger F, Boesiger P. An Investigation Into the Role of Coil Coupling in Parallel Imaging. In: Proceedings of the ISMRM 10th Annual Meeting, Honolulu, 2002. p 196.

90. Ohliger MA, Ledden P, Yeh EN, McKenzie CA, Sodickson DK. The Effect of Inductive Coupling on Parallel Image Reconstructions. In: Proceedings of the ISMRM 10th Annual Meeting, Honolulu, 2002. p 197.

91. Ocali O, Atalar E. Ultimate intrinsic signal-to-noise ratio in MRI. Magn Reson Med 1998;39(3):462-473.

92. Ohliger MA, Yeh EN, McKenzie CA, Sodickson DK. Fundamental Physical Constraints on the Performance of Parallel Magnetic Resonance Imaging. In: Proceedings of the ISMRM 10th Annual Meeting, Honolulu, 2002. p 2387.

93. Wiesinger F, Pruessmann K, Boesiger P. Inherent Limitation of the Reduction Factor in Parallel Imaging as a Function of Field Strength. In: Proceedings of the ISMRM 10th Annual Meeting, Honolulu, HI, 2002. p 191.

94. Griswold MA, Lanz T, Haase A, Jakob PM. A Brute-Force Estimation of the SNR Limits of Sensitivity Encoding in a Cylindrical Geometry. Honolulu, 2002. p 2386.

95. Reykowski A, Schnell W, Wang J. Simulation of SNR Limit for SENSE Related Reconstruction Techniques. In: Proceedings of the ISMRM 10th Annual Meeting, 2002. p 2385.

96. Insko EK, Elliott MA, Schotland JC, Leigh JS. Generalized reciprocity. J Magn Reson 1998;131(1):111-7.

97. Ohliger MA, Grant AK, Sodickson DK. Ultimate intrinsic signal-to-noise ratio for parallel MRI: Electromagnetic field considerations. Magnetic Resonance in Medicine 2003;50(5):1018-1030.

98. Weisstein E. CRC Concise Encyclopedia of Mathematics. 2 ed. New York: Chapman & Hall/CRC; 2003. p 2775.

99. Gabriel C. Compilation of the Dielectric Properties of Body Tissues at RF and Microwave Frequencies: Brooks Air Force AL/OE-TR-1996-0037; 1996. Report nr AL/OE-TR-1996-0037.

100. Wiesinger F, Boesiger P, Pruessmann KP. Electrodynamics and Ultimate SNR in Parallel MR Imaging. Magnetic Resonance in Medicine 2004;52:376-390.

101. Hoult DI. Sensitivity and power deposition in a high-field imaging experiment. J Magn Reson Imaging 2000;12(1):46-67.

102. Ohliger MA, Ledden P, McKenzie C, Sodickson DK. The Effects of Inductive Coupling on Parallel MR Image Reconstructions. Magn Reson Med 2004;52(3):628-639.

103. Bleistein N, Cohen JK. Nonuniqueness in the inverse source problem in acoustics and electromagnetics. Jounral of Mathematical Physics 1976;18(2):194-201.

104. Schnell W, Renz W, Vester M, Ermert H. Ultimate Signal-to-Noise-Ratio of Surface and Body Antennas for Magnetic Resonance Imaging. IEEE Transactions on Antennas and Propagation 2000;48(3):418-428.

105. Reykowski A. How To Calculate the SNR Limit of SENSE Related Reconstruction Techniques. In: Proceedings of the 10h Annual Meeting of the International Society for Magnetic Resonance in Medicine, Toronto, Ontario, Canada, 2002. p 905.

106. Duensing GR, Akao J, Saylor C, Molyneaux D. Conductor Losses in Many Channel RF Coil Arrays. In: Proceedings of the 12th Annual Meeting of the International Society for Magnetic Resonance in Medicine, Kyoto, Japan, 2004. p 1583.

107. Wosik J, Xie LM, Nesteruk K, Xue L, Bankson JA, Hazle JD. Superconducting single and phased-array probes for clinical and research MRI. Ieee Transactions on Applied Superconductivity 2003;13(2):1050-1055.